

12-2008

# Calculations of Diffusion in FCC Binary Alloys Using On-the-fly Kinetic Monte Carlo

Erdi Bleda

Clemson University, ealacam@clemson.edu

Follow this and additional works at: [https://tigerprints.clemson.edu/all\\_dissertations](https://tigerprints.clemson.edu/all_dissertations)

 Part of the [Condensed Matter Physics Commons](#)

---

## Recommended Citation

Bleda, Erdi, "Calculations of Diffusion in FCC Binary Alloys Using On-the-fly Kinetic Monte Carlo" (2008). *All Dissertations*. 306.  
[https://tigerprints.clemson.edu/all\\_dissertations/306](https://tigerprints.clemson.edu/all_dissertations/306)

This Dissertation is brought to you for free and open access by the Dissertations at TigerPrints. It has been accepted for inclusion in All Dissertations by an authorized administrator of TigerPrints. For more information, please contact [kokeefe@clemson.edu](mailto:kokeefe@clemson.edu).

# CALCULATIONS OF DIFFUSION IN FCC BINARY ALLOYS USING ON-THE-FLY KINETIC MONTE CARLO

---

A Dissertation  
Presented to  
the Graduate School of  
Clemson University

---

In Partial Fulfillment  
of the Requirements for the Degree  
Doctor of Philosophy  
Physics and Astronomy

---

by  
Erdi Ata Bleda  
December 2008

---

Accepted by:  
Dr. Murray S. Daw, Committee Chair  
Dr. Joseph R. Manson  
Dr. Chad E. Sosolik  
Dr. Sean Brittain

# Abstract

With the recent advancements in computer technologies and the improvements in simulation algorithms, along with the theories, has allowed scientists to carry out diffusion calculations more efficiently, especially for the cases where either the diffusion itself takes longer, or there is no available isotope to carry out the diffusion experiments such as *tracer diffusion*.

In this work, we present a systematic approach to diffusion in intermetallic alloys such as weakly clustered  $Cu - Ni$  and weakly ordered  $Au - Ag$ . We use Accelerated Molecular Dynamics (AMD) combined with the Embedded Atom Method (EAM) to find the necessary saddlepoint energies. With this technique, we calculate the tracer diffusivity coefficients for  $Cu - Ni$  (temperature range  $700 - 1300K$ ) and for  $Au - Ag$  (temperature range  $800 - 1300K$ ) as a function of composition and temperature. We assume that the vacancy-assisted diffusion mechanism is governing the whole process. In our calculations we keep the vacancy concentration fixed. We observe that the results are in agreement with Arrhenius behavior as discussed in detail in Chapter 4: *Results*. However closer to critical temperature, the results are overwhelmed by statistical fluctuations.

During the simulations at low temperatures, we sometimes find that the vacancy spends a large number of steps moving locally without accomplishing significant displacements or accumulating much simulated time. To overcome this “sandtrap”

problem, we develop a systematic approach which is discussed in Chapter 5: *Sandtrap Limitation and How to Overcome it* in detail.

We also analyze the motion and the “width” of the Anti-Phase Boundary (APB) perpendicular to its slip plane for  $Ni_3Al$  using the same approach mentioned above for various temperatures (1000, 1200 and 1500K) under no driving force. We create the APB in the center of the sample and observe its motion. In addition, we create the APB farther away from the center and fix the atoms at the end of each side. This puts a bias on the motion of the APB by limiting the number of possible escapes in a certain direction, thus “forcing” it to move towards the center. We observe the motion of the APB and the results are discussed in detail in Chapter 4: *Results*.

# Dedication

This work is dedicated to my mother for her tremendous support and in loving memory of my grandfather.

# Acknowledgments

First, I would like to express my deepest gratitude to my adviser, Dr. Daw for his advices and support on my studies towards ph.D. I also would like to thank each one of my committee members for accepting being in my committee. And finally, I would like to thank Xing Gao for her help in the calculations of  $Au - Ag$ , and her patience in our countless discussions.

This project is carried out with the support from NSF-ITR.

# Table of Contents

<b>Title Page</b> . . . . .	<b>i</b>
<b>Abstract</b> . . . . .	<b>ii</b>
<b>Dedication</b> . . . . .	<b>iv</b>
<b>Acknowledgments</b> . . . . .	<b>v</b>
<b>List of Tables</b> . . . . .	<b>viii</b>
<b>List of Figures</b> . . . . .	<b>x</b>
<b>1 Introduction</b> . . . . .	<b>1</b>
<b>2 Theory</b> . . . . .	<b>6</b>
<b>3 Simulation</b> . . . . .	<b>14</b>
3.1 Embedded Atom Method (EAM) . . . . .	16
3.2 Saddlepoint Search . . . . .	18
3.3 On-the-fly kinetic Monte Carlo Simulation . . . . .	23
<b>4 Results</b> . . . . .	<b>30</b>
4.1 Bulk Tracer Diffusivity for $Cu - Ni$ . . . . .	30
4.2 Bulk Tracer Diffusivity for $Au - Ag$ . . . . .	52
4.3 Mobility of Anti-Phase Boundary in $Ni_3Al$ . . . . .	68
<b>5 Sandtrap Limitation and How to Overcome it</b> . . . . .	<b>90</b>
<b>6 Conclusions and Discussion</b> . . . . .	<b>97</b>
6.1 Diffusion in Binary Alloys . . . . .	97
6.2 Translation of an APB . . . . .	98
<b>7 Future Work</b> . . . . .	<b>99</b>

References . . . . . 100



# List of Tables

4.1	Parameters obtained by a global fit to all of the presented kMC results for scaled tracer diffusivity in $Cu - Ni$ . . . . .	34
4.2	Parameters obtained by a global fit to all of the presented kMC results for scaled tracer diffusivity in $Au - Ag$ . . . . .	54
4.3	Histogram of sites $Al$ atoms occupy per layer for the initial configuration. There are total 32 $Al$ atoms per layer. Due to phase shift (remember, APB) after the fifth layer, $Al$ atoms now reside on site three. . . . .	74
4.4	The averaged histogram of sites $Al$ atoms occupy per layer over intermediate configurations after the third run at $T = 1000$ K. Initially the APB was positioned in the middle (between the fifth and the sixth layer). The histogram for the first two and the last two layers are not allowed to change due to the non-movable region. . . . .	75
4.5	The averaged histogram of sites $Al$ atoms occupy per layer over intermediate configurations for the final configuration at $T = 1000$ K. Initially the APB was positioned in the middle (between the fifth and the sixth layer). The histogram for the first two and the last two layers are not allowed to change due to the non-movable region. . . . .	76
4.6	The averaged histogram of sites $Al$ atoms occupy per layer over intermediate configurations for the final configuration at $T = 1200$ K. Initially the APB was positioned in the middle (between the fifth and the sixth layer). The histogram for the first two and the last two layers are not allowed to change due to the non-movable region. . . . .	77

4.7	The averaged histogram of sites <i>Al</i> atoms occupy per layer over intermediate configurations for the final configuration at $T = 1500$ K. Initially the APB was positioned in the middle (between the fifth and the sixth layer). The histogram for the first two and the last two layers are not allowed to change due to the non-movable region.	78
4.8	Histogram of sites <i>Al</i> atoms occupy per layer for the initial configuration. There are total 32 <i>Al</i> atoms per layer. Due to phase shift (remember– APB) after the seventh layer, <i>Al</i> atoms now reside on site three. . . . .	80
4.9	The averaged histogram of sites <i>Al</i> atoms occupy per layer over intermediate configurations for the third run at $T = 1000$ K. The histogram for the first two and the last two layers are not allowed to change due to the non-movable region. . . . .	81
4.10	An early snapshot of the configuration of the simulation running at $T=1000$ K under no driving force. . . . .	81
4.11	A later snapshot of the configuration of the simulation running at $T=1000$ K under no driving force. . . . .	82

# List of Figures

1.1	Direct exchange mechanism: Two atoms swap places. This introduces a local distortion in the lattice. . . . .	4
1.2	Ring mechanism: In order to observe a migration of an atom, the atoms need to move in a correlated manner. . . . .	4
1.3	Interstitial mechanism: If there are spaces between atoms, those spaces can be used by smaller atoms to migrate. . . . .	5
1.4	Single vacancy mechanism: Vacancy exchanges places with one of its nearest neighbors. . . . .	5
3.1	$A_3B$ FCC ( $L1_2$ ) structure. Each atom has 12 nearest neighbors. . . . .	17
3.2	12 nearest neighbor of atom $A$ : 4 $B$ 's and 8 $A$ 's. . . . .	17
3.3	12 nearest neighbor of atom $B$ : 12 $A$ 's. . . . .	17
3.4	2-D visualization of dimer near saddlepoint (image taken from [HJ99]).	20
3.5	Using the original NEB equations can develop kinks along the path (image taken from [HJ00]). . . . .	22
3.6	Using the modified tangents does not develop kinks along the path and converges smoothly (image taken from [HJ00]). . . . .	23
3.7	1-D energy-valley with 2 exits as a function of displacement. $\Delta E_{+x}$ and $\Delta E_{-x}$ are the saddlepoint energies to exit the valley. $\Delta E_{+x}$ is usually not equal to $\Delta E_{-x}$ . . . . .	24

4.1	$Cu - Ni$ phase diagram ( <i>source: www.factsage.com</i> ) . . . . .	31
4.2	SRO vs. $Cu$ concentration for $T = 700, 1000$ and $1300$ K. The fitted quadratics with the boundary condition SRO vanish at 0% and 100% $Cu$ concentrations are also shown. . . . .	32
4.3	$d_{Cu}$ vs. $Cu$ concentration at 700 K for $Cu - Ni$ . The curve is the global fit to all compositions and temperatures, and the symbol “*” shows the result of kMC runs. . . . .	35
4.4	$d_{Ni}$ vs. $Cu$ concentration at 700 K for $Cu - Ni$ . The curve is the global fit to all compositions and temperatures, and the symbol “*” shows the result of kMC runs. . . . .	36
4.5	$d_{Cu}$ vs. $Cu$ concentration at 1000 K for $Cu - Ni$ . The curve is the global fit to all compositions and temperatures, and the symbol “*” shows the result of kMC runs. . . . .	37
4.6	$d_{Ni}$ vs. $Cu$ concentration at 1000 K for $Cu - Ni$ . The curve is the global fit to all compositions and temperatures, and the symbol “*” shows the result of kMC runs. . . . .	38
4.7	$d_{Cu}$ vs. Temperature (K) at a fixed $Cu$ concentration, $x = 0.25$ for $Cu - Ni$ . The curve is the global fit to all compositions and temperatures, and the symbol “*” shows the result of kMC runs. . . . .	39
4.8	$d_{Ni}$ vs. Temperature (K) at a fixed $Cu$ concentration, $x = 0.25$ for $Cu - Ni$ . The curve is the global fit to all compositions and temperatures, and the symbol “*” shows the result of kMC runs. . . . .	40
4.9	$d_{Cu}$ vs. Temperature (K) at a fixed $Cu$ concentration, $x = 0.50$ for $Cu - Ni$ . The curve is the global fit to all compositions and temperatures, and the symbol “*” shows the result of kMC runs. . . . .	41
4.10	$d_{Ni}$ vs. Temperature (K) at a fixed $Cu$ concentration, $x = 0.50$ for $Cu - Ni$ . The curve is the global fit to all compositions and temperatures, and the symbol “*” shows the result of kMC runs. . . . .	42
4.11	$d_{Cu}$ vs. Temperature (K) at a fixed $Cu$ concentration, $x = 0.75$ for $Cu - Ni$ . The curve is the global fit to all compositions and temperatures, and the symbol “*” shows the result of kMC runs. . . . .	43

4.12	$d_{Ni}$ vs. Temperature at a fixed $Cu$ concentration, $x = 0.75$ for $Cu - Ni$ . The curve is the global fit to all compositions and temperatures, and the symbol “*” shows the result of kMC runs. . . . .	44
4.13	Results of kMC simulations of $d_{Cu}$ plotted in Arrhenius form at 25% $Cu$ concentration for the temperature range 700 – 1300 K. . . . .	45
4.14	Results of kMC simulations of $d_{Ni}$ plotted in Arrhenius form at 25% $Cu$ concentration for the temperature range 700 – 1300 K. . . . .	46
4.15	Results of kMC simulations of $d_{Cu}$ plotted in Arrhenius form at 50% $Cu$ concentration for the temperature range 700 – 1300 K. . . . .	47
4.16	Results of kMC simulations of $d_{Ni}$ plotted in Arrhenius form at 50% $Cu$ concentration for the temperature range 700 – 1300 K. . . . .	48
4.17	Results of kMC simulations of $d_{Cu}$ plotted in Arrhenius form at 75% $Cu$ concentration for the temperature range 700 – 1300 K. . . . .	49
4.18	Results of kMC simulations of $d_{Ni}$ plotted in Arrhenius form at 75% $Cu$ concentration for the temperature range 700 – 1300 K. . . . .	50
4.19	Migration energy of both $Cu$ and $Ni$ for $Cu - Ni$ as a function of $Cu$ concentration, which is obtained by the global fitting of kMC results to Eq. 3.11 for all temperatures and compositions. . . . .	51
4.20	$Ag - Au$ phase diagram ( <i>source: www.factsage.com</i> ) . . . . .	52
4.21	SRO vs. $Ag$ concentration for $T = 600, 800$ and $1000$ K. The fitted quadratics with the boundary condition SRO vanish at 0% and 100% $Ag$ concentrations are also shown. . . . .	53
4.22	$d_{Au}$ vs. $Ag$ concentration at 800 K for $Au - Ag$ . The curve is the global fit to all compositions and temperatures, and the symbol “*” shows the result of kMC runs. . . . .	55
4.23	$d_{Ag}$ vs. $Ag$ concentration at 800 K for $Au - Ag$ . The curve is the global fit to all compositions and temperatures, and the symbol “*” shows the result of kMC runs. . . . .	56

4.24	$d_{Au}$ vs. $Ag$ concentration at 1000 K for $Au - Ag$ . The curve is the global fit to all compositions and temperatures, and the symbol “*” shows the result of kMC runs. . . . .	57
4.25	$d_{Ag}$ vs. $Ag$ concentration at 1000 K for $Au - Ag$ . The curve is the global fit to all compositions and temperatures, and the symbol “*” shows the result of kMC runs. . . . .	58
4.26	$d_{Au}$ vs. $Ag$ concentration at 1300 K for $Au - Ag$ . The curve is the global fit to all compositions and temperatures, and the symbol “*” shows the result of kMC runs. . . . .	59
4.27	$d_{Ag}$ vs. $Ag$ concentration at 1300 K for $Au - Ag$ . The curve is the global fit to all compositions and temperatures, and the symbol “*” shows the result of kMC runs. . . . .	60
4.28	Results of kMC simulations of $d_{Au}$ plotted in Arrhenius form at 25% $Ag$ concentration for the temperature range 800 – 1300 K. . . . .	61
4.29	Results of kMC simulations of $d_{Ag}$ plotted in Arrhenius form at 25% $Ag$ concentration for the temperature range 800 – 1300 K. . . . .	62
4.30	Results of kMC simulations of $d_{Au}$ plotted in Arrhenius form at 50% $Ag$ concentration for the temperature range 800 – 1300 K. . . . .	63
4.31	Results of kMC simulations of $d_{Ag}$ plotted in Arrhenius form at 50% $Ag$ concentration for the temperature range 800 – 1300 K. . . . .	64
4.32	Results of kMC simulations of $d_{Au}$ plotted in Arrhenius form at 75% $Ag$ concentration for the temperature range 800 – 1300 K. . . . .	65
4.33	Results of kMC simulations of $d_{Ag}$ plotted in Arrhenius form at 75% $Ag$ concentration for the temperature range 800 – 1300 K. . . . .	66
4.34	Migration energy of both $Au$ and $Ag$ for $Au - Ag$ as a function of $Ag$ concentration, which is obtained by the global fitting of kMC results to Eq. 3.11 for all temperatures and compositions. . . . .	67
4.35	Zipper effect: If the vacancy is bound to a region near the APB, this shows the easiest way to translate the APB. . . . .	70
4.36	(100) APB in $Ni_3Al$ . . . . .	71

4.37	(100) APB in $Ni_3Al$ with two non-movable region (blue shaded) on each side putting boundaries on the APB's motion perpendicular to its slip plane. . . . .	71
4.38	Visual definition of <i>layer</i> for the (100) APB $Ni_3Al$ sample. The first two planes (yellow shaded) are designated as <i>layer</i> number 1, the following two planes (green shaded) are designated as <i>layer</i> number 2, etc. The last two planes (red shaded) are designated as <i>layer</i> number 10. There are a total of ten <i>layers</i> . . . . .	72
4.39	Four sites of an FCC ( $L1_2$ ): Site 1 (S1), Site 2 (S2), Site 3 (S3) and Site 4 (S4). . . . .	73
4.40	(100) APB positioned closer the right "wall" . . . . .	79
4.41	The position and the width of (100) APB for the initial configuration. . . . .	83
4.42	The first snapshot of the simulation running at $T = 1000$ K showing the position and the width of (100) APB. Number of <i>Al</i> atoms vs. layer number is plotted, the fitted <i>tanh</i> to site one and site three are also shown. . . . .	84
4.43	The second snapshot of the simulation running at $T = 1000$ K showing the position and the width of (100) APB. Number of <i>Al</i> atoms vs. layer number is plotted, the fitted <i>tanh</i> to site one and site three are also shown. . . . .	85
4.44	The third snapshot of the simulation running at $T = 1000$ K showing the position and the width of (100) APB. Number of <i>Al</i> atoms vs. layer number is plotted, the fitted <i>tanh</i> to site one and site three are also shown. . . . .	86
4.45	The fourth snapshot of the simulation running at $T = 1000$ K showing the position and the width of (100) APB. Number of <i>Al</i> atoms vs. layer number is plotted, the fitted <i>tanh</i> to site one and site three are also shown. . . . .	87
4.46	The fifth snapshot of the simulation running at $T = 1000$ K showing the position and the width of (100) APB. Number of <i>Al</i> atoms vs. layer number is plotted, the fitted <i>tanh</i> to site one and site three are also shown. . . . .	88

4.47	The sixth snapshot of the simulation running at $T = 1000$ K showing the position and the width of (100) APB. Number of $Al$ atoms vs. layer number is plotted, the fitted $\tanh$ to site one and site three are also shown. . . . .	89
5.1	1-D representation of the “sandtrap” for two energy valleys ( $\Delta E$ 's are not necessarily equal) as a function of displacement. . . . .	91



# Chapter 1

## Introduction

When approaching diffusion phenomena at the microscopic level, it becomes important to understand what microscopic mechanism is governing the migration of atoms from one lattice site to another. There are several mechanisms (see [HL64] for more details on these mechanisms): The first one is *direct* exchange of atoms (see Fig. 1.1), however this introduces large number of localized distortions. The second mechanism is the *ring* mechanism (see Fig. 1.2), where atoms migrate from one lattice site to another by series of migrations of neighboring atoms in a correlated manner. If there are spaces between atoms, *interstitial* positions can be used to enable the migration of atoms as another alternative mechanism (see Fig. 1.3). With the discovery of the Kirkendall effect [SE47], the *vacancy-assisted* mechanism has become more accepted for diffusion in solids, particularly for close-packed systems. This happens by the vacancy exchanging places with one of its nearest neighbors (see Fig. 1.4).

In the case of a binary alloy, as the vacancies continue to exchange places with the atoms nearby, the regular arrangement of atoms in the crystal starts to alter. During this process, several interesting diffusion limited processes have been

revealed, such as the translation of Anti Phase Boundary (APB).

APB is a planar defect that occurs in ordered alloys. While maintaining the crystallographic direction, the phase on each side of the boundary changes, i.e. ABABBABA (see Fig. 4.36). In Rong *et al.* [RJS94] work, it is observed that the vacancies, as they wander, accomplish a gliding effect of the APB perpendicular to its slip plane in  $Ni_3Al$ .

Even in the absence of a chemical composition gradient in the sample, due to the random thermal motions of atoms, atoms can move from one lattice site to another. Experimentally, the atoms to be traced are replaced by their isotopes. The coefficient obtained by this manner is called *tracer* diffusion coefficient.

To calculate these tracer diffusion coefficients for various binary alloys, a kinetic Monte Carlo code (*Pflame*) has been developed by *Dr. Murray S. Daw*. The code is written in *Fortran 90* and designed to work on parallel computers. The detail of the algorithms are discussed in Chapter 3: *Simulation*.

Using this code, we calculated the tracer diffusion coefficients for various binary alloys (such as weakly clustered  $Cu-Ni$ , and weakly ordered  $Au-Ag$ ) as a function of composition and temperature. Since these binary alloys are close-packed, the single vacancy mechanism is assumed to be the governing mechanism. Throughout our calculations, we kept the vacancy concentration fixed. The temperature interval is selected carefully to make sure that we are above the immiscibility gap. With the same technique, we also investigated the mobility and the spreading (width) of the APB in  $Ni_3Al$  as a continuation of the work of Harris *et al.* [HTDM06] to increase our understanding of these complex diffusion phenomena and diffusion limited processes.

During the calculations, particularly at lower temperatures, we found some configurations where the vacancy was trapped. We called this the *sandtrap*. The statistical averages were affected by these sandtraps. In a typical sandtrap, the va-

cancy moves back and forth between two configurations accomplishing nothing, while simulation time is accumulated. We didn't come across these configurations in the APB calculations because of the high temperature range we picked. We developed a systematic approach to overcome this problem (see Chapter 5: *Sandtrap Limitation and How to Overcome it*).

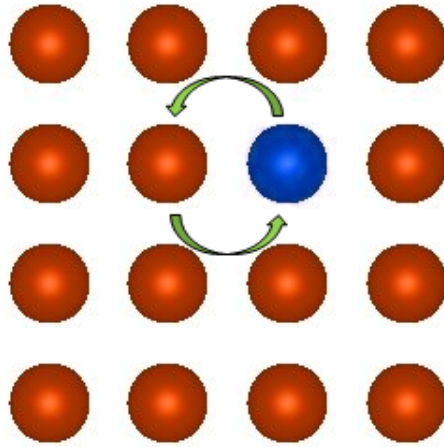


Figure 1.1: Direct exchange mechanism: Two atoms swap places. This introduces a local distortion in the lattice.

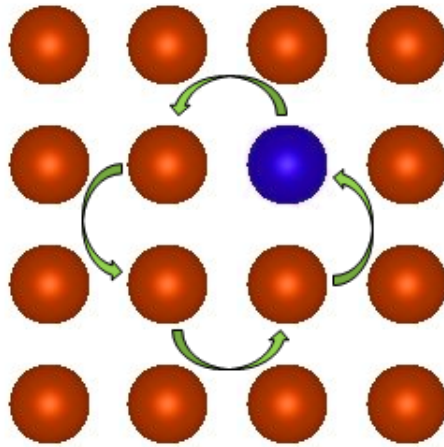


Figure 1.2: Ring mechanism: In order to observe a migration of an atom, the atoms need to move in a correlated manner.

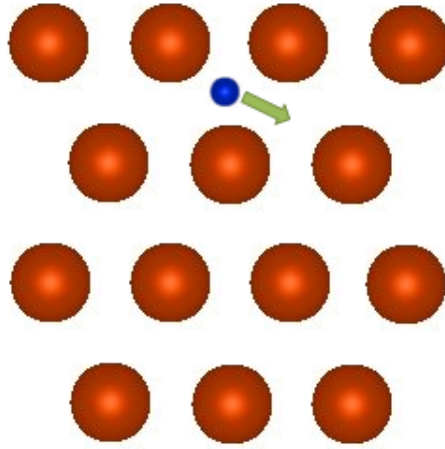


Figure 1.3: Interstitial mechanism: If there are spaces between atoms, those spaces can be used by smaller atoms to migrate.

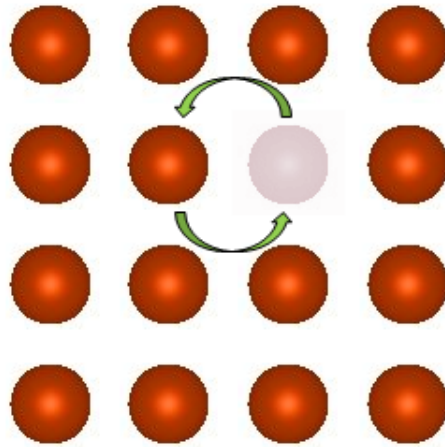


Figure 1.4: Single vacancy mechanism: Vacancy exchanges places with one of its nearest neighbors.

# Chapter 2

## Theory

In this chapter, the necessary formalism for calculating the tracer diffusion coefficient in the Pflame code is presented. The implementation of the theory is discussed in Chapter: 3: *Simulation*.

Let's consider a well-annealed sample of a pure metal. Even though nothing is observed macroscopically, the atoms in the sample are still diffusing at a rate depending on the temperature. When a radioactive atom of the same type as the host is introduced as a tracer, provided that no chemical composition gradient is imposed, the resulting diffusion coefficient is called the *tracer diffusion coefficient* and usually designated by the symbol  $D^*$ . The tracer atom is chemically identical with the host, so it is sometimes called the *self-diffusion coefficient* as well.

In order to observe diffusion in a macroscopic scale for a substance, a concentration gradient needs to be introduced. In the presence of a such a concentration gradient, one will observe a flux of substance in the opposite direction to the concentration gradient. The proportionality coefficient between the flux and the concentration gradient is called the *diffusion coefficient*. This law is known as *Fick's First Law*

of diffusion [Fic55], and written as,

$$\vec{J} = -D \vec{\nabla} C \quad (2.1)$$

where  $C$  is the concentration,  $D$  is the diffusion coefficient, and  $\vec{J}$  is the flux. If the concentration changes with time, then one can use the continuity equation,

$$\vec{\nabla} \cdot \vec{J} = -\frac{\partial C}{\partial t} \quad (2.2)$$

with Eq. 2.1 to derive,

$$\vec{\nabla} \cdot (-D \vec{\nabla} C) = -D (\nabla^2 C) - (\vec{\nabla} D) \cdot (\vec{\nabla} C) = -\frac{\partial C}{\partial t} \quad (2.3)$$

Eq. 2.3 is known as *Fick's Second Law* of diffusion [Fic55]. If the diffusion coefficient,  $D$ , doesn't depend on the concentration, then Eq. 2.3 can be written as

$$D (\nabla^2 C) = \frac{\partial C}{\partial t}. \quad (2.4)$$

Once the initial boundary conditions are established, Eq. 2.4 can be solved for  $C(x, t)$ . The diffusion coefficient can then be found by fitting the experimental  $C(x, t)$  to the analytical  $C(x, t)$ . However, if the diffusion coefficient depends on the concentration, which is frequently the case, then one can look for a solution for  $D = D(C)$  by using the Boltzmann-Matano analysis [Bol94, Mat33].

To get more insight into the diffusion phenomena, one needs to understand it through a thermodynamic point view. The phenomenological equations of irreversible thermodynamics present a unifying framework to understand these diffusion phenomena in solids (see, for example [HL64, Ant75, Fre75]). The transport properties of

a solid, such as the tracer diffusion coefficient, can be expressed in terms of phenomenological coefficients [HL64]. During the derivation of the equations, we restrict ourselves to isothermal, isobaric diffusion under no external forces (such as magnetic field or electric field), and the *Onsager reciprocity theorem* is governing when expressing the linear laws of transport as relations between the fluxes and thermodynamic forces. Thus the flux can be written in terms of phenomenological coefficients and forces as

$$\vec{J}_i = \sum_k^n L_{ik} \vec{X}_k, \quad (2.5)$$

where  $\vec{J}_i$  is the flux of the  $i$ th species of an  $n$  species system,  $L$ 's are the phenomenological coefficients, and  $\vec{X}$ 's are the thermodynamic driving forces on the system which is written as

$$\vec{X}_k = -\vec{\nabla}(\mu_k)_T, \quad (2.6)$$

where  $\mu_k$  is the chemical potential of the species  $k$ .

In the case of a binary alloy, where there are two species: atom type  $A$  and atom type  $B$ , the diffusion rates of type  $A$  and type  $B$  are usually not equal to each other, since their self-diffusion coefficients are different. The effects arising from the gradient of chemical composition also play a role in their diffusion rates. The diffusion coefficient of the individual type, in this case, is called the *chemical* diffusion coefficient, and it is measured relative to the local lattice. The difference in the diffusion rates causes a net flux of atoms, so if one places insoluble markers in the sample, one observes the motion of the markers relative to the lab frame. This effect is known as the Kirkendall effect [SE47]. Kirkendall's experiment also proved the existence of vacancy diffusion in the vast majority of the metallic materials.

In order to find a relationship between phenomenological coefficients and the tracer diffusion coefficients for a homogenous binary alloy, and say, the vacancy mech-



anism is operating, we must first describe the fluxes by using Fick's Law, Eq 2.1, and then describe the fluxes in terms of phenomenological coefficients using Eq. 2.5. Equating these two gives a relationship between phenomenological coefficients and the chemical diffusion coefficients. By using Darken's equation [Dar48], we can then relate the chemical diffusion coefficients to tracer diffusion coefficients for a homogeneous alloy.

From Eq. 2.1, the fluxes are

$$\begin{aligned} J_A &= -D_A \frac{\partial C_A}{\partial x} \\ J_B &= -D_B \frac{\partial C_B}{\partial x}, \end{aligned} \tag{2.7}$$

(for simplicity, the vector signs are dropped and only the  $x$  direction is taken.) where  $C$ 's are the concentrations, and  $D$ 's are the diffusion coefficients of type  $A$  and type  $B$ .

Meanwhile, using Eq. 2.5, we can write

$$\begin{aligned} J_A &= L_{AA}X_A + L_{AB}X_B \\ J_B &= L_{BA}X_A + L_{BB}X_B. \end{aligned} \tag{2.8}$$

Actually, the vacancies should enter here as another species so that the fluxes are written as

$$\begin{aligned} J_A &= L_{AA}X_A + L_{AB}X_B + L_{AV}X_V \\ J_B &= L_{BA}X_A + L_{BB}X_B + L_{BV}X_V, \end{aligned} \tag{2.9}$$

and from the conservation of lattice sites,

$$J_V = -(J_A + J_B), \tag{2.10}$$

however, if the sources and sinks for the vacancies are numerous in the sample, then

it can be assumed that vacancies are at equilibrium and  $X_V = 0$ .

The Gibbs-Duhem equation [Jan76] states that the thermodynamic intensive properties are not independent, but related. For a system restricted to isothermal and isobaric diffusion, this imposes a restriction upon the forces,  $X$ 's, of the form

$$\sum_k^n C_k X_k = 0, \quad (2.11)$$

where  $C_k$  is the concentration of species  $k$ ,

$$C_A X_A + C_B X_B = 0, \quad (2.12)$$

Eq. 2.8 can be re-written as

$$\begin{aligned} J_A &= \left( L_{AA} - \frac{C_A}{C_B} L_{AB} \right) X_A \\ J_B &= \left( \frac{C_B}{C_A} L_{BA} - L_{BB} \right) X_B. \end{aligned} \quad (2.13)$$

The chemical potential of type  $A$  and type  $B$  is

$$\begin{aligned} \mu_A &= \mu_A^0 + kT \ln(C_A \gamma_A) \\ \mu_B &= \mu_B^0 + kT \ln(C_B \gamma_B), \end{aligned} \quad (2.14)$$

where  $k$  is the Boltzmann constant,  $T$  is the temperature, and the  $\gamma$ 's are the factors to account for deviations from the ideal behavior in a mixture and they are known as the activity coefficients. Using Eq. 2.14 in Eq. 2.6, we can write the forces as

$$\begin{aligned} X_A &= -\frac{kT}{C_A} \frac{\partial C_A}{\partial x} \left( 1 + \frac{\partial \ln \gamma_A}{\partial \ln C_A} \right) \\ X_B &= -\frac{kT}{C_B} \frac{\partial C_B}{\partial x} \left( 1 + \frac{\partial \ln \gamma_B}{\partial \ln C_B} \right). \end{aligned} \quad (2.15)$$

Re-writing Eq. 2.13 by using Eq. 2.15 gives

$$\begin{aligned} J_A &= -kT \left( \frac{L_{AA}}{C_A} - \frac{L_{AB}}{C_B} \right) \left( 1 + \frac{\partial \ln \gamma_A}{\partial \ln C_A} \right) \frac{\partial C_A}{\partial x} \\ J_B &= -kT \left( \frac{L_{BA}}{C_A} - \frac{L_{BB}}{C_B} \right) \left( 1 + \frac{\partial \ln \gamma_B}{\partial \ln C_B} \right) \frac{\partial C_B}{\partial x}. \end{aligned} \quad (2.16)$$

By comparing Eq. 2.16 with Eq. 2.7, the diffusion coefficients can be written as

$$\begin{aligned} D_A &= \frac{kT}{N} \left( \frac{L_{AA}}{C_A} - \frac{L_{AB}}{C_B} \right) \left( 1 + \frac{\partial \ln \gamma_A}{\partial \ln C_A} \right) \\ D_B &= \frac{kT}{N} \left( \frac{L_{BA}}{C_A} - \frac{L_{BB}}{C_B} \right) \left( 1 + \frac{\partial \ln \gamma_B}{\partial \ln C_B} \right), \end{aligned} \quad (2.17)$$

where  $N$  is the total number of atoms per unit volume.

Darken [Dar48] tried to relate the chemical diffusion coefficient to tracer diffusion in a homogenous alloy. Since the phenomenological coefficients,  $L$ 's, do not depend on the gradients of composition, it can be assumed that the average velocity of one type per unit force due to the chemical composition gradient is equal to the average velocity of that type's isotope per unit force due to the chemical composition gradient in a homogenous alloy,

$$\frac{J_{A^*}}{C_{A^*} X_{A^*}} = \frac{J_A}{C_A X_A}, \quad (2.18)$$

or

$$\frac{J_{B^*}}{C_{B^*} X_{B^*}} = \frac{J_B}{C_B X_B}, \quad (2.19)$$

where (\*) represents the isotope of the type. Using Eq. 2.18 and Eq. 2.19, Eq. 2.13 can be written for the isotopes as

$$\begin{aligned} J_{A^*} &= \frac{C_{A^*}}{C_A} \left( L_{AA} - \frac{C_A}{C_B} L_{AB} \right) X_{A^*} \\ J_{B^*} &= \frac{C_{B^*}}{C_B} \left( \frac{C_B}{C_A} L_{BA} - L_{BB} \right) X_{B^*}. \end{aligned} \quad (2.20)$$

Using Eq. 2.14 in Eq. 2.6 with the  $\gamma$ 's set to unity, since isotope  $A^*$  is chemically identical to type  $A$ , and isotope  $B^*$  is chemically identical to type  $B$ , we can write the forces as

$$\begin{aligned} X_{A^*} &= -\frac{kT}{C_{A^*}} \frac{\partial C_{A^*}}{\partial x} \\ X_{B^*} &= -\frac{kT}{C_{B^*}} \frac{\partial C_{B^*}}{\partial x}. \end{aligned} \quad (2.21)$$

Then Eq. 2.20 becomes

$$\begin{aligned} J_{A^*} &= -kT \left( \frac{L_{AA}}{C_A} - \frac{L_{AB}}{C_B} \right) X_{A^*} \\ J_{B^*} &= -kT \left( \frac{L_{BA}}{C_A} - \frac{L_{BB}}{C_B} \right) X_{B^*}, \end{aligned} \quad (2.22)$$

and therefore the tracer diffusivity coefficients for a homogenous binary alloy can be written as

$$\begin{aligned} D_{A^*} &= \frac{kT}{N} \left( \frac{L_{AA}}{C_A} - \frac{L_{AB}}{C_B} \right) \\ D_{B^*} &= \frac{kT}{N} \left( \frac{L_{BA}}{C_A} - \frac{L_{BB}}{C_B} \right) \end{aligned} \quad (2.23)$$

What makes the phenomenological approach appealing is the fact that phenomenological coefficients don't depend on the driving force, but only on temperature and composition. If these coefficients are determined somehow, maybe one can not control the diffusion behavior, but at least one can predict the behavior under different thermodynamic forces acting on the system. The phenomenological coefficients can be expressed in terms of atomistic Einsteinian formulae [All82],

$$L_{ij} = \lim_{V \rightarrow \infty} \lim_{t \rightarrow \infty} (6VkTt)^{-1} \langle \Delta \vec{R}^{(i)}(t) \cdot \Delta \vec{R}^{(j)}(t) \rangle, \quad (2.24)$$

where  $\Delta \vec{R}^{(i)}(t)$  is the sum of all the displacements of type  $i$  atoms in time  $t$ ,  $k$  is the Boltzmann constant,  $T$  is the temperature and  $V$  is the volume. The angular brackets denote the thermal average. In a computer simulation, the position of the each atom can be stored. By comparing the initial configuration with the final configuration, one

can easily calculate the sum of all displacements of each type of atom. Eq. 2.24 enables us to calculate the phenomenological coefficients, the  $L$ 's, directly from the simulation. Once the  $L$ 's are calculated, the tracer diffusion coefficients can be calculated by using Eq. 2.23.

When an atom near a vacancy acquires sufficient thermal energy, it can pass over the energy barrier and exchange sites with the vacancy. The probability,  $P$ , of an atom crossing this energy barrier is given by Boltzmann factor,

$$P \propto e^{-E_a/kT}, \quad (2.25)$$

where  $k$  is the Boltzmann constant,  $T$  is the temperature, and  $E_a$  is the activation energy, which consists of two parts:

$$E_a = E_f + E_m, \quad (2.26)$$

where  $E_f$  is the formation energy and  $E_m$  is the migration energy. The formation energy is the necessary energy to bring one atom from the interior of the sample to the surface and form a vacancy. In the simulations, we start with the configurations in which the vacancy is already formed, thus  $E_f = 0$  and  $E_a = E_m$ . The calculation of the migration energies, along with the algorithm of the simulation, is discussed in Chapter: 3: *Simulation*.

# Chapter 3

## Simulation

With the advancement of computer technologies, doing simulations of diffusion phenomena has become more appealing. However, diffusion in solids, unlike in gases or liquids, is a very slow process due to the fact that the forces between molecules and atoms are generally so large that there are only infrequent exchanges of positions. These atomic jumps are activated processes, which means that in order to observe a jump, a certain energy barrier needs to be crossed (*saddlepoint* energy). Methods which integrate the equations of motion, as in Molecular Dynamics (MD), are not feasible due to the timescale. For an accurate calculation of those integrals, the time step needs to be in the order of  $fs$ . Even with the fastest computers today, only a fraction of  $\mu s$  can be reached, which unfortunately, leaves a gap of several orders of magnitude between experiments and simulations.

This known issue of time scale of MD can be overcome by Accelerated Molecular Dynamics (AMD) [VMG02] using the kinetic Monte Carlo (kMC) technique. However, the list of all possible configurations and rates of transition are commonly known in advance. Provided that the harmonic approximation to Transition State Theory (hTST) holds, then the rates of transitions can be calculated using  $k =$

$\nu_0 \exp(-E/k_b T)$  where  $\nu_0$  is the prefactor,  $k_b$  is the Boltzmann constant,  $T$  is the temperature and  $E$  is the activation energy. The challenge in here is to find the the saddlepoint energies. There are several methods to find the saddlepoint energies: Provided that the initial configuration is known, the Dimer Method [HJ99] can be used. An alternative to the Dimer Method is the Nudged Elastic Band Method (NEB) [HJ00], if the final configuration is also known along with the initial configuration. The energetics necessary for Pflame kinetic Monte Carlo code are obtained by Embedded Atom Method (EAM) [DB84, Daw89] (see Sec. 3.1: *Embedded Atom Method (EAM)*).

In the earlier versions of the code, the Dimer Method is used to find the saddlepoint energies with good results in Harris *et al.* [HTDM06]. Harris *et al.* calculated the tracer diffusion coefficients in  $Ni_3Al$  as functions of temperature and composition. At temperatures below about 1000 K, they found that diffusivity is a sharp function of composition, and at 76 at.% Ni, their calculations show a dip. The experiments agree with this behavior, however, it is observed below about 1300 K. They also observed in their calculations that the diffusivity, in general, shows an Arrhenius behavior with few exceptions which show deviations from this behavior. However, they couldn't confirm or deny these deviations due to high statistical errors. The experiments carried out by Shi *et al.* at 1200 K agrees with these deviations.

With these earlier versions of Pflame, we investigated the motion of the APB. However, the motion of the APB is an extremely slow process compared to individual displacement of atoms, thus some performance improvements were necessary to the code. In the later versions, due to our better understanding of possible configurations of the binary alloys we were working on, a method more akin to NEB is used (see Sec 3.2: *Saddlepoint Search*). The applications of the simulation are presented in Chapter 4: *Results*.

### 3.1 Embedded Atom Method (EAM)

The total energy of a solid can be calculated by solving the many-electron Schrodinger equation, however this is a very overwhelming task. Certain approximations need to be made to simplify the calculations while retaining the physics of the solid. One of the simplest approximations is the pair potential model, where the total energy,  $E_c$ , can be approximated to be

$$E_c = E_0 + \frac{1}{2} \sum_{i,j} V_2^{eff}(\vec{R}_i - \vec{R}_j) \quad (3.1)$$

where  $V_2^{eff}(\vec{R}_i - \vec{R}_j)$  is an effective pair potential [Car90]. In this approximation, the strength of a bond is not affected by the presence of the other bonds, thus neglecting a very important physics of metallic bonding. In the pair potential model,  $E_c$  scales linearly with the coordination number,  $Z$ . However, in reality it scales more closely to  $\sqrt{Z}$  (see [Har06] for  $E_c$  vs. coordination number,  $Z$ , in  $Ni_3Al$ ).

The Embedded Atom Method (EAM) [DB83, DB84] is a semi-empirical potential which is used to calculate the total energy of a metallic system. EAM is a great improvement over the pair potential model because it includes the many-atom interactions, which are neglected by the pair potential model. The total energy in EAM can be written as

$$E_{tot} = \sum_i G_i(\rho_{h,i}) + \frac{1}{2} \sum_{i,j \neq i} \phi_{ij}(R_{ij}) \quad (3.2)$$

where  $G$  is the embedding energy which is defined as the interaction of the atom with the background electron gas [DFB93],  $\rho$  is the linear superposition of the electron densities of the host atoms,  $\phi$  is the two-atom electrostatic potential, and  $R_{ij}$  is the distance between atoms  $i$  and  $j$ .



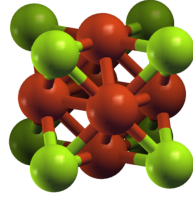


Figure 3.1:  $A_3B$  FCC ( $L1_2$ ) structure. Each atom has 12 nearest neighbors.

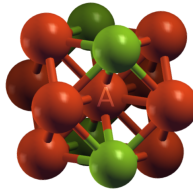


Figure 3.2: 12 nearest neighbor of atom  $A$ : 4  $B$ 's and 8  $A$ 's.

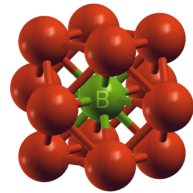


Figure 3.3: 12 nearest neighbor of atom  $B$ : 12  $A$ 's.

The embedded energy,  $G$ , and  $\phi$  are fitted to bulk properties empirically.

The Embedded Atom Method has been applied successfully to many different problems (see [DFB93] *p.257* for the list of the references). The fact that it is computationally less intensive than other approximations, such as the local density approximation, and due to its successful applications, we chose EAM to calculate the energetics in our simulations.

## 3.2 Saddlepoint Search

In the earlier versions of the code Pflame, as a general scheme of finding the saddlepoint energies, the Dimer Method [HJ99] is used with great success [HTDM06]. However, this part of the code is computationally intensive. Because of the straightforward nature of the motion of the vacancy in a close-packed FCC binary alloy, a faster search algorithm more akin to the Nudged Elastic Band (NEB) [HJ00] is implemented in later versions.

**Dimer Method:** The Dimer Method [HJ99] is one of the most commonly used surface-walking algorithms to find the saddlepoints on an energy surface. Its advantage over the Nudged Elastic Band (NEB) Method (see below) is that the Dimer Method requires only the initial state and initial direction. However this method is computationally more intensive.

The Dimer Method involves working with two images in configuration space of the system separated by some fixed distance. These two images are referred as “dimer”. The dimer can be thought of as a dumbbell. The idea is, starting from a point at the vicinity of the potential energy minimum, to climb up the potential energy surface until a saddlepoint is found. This method involves two steps. In the

first step, the dimer's center is fixed in space but allowed to rotate about its center axis to minimize its energy. In the second step, the dimer is translated along a modified force,  $\vec{F}^U$ .

$$\vec{F}^U = \vec{F}_R - 2\vec{F}_N \quad (3.3)$$

where  $\vec{F}_R$  is the net translational force pulling the dimer towards a minimum and  $\vec{F}_N$  is the force along the direction of the lowest curvature (see, Fig. 3.4). The movement of the dimer along this modified force will bring it to a saddlepoint.

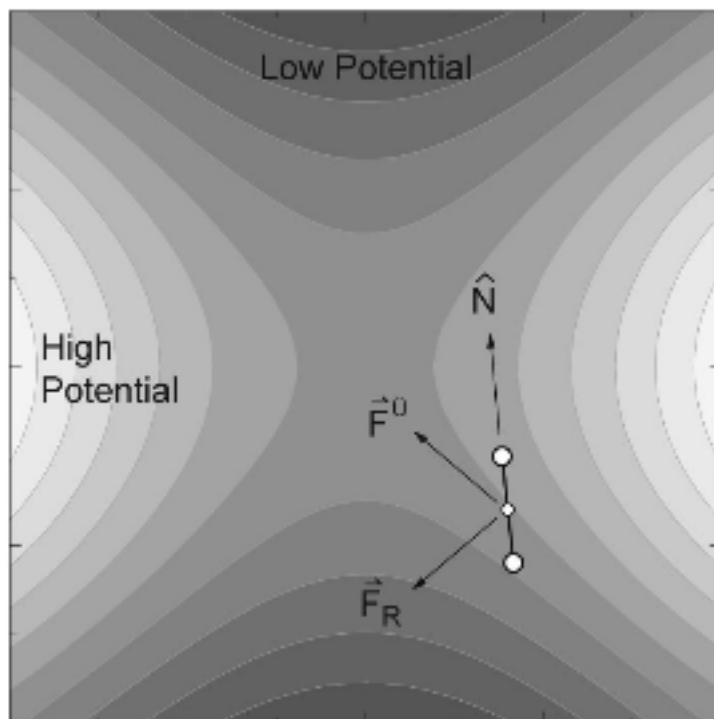


Figure 3.4: 2-D visualization of dimer near saddlepoint (image taken from [HJ99]).

**Modified Nudged Elastic Band Method:** The other most commonly used method is the Nudged Elastic Band (NEB) Method [HJ00]. This is a very efficient way of finding the minimum energy path (MEP) on the potential energy surface provided that initial and final states are given.

In this method, we need to construct points along the path which connects these two states (initial and final). These states are assumed to be known prior to applying the NEB Method. To ensure the continuity of the path, we then attribute a spring force between adjacent points. Minimization of the forces acting on this band brings it to MEP. Only the parallel component of the spring forces and the perpendicular component of the true forces to the path are used. The main reason for using these components is to ensure that the spring forces are not interfering with

the convergence of the band.

In the original formalism, the tangent at point  $i$  on the path is estimated from two adjacent points,  $i - 1$  and  $i + 1$ . In some cases, this introduces the problem called a “kink”, when the parallel forces are much larger than the perpendicular forces, and when many points are used (see, Fig. 3.5). Henkelman *et al.* [HJ00] modified the tangent to eliminate these kinks (see, Fig. 3.6). They used point  $i$  and one of the adjacent points which is higher in energy to estimate the tangent at point  $i$ . However, if both of the adjacent points are either lower in energy, or both higher in energy than point  $i$ , then the weighted average of the adjacent points is used.

In the later versions of Pflame, the saddlepoint search scheme has been simplified and accelerated from the earlier work [HTDM06]. Because of the straightforward nature of the motion of the vacancy in a close-packed FCC binary alloy, we chose to implement a faster search algorithm more akin to the Nudged Elastic Band. In the present scheme, it is straightforward to find the beginning configuration and 12 neighboring (see Fig. 3.1) ending configurations for a vacancy hop. Once the 12 neighbors of the vacancy are identified, one of the neighboring atoms (migrant atom) is gradually moved along the vector towards the vacancy. While moving the migrant atom, at each step the system is relaxed and the energy of the system is calculated. In these relaxations, while every atom is free to move in any direction, the migrant atom is only allowed to move perpendicular to the initial direction vector. The energy of the system, as the migrant atom moves towards the vacancy, crosses the saddlepoint. This process is repeated for the remaining 11 neighboring atoms, and the saddlepoint energies are sampled.

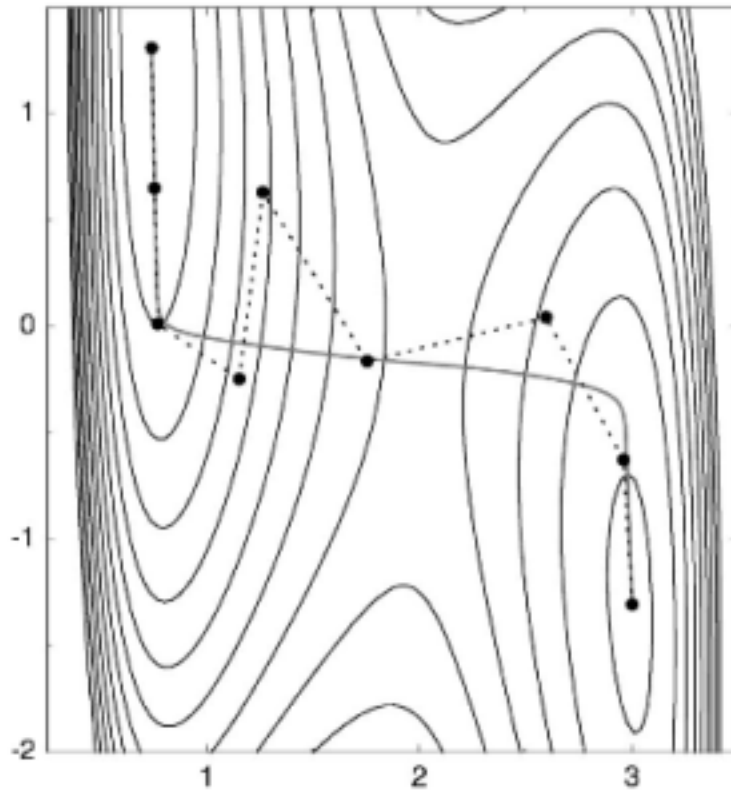


Figure 3.5: Using the original NEB equations can develop kinks along the path (image taken from [HJ00]).

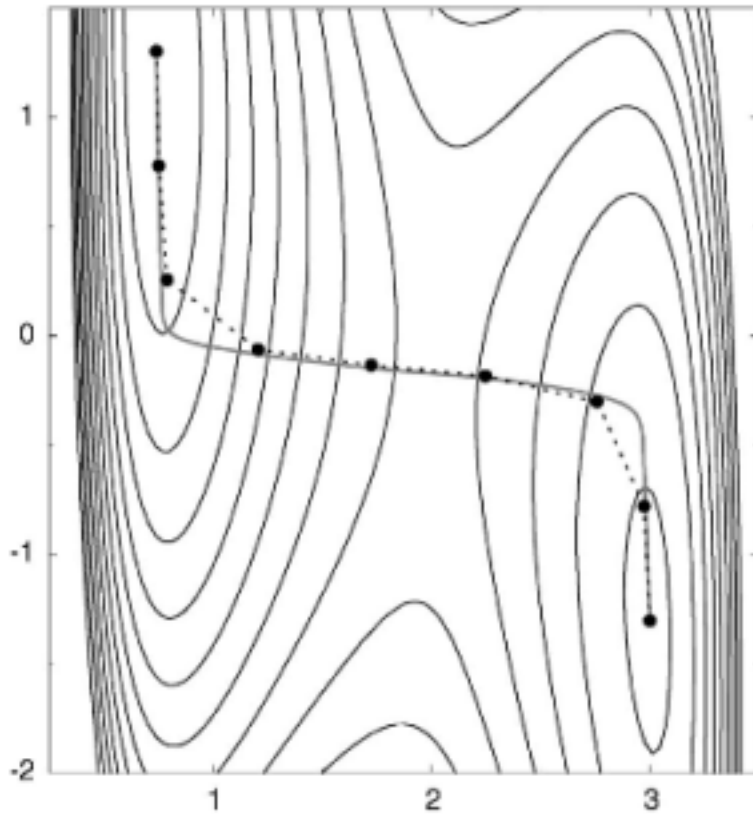


Figure 3.6: Using the modified tangents does not develop kinks along the path and converges smoothly (image taken from [HJ00]).

### 3.3 On-the-fly kinetic Monte Carlo Simulation

Kinetic Monte Carlo has been a useful tool for decades (see, for example [FW91]). Where there are well-defined valleys in the energy surface separated by simple saddlepoints, the approach associates all the exits from a valley with a probability (see, Eq. 2.25)

$$p_i \propto e^{-\frac{\Delta E_i}{k_B T}} \quad (3.4)$$

where the  $\Delta E_i$  is the energy barrier to be crossed for that exit (see, Fig. 3.7) and  $C$  is the normalization constant. From that list is then selected, randomly according to the weights  $p_i$ , a single exit. That exit is taken, leading to new valley, and the time is incremented by

$$dt = \tau e^{+\frac{\Delta E_i}{k_B T}} \quad (3.5)$$

For most metals the characteristic time scale  $\tau$  is on the order of 1 ps [Har06]. The exact value of this constant is unimportant at the moment, because we are only interested in the trends of the diffusion constant with changing temperature and composition and not exact values.

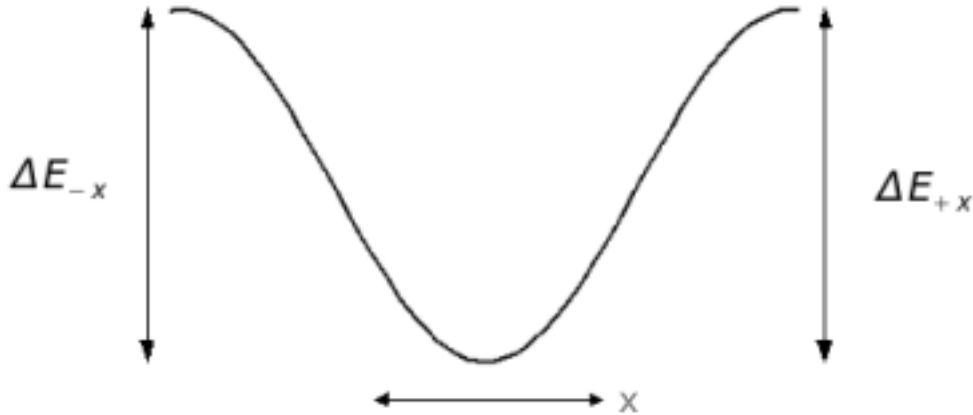


Figure 3.7: 1-D energy-valley with 2 exits as a function of displacement.  $\Delta E_{+x}$  and  $\Delta E_{-x}$  are the saddlepoint energies to exit the valley.  $\Delta E_{+x}$  is usually not equal to  $\Delta E_{-x}$ .

The majority of Monte Carlo simulations of similar systems use a predefined table of saddlepoint energies which the vacancy will encounter. This method is successful when considering mono-elemental crystals and other systems where there is a narrow range of saddlepoint energies encountered by the vacancy. However, if the



necessary saddlepoint energies can not be categorized in a simple way, then it may become necessary to calculate saddlepoint energies on the fly (see, for example [HJ01]).

In the present calculation, because of the effects of the temperature and stoichiometry, we are concerned with the influence of local composition on vacancy migration. We tested the dependence of vacancy migration saddlepoint energies in FCC-based alloys on the local composition near the vacancy. We found that compositional variations in the shell of fifth neighbors of the vacancy can have non-negligible effects on the saddlepoint energies. This is understandable if one considers neighbors of the atom which is exchanging with vacancy: a second neighbor of that atom is a fifth neighbor to the vacancy. This means that in constructing a pre-defined event table, one must consider various configurations of anti-site defects out to fifth neighbors of the vacancy. The number of possible configurations in that case is quite large to be stored and re-used efficiently, making a pre-defined event table impractical.

The energetics for kinetic Monte Carlo is obtained in this work by the Embedded Atom Method (EAM) [DFB93, FBD86], which is a semi-empirical many-atom description of metallic bonding. The overall accuracy of the simulations depends upon the ability of EAM functions we have used to calculate the energies of the crystal configurations. EAM allows fairly quick computing of these energies which makes our method of on-the-fly kinetic Monte Carlo possible. The accuracy of these functions could be tested with more accurate simulations such as VASP which fully take into account the electronic structure of the solid. We used periodic boundary conditions, and usually used supercells of 256 atoms. The lattice constants were optimized for each composition. In the present calculations, we did not account for thermal expansions.

We also kept the vacancy concentration fixed (one vacancy per cell) throughout the calculations. This means that direct interaction between two or more vacancies

is not allowed. It would be interesting in future research to create cells with two or more vacancies in order to see if the vacancies interact with each other or merely ignore each other. It is important to recall this factor because the tracer diffusivity should be proportional to the vacancy concentration which is a function of temperature and composition. This must be remembered when comparing to experiment. In particular, if the assumption of single vacancy assistance holds, then the tracer diffusivity should be proportional to the vacancy concentration,

$$D_A = [c_v]Nd_A \quad (3.6)$$

(\* is dropped for simplicity) where  $d_A$  is the result of the present calculation,  $N$  is the number of sites in our calculational cell, and  $[c_v]$  is the correct vacancy concentration (per site) for a given composition and temperature. The equilibrium vacancy concentration could be calculated self-consistently within our approach using equilibrium Monte Carlo (eMC).

To carry out the kinetic Monte Carlo calculations, *Dr. Murray S. Daw* has developed a parallel code Pflame tailored to a Beowulf<sup>1</sup> architecture. Pflame is similar in design to the earlier Sandia Dynamo code written for vector architecture. The new implementation is written in F90, and uses straightforward MPICH<sup>2</sup> communications between the processes. For the present application, we have found the most efficient strategy to be one in which the 12 saddlepoint searches are performed in parallel. All processes communicate the saddlepoint energies to the master, which picks and announces the kinetic Monte Carlo “winner”, and the winning processor then broadcasts the ending configuration of its jump to all processes, and the next

---

<sup>1</sup>“Beowulf clusters are scalable performance clusters based on commodity hardware, on private system network, with open source software (Linux) infrastructure.” – [www.beowulf.org](http://www.beowulf.org)

<sup>2</sup>MPICH is a freely available, portable implementation of MPI (Message Passing Interface), which allows the parallelism of the program codes using networked machines.

kinetic Monte Carlo step begins.

By comparing the initial and final configurations, we calculate the displacements of the two types and also the vacancy, and from that, we compute the kinetic coefficients and the corresponding tracer diffusivities. The tracer diffusion coefficients for type  $A$  and type  $B$  in a homogenous A-B alloy is given by Eq. 2.23, respectively, where the kinetic coefficients (phenomenological coefficients),  $L_{ij}$  are calculated from the net displacements of each type (see, Eq. 2.24).

Before we run kinetic Monte Carlo, we equilibrate each configuration using equilibrium Monte Carlo (eMC) as a preparatory step. This eMC procedure consists of two mechanisms. The first mechanism involves swapping the types of two randomly chosen atoms. The second mechanism is to add a random displacement to a randomly picked atom. One of those two mechanisms is selected randomly at each step. The new configuration is either accepted or rejected according to the metropolis algorithm [MRR<sup>+</sup>53].

After equilibrating the configurations, we created 10 samples per temperature per concentration with one vacancy, such that the position of the vacancy is selected randomly. This approach is intended to give a better statistics and also to avoid some configurational traps which we call *sandtrap* (see Chapter 5: *Sandtrap Limitation and How to Overcome it*). We ran kMC with 500 steps for each sample and used sub-averaging to determine statistical error.

We also monitor the long-range order (LRO) and short-range order (SRO). The former is quickly obtained by calculating the structure factor

$$S(\vec{G}) = \sum_j e^{i\vec{G}\cdot\vec{R}_j} \quad (3.7)$$

for these types of reciprocal lattice vectors:  $\vec{G} = \frac{2\pi}{a}\{1\ 0\ 0\}$ ,  $\frac{2\pi}{a}\{0\ 1\ 1\}$ ,  $\frac{2\pi}{a}\{1\ 1\ 1\}$ . The

intensities are then used to monitor the ordering, such as tendency to  $L1_2$  or  $L1_0$ .

If  $C_{AA}$  is the probability of finding type  $A$  atom near type  $A$  atom,  $C_{BB}$  is the probability of finding type  $B$  atom near type  $B$  atom, and  $C_{AB}$  is the probability of finding type  $A$  atom near type  $B$  atom (which is also equal to  $C_{BA}$ ), then the sum rule gives

$$C_{AA} + 2C_{AB} + C_{BB} = 1. \quad (3.8)$$

For a given composition,  $x$ , of a random occurrence, we can write

$$x^2 + 2x(1 - x) + (1 - x)^2 = 1, \quad (3.9)$$

and by comparing Eq. 3.8 with Eq. 3.9, we find  $C_{AB}$  to be  $x(1 - x)$ .

In Pflame, SRO is calculated by counting the number of nearest neighbor pairs of unlike type and comparing to what would be expected from a random occurrence at the known composition,

$$C_{AB} - x(1 - x). \quad (3.10)$$

If the binary alloy is clustering, then Eq. 3.10 will be negative. If the binary alloy is ordering, then Eq. 3.10 will be positive.

We analyzed the calculated diffusivities over the full range of composition and temperature. We found that we could get a good representation of all the results by a simple linear variation of the migration energy with composition. To demonstrate this, we fit the results for all temperature and compositions to a pre-exponential of the form

$$d(x, T) = d_0 e^{-\frac{E_m(x)}{kT}}, \quad (3.11)$$

where  $d(x, T)$  is the calculated tracer diffusivity as a function of composition  $x$  and temperature  $T$ ,  $d_0$  is a constant prefactor and  $E_m(x)$  is the migration energy. The

lower case  $d$  is used as a reminder that the vacancy concentration is held fixed at the same value for all compositions and temperatures. In applying the fit, within the statistical uncertainties of our simulations, a linear function was sufficient to describe  $E_m(x)$ .

It is best here to emphasize that the goal in the present work is the development of the parallel implementation of the on-the-fly kinetic Monte Carlo for diffusion in binary alloys, and to note that some work remains to be done to enable a complete comparison to experiment. In particular, the overall time scale  $\tau$  of Monte Carlo steps is not yet determined. In the previous work [HTDM06] on  $Ni_3Al$ , the value of  $\tau$  was determined by fitting to one experimental data point. It is also possible to employ a more fundamental theory, such as transition state theory [Cha78, MCB79], to determine  $\tau$ , which would probably show some dependence on the local environment. That step is left undone in the present case, choosing instead to emphasize the development of the parallel saddlepoint search and the extension to a wider range of materials. In addition, we also note that the vacancy concentration is fixed in these calculations. For this we can not yet make direct comparison to experimental diffusivities. However, the ratio of the component tracer diffusivities in each binary is independent of  $\tau$  and the vacancy concentration.

# Chapter 4

## Results

In this chapter, the results of on-the-fly kinetic Monte Carlo applied to weakly clustered ( $Cu-Ni$ ) and weakly ordered ( $Au-Ag$ ) alloys are presented. In the last section, a further investigation of the Anti-Phase Boundary (APB) in a strongly ordered alloy,  $Ni_3Al$  is made as a continuation of the work of Harris *et al.* [HTDM06]. The discussion regarding these results is given in Chapter 6: *Conclusions and Discussion*.

### 4.1 Bulk Tracer Diffusivity for $Cu - Ni$

The on-the-fly kinetic Monte Carlo technique described in the previous chapter is used to calculate the bulk tracer diffusivity in a weakly clustered alloy,  $Cu - Ni$  as a function of composition and temperature. Twenty different values of  $Cu$  concentrations were picked between 5% and 90%. Extreme compositions are excluded. When there are very few minority atoms, and only a single vacancy, the minority atoms are not given much chance to move around, thus causing poor statistics.

The temperatures were chosen in the interval 700 – 1300 K. Those temperatures were deliberately chosen to be well above the immiscibility temperature (see

Fig. 4.1). The estimation of the critical temperature for clustering, based on the equilibrium Monte Carlo calculations, is well below the temperatures of the simulation. Within this temperature range,  $Cu - Ni$  remains weakly clustering. The degree of ordering was verified by calculating long-range ordering (LRO) and short-range ordering (SRO). The long-range ordering over the range of temperatures and concentrations is negligible. However, some weak dependence of short-range order on temperature and concentration is observed.

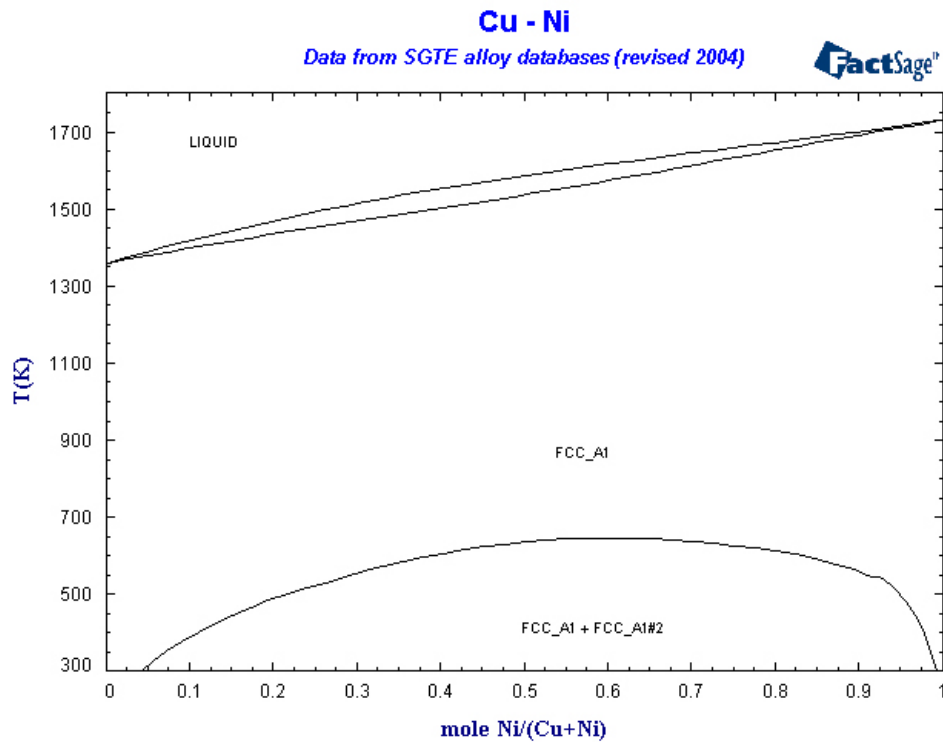


Figure 4.1:  $Cu - Ni$  phase diagram (*source: www.factsage.com*)

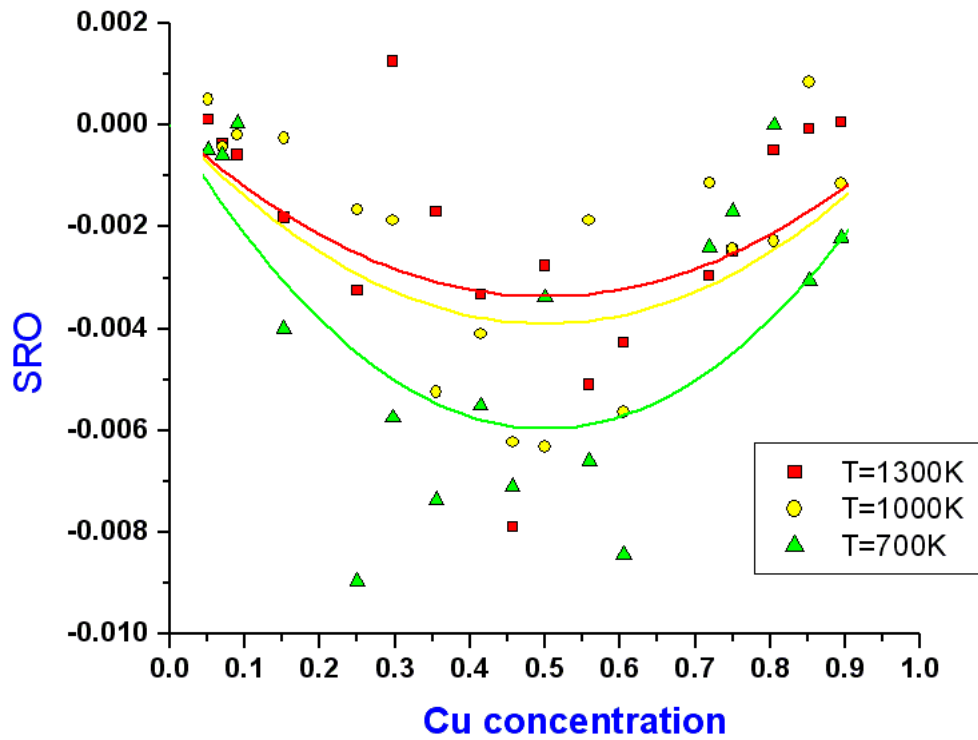


Figure 4.2: SRO vs.  $Cu$  concentration for  $T = 700, 1000$  and  $1300$  K. The fitted quadratics with the boundary condition SRO vanish at 0% and 100%  $Cu$  concentrations are also shown.



In Fig. 4.2, SRO vs.  $Cu$  concentration is plotted for select temperatures ( $T = 700, 1000$  and  $1300$  K). SRO is defined as the probability of finding  $Cu$  at the vicinity of  $Ni$  relative to the probability expected for an ideal solid solution at the same concentration. The sign of the SRO indicates a tendency to cluster, as is appropriate for this alloy. The degree of SRO is small but increases some with lower temperature, as expected. The fitted curves are quadratics and chosen to be vanished at  $Cu$  concentrations  $x = 0$  and  $x = 1$ .

The statistical variability for the following figures is typical for the kinetic Monte Carlo runs. The lines plotted in the those figures correspond to the global fit for all compositors and temperatures in  $Cu - Ni$ . The complete set of calculated tracer diffusivities for  $Cu$  in  $Cu - Ni$  were fitted to the simple form, Eq. 3.11, where

$$E_m(x) = xP_1 + (1 - x)P_2. \quad (4.1)$$

The parameter  $P_1$  is set to  $0.72$  eV to match the vacancy migration in pure  $Cu$  [FBD86]. So only two parameters were used for the global fit to seven temperatures and 20 compositions. Similarly, the complete set of calculated tracer diffusivities for  $Ni$  in  $Cu - Ni$  were fitted to the same form, Eq. 3.11, but this time  $P_2$  is set to  $1.08$  eV to match the result for pure  $Ni$  [FBD86]. The resulting parameters are presented in Table. 4.1.

These calculations are of the tracer diffusivity at fixed vacancy concentration. To make a direct comparison to experiment, the vacancy concentration as a function of composition and temperature must be calculated and then these results are scaled accordingly. Also there is a overall kinetic Monte Carlo time scale factor,  $\tau$ , which must be determined. However, the ratio of the two tracer diffusivities is a prediction

Type	$d_0$ (arb)	$P_1$ (eV)	$P_2$ (eV)
<i>Cu</i>	$1.13(\pm 0.08) \times 10^{-2}$	0.72	$0.87 \pm 0.01$
<i>Ni</i>	$1.24(\pm 0.01) \times 10^{-1}$	$0.90 \pm 0.01$	1.08

Table 4.1: Parameters obtained by a global fit to all of the presented kMC results for scaled tracer diffusivity in *Cu* – *Ni*

independent of  $\tau$  and the vacancy concentration. From the fit, the predicted ratio

$$\frac{D_{Cu}}{D_{Ni}} = \frac{d_{Cu}}{d_{Ni}} = 0.091 \exp\left(+\frac{(0.21 - 0.03x) \text{ eV}}{k_B T}\right) \quad (4.2)$$

which means that in the range 900-1000 K (depending on the composition) the diffusivities will be about the same. At higher temperatures,  $D_{Cu} < D_{Ni}$  and at lower temperatures,  $D_{Cu} > D_{Ni}$ .

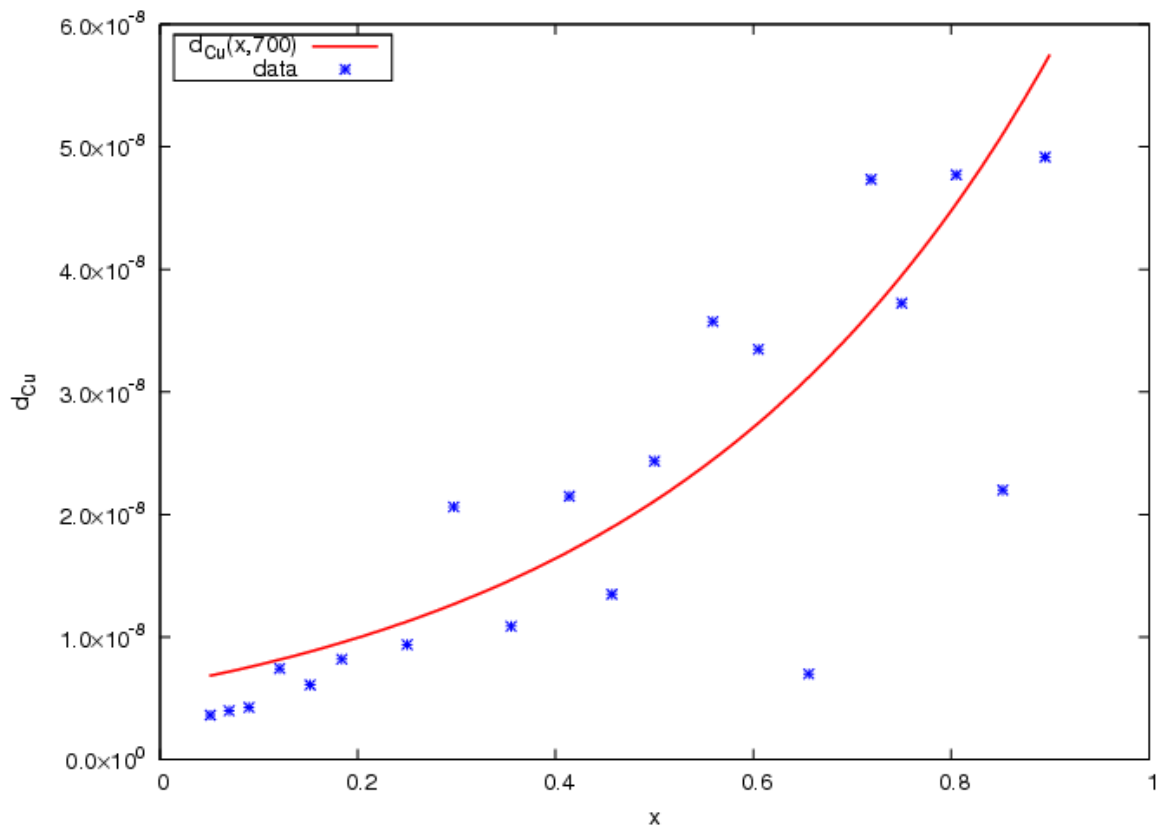


Figure 4.3:  $d_{Cu}$  vs.  $Cu$  concentration at 700 K for  $Cu - Ni$ . The curve is the global fit to all compositions and temperatures, and the symbol “\*” shows the result of kMC runs.

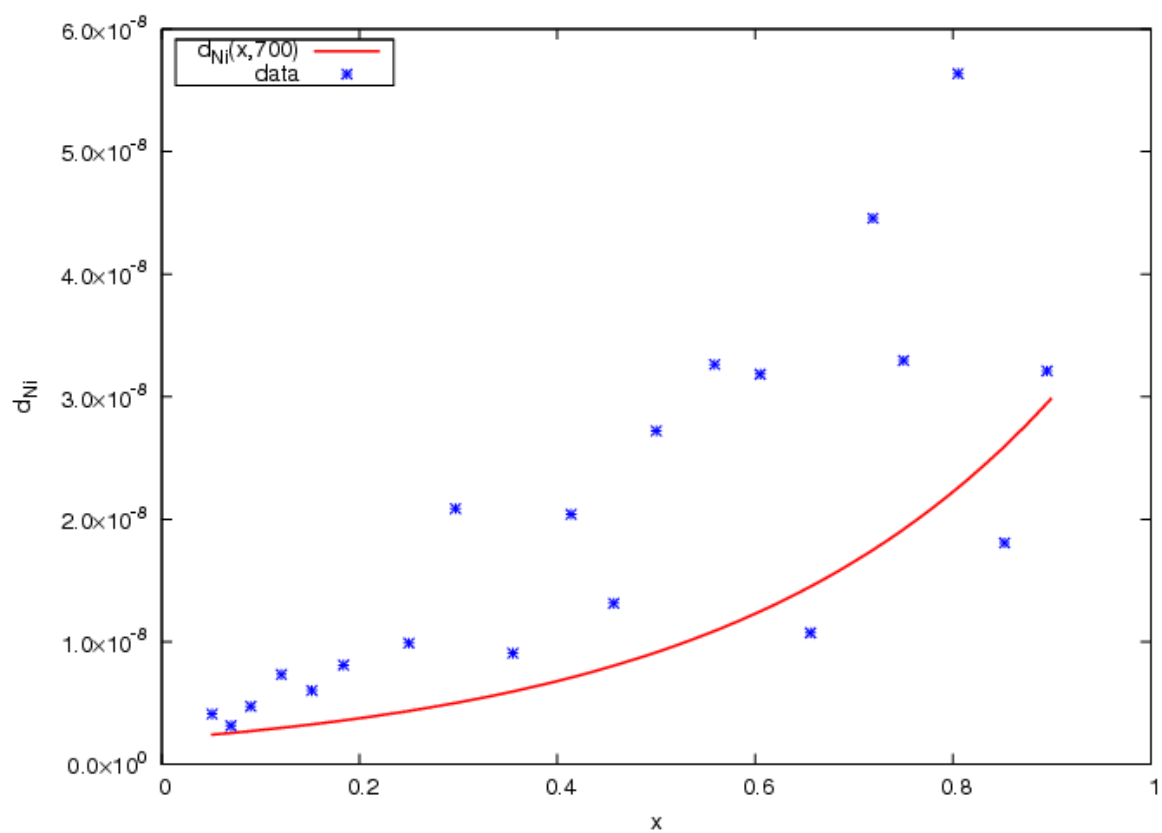


Figure 4.4:  $d_{Ni}$  vs.  $Cu$  concentration at 700 K for  $Cu - Ni$ . The curve is the global fit to all compositions and temperatures, and the symbol “\*” shows the result of kMC runs.

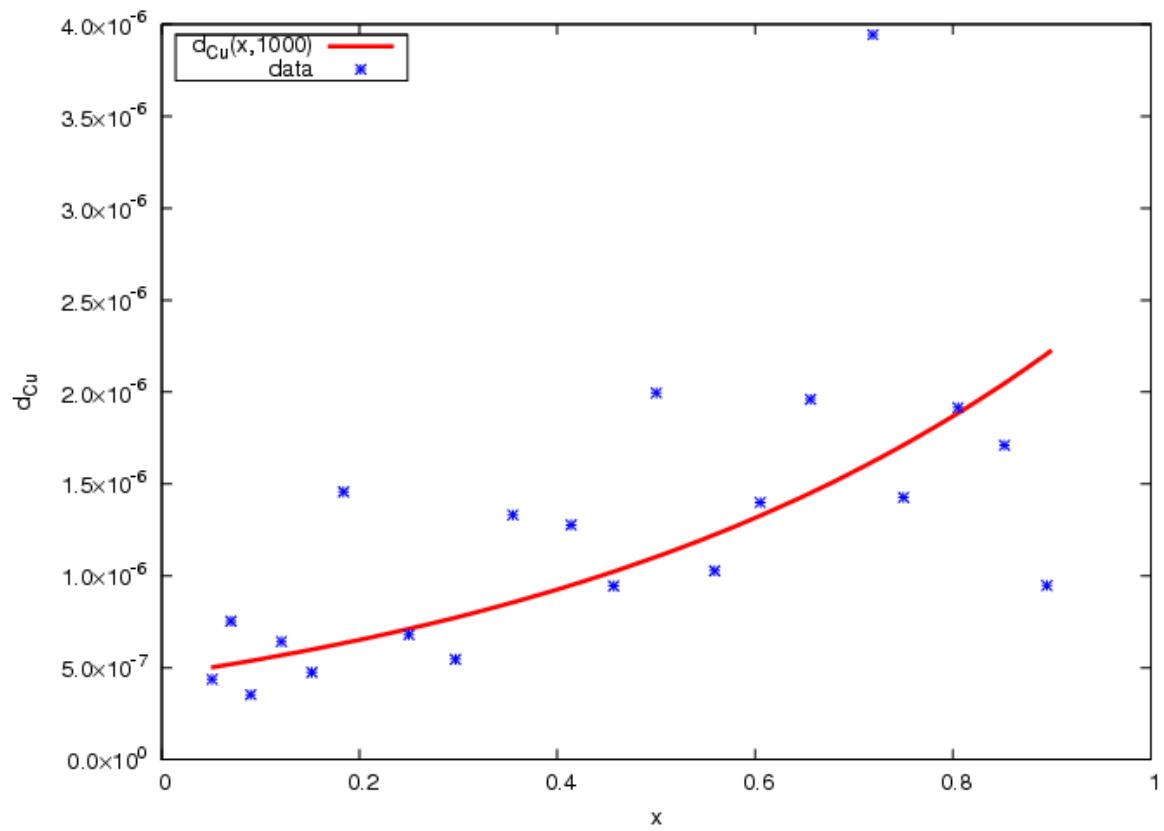


Figure 4.5:  $d_{Cu}$  vs.  $Cu$  concentration at 1000 K for  $Cu - Ni$ . The curve is the global fit to all compositions and temperatures, and the symbol “\*” shows the result of kMC runs.

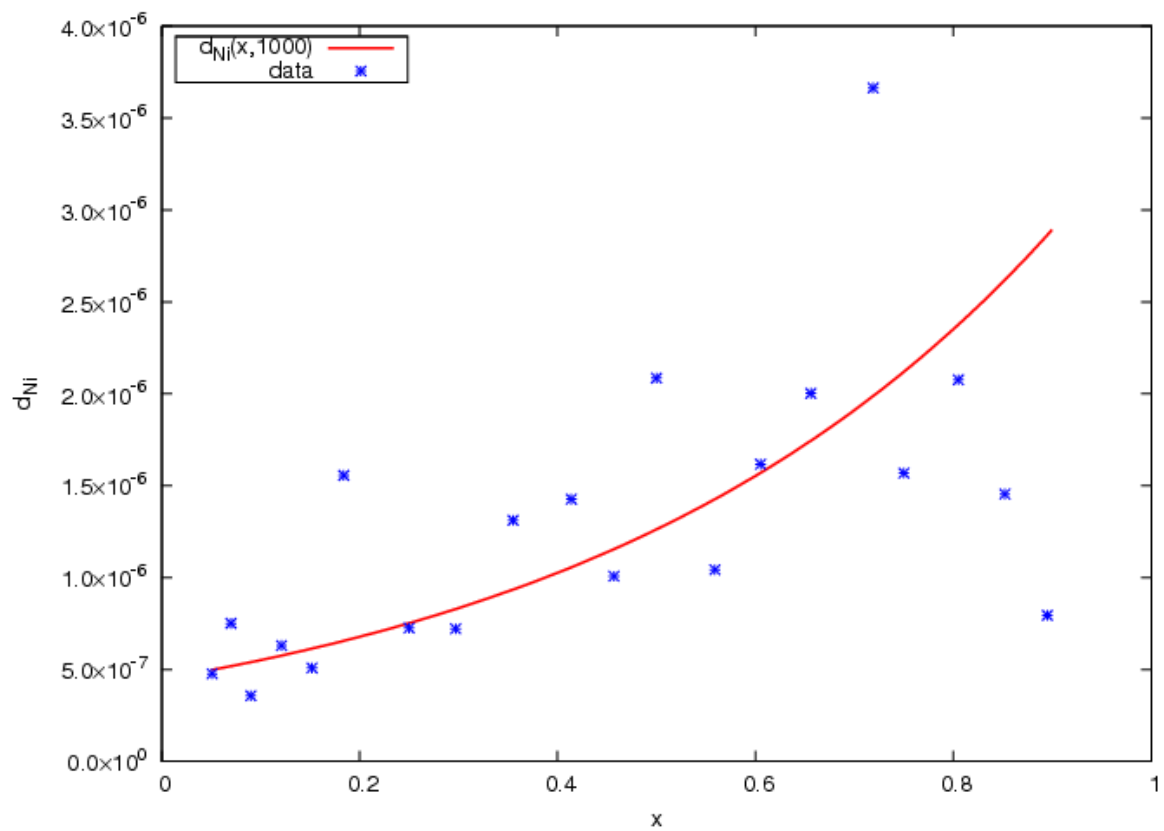


Figure 4.6:  $d_{Ni}$  vs.  $Cu$  concentration at 1000 K for  $Cu - Ni$ . The curve is the global fit to all compositions and temperatures, and the symbol “\*” shows the result of kMC runs.

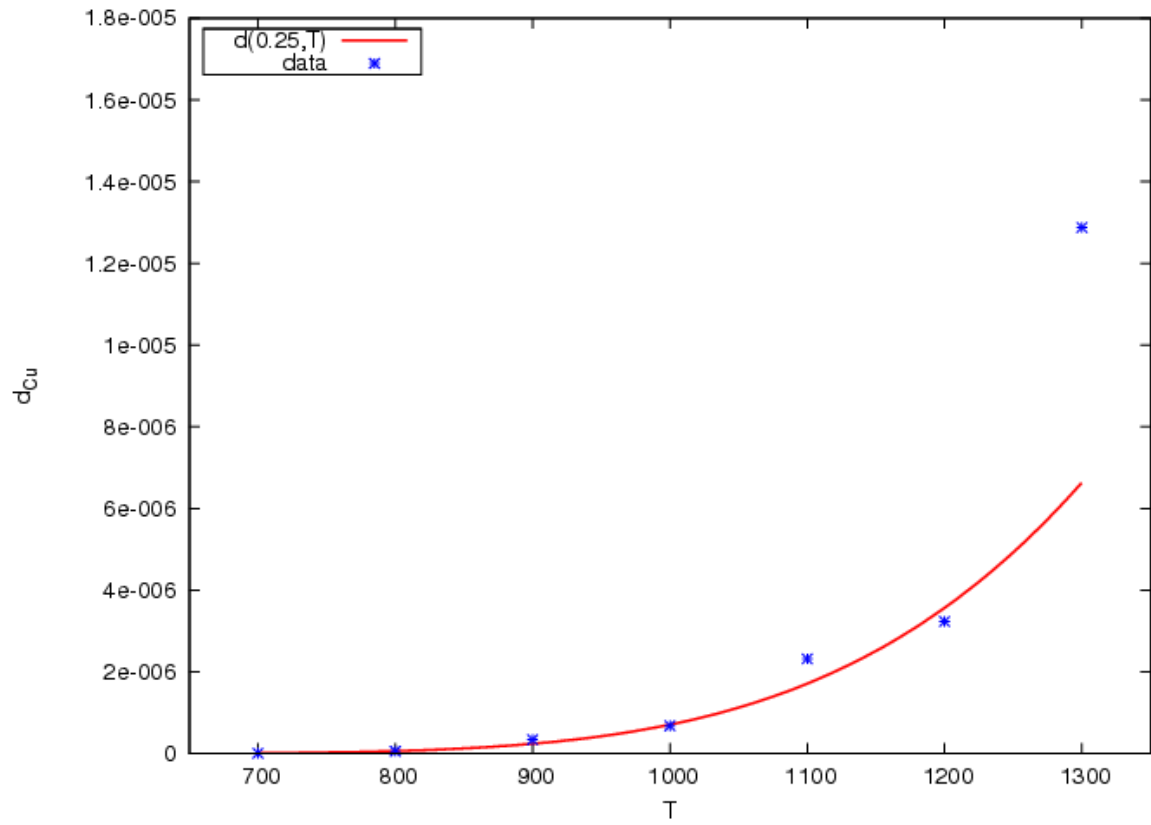


Figure 4.7:  $d_{Cu}$  vs. Temperature (K) at a fixed  $Cu$  concentration,  $x = 0.25$  for  $Cu - Ni$ . The curve is the global fit to all compositions and temperatures, and the symbol “\*” shows the result of kMC runs.

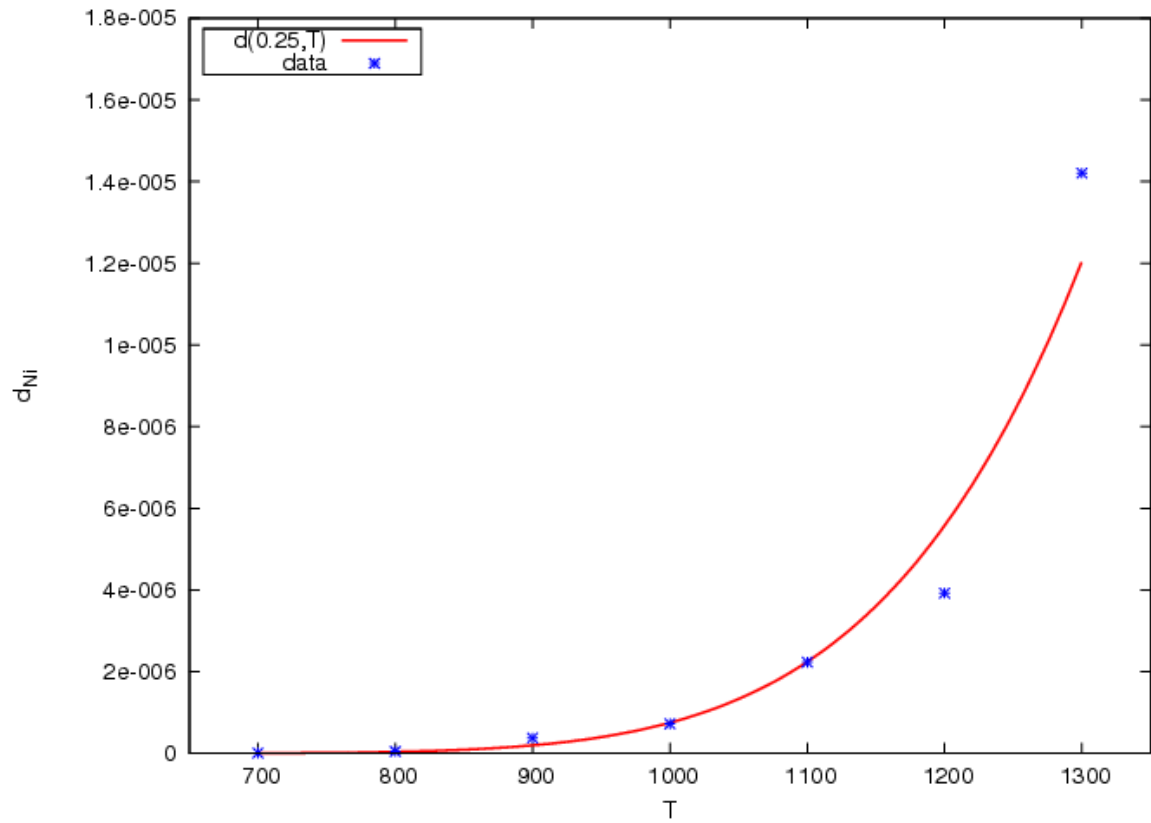


Figure 4.8:  $d_{Ni}$  vs. Temperature (K) at a fixed  $Cu$  concentration,  $x = 0.25$  for  $Cu - Ni$ . The curve is the global fit to all compositions and temperatures, and the symbol “\*” shows the result of kMC runs.



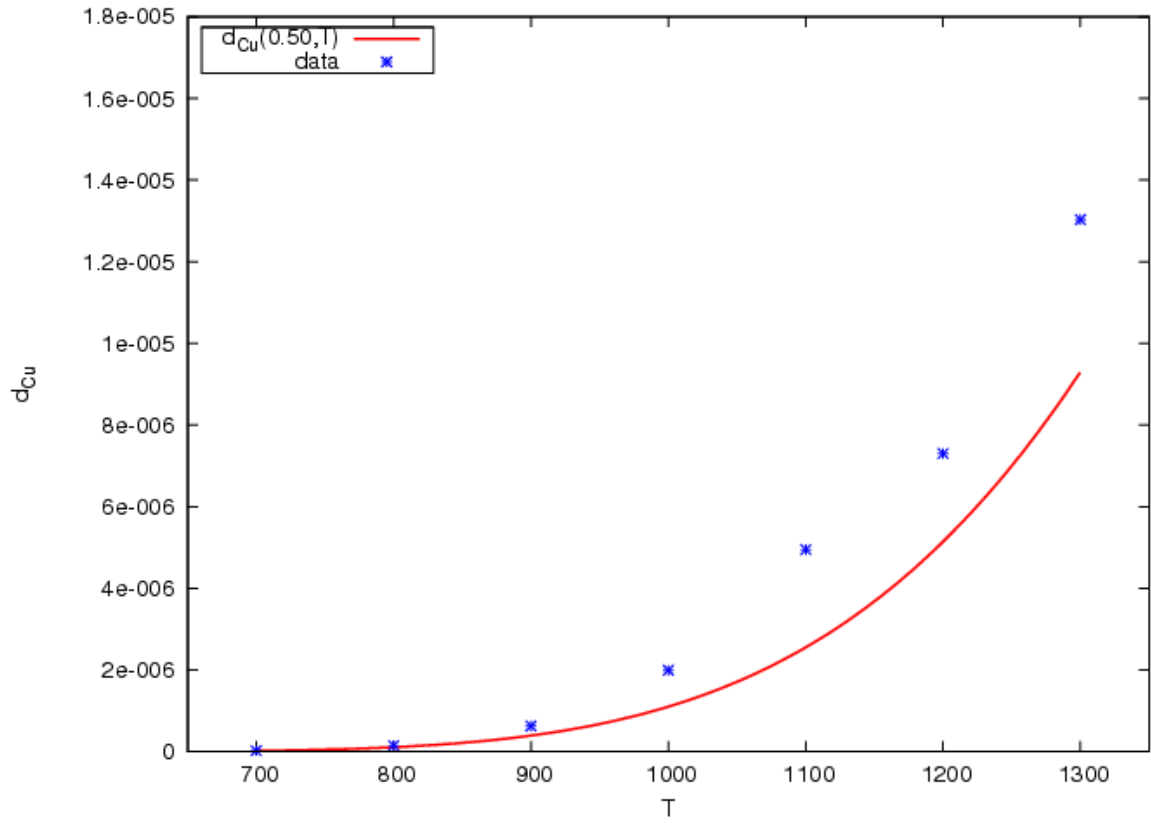


Figure 4.9:  $d_{Cu}$  vs. Temperature (K) at a fixed  $Cu$  concentration,  $x = 0.50$  for  $Cu - Ni$ . The curve is the global fit to all compositions and temperatures, and the symbol “\*” shows the result of kMC runs.

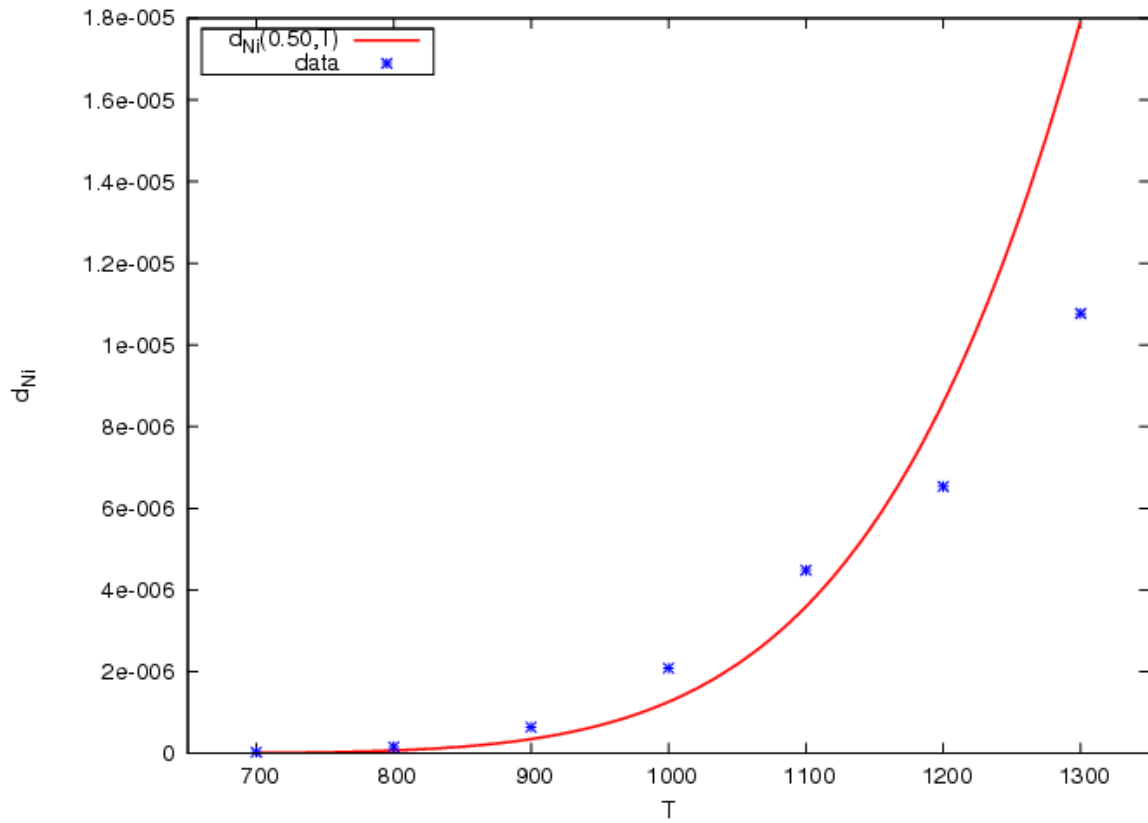


Figure 4.10:  $d_{Ni}$  vs. Temperature (K) at a fixed  $Cu$  concentration,  $x = 0.50$  for  $Cu - Ni$ . The curve is the global fit to all compositions and temperatures, and the symbol “\*” shows the result of kMC runs.

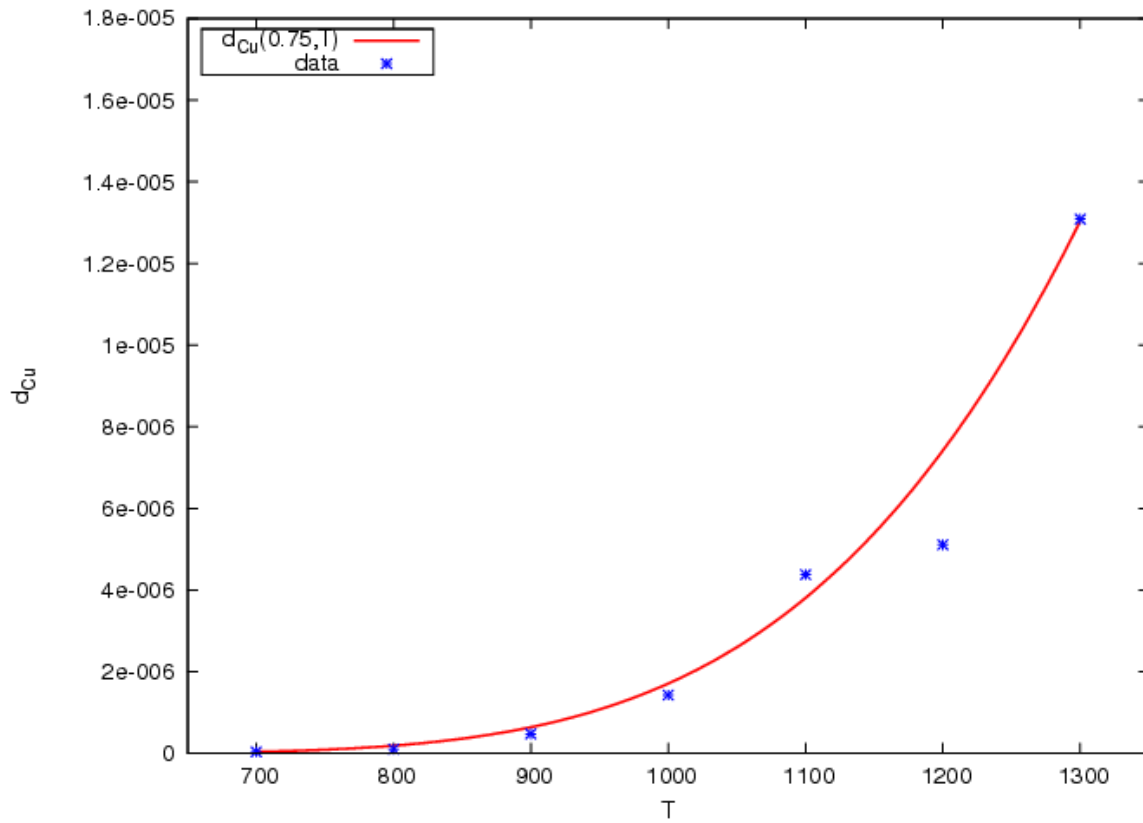


Figure 4.11:  $d_{Cu}$  vs. Temperature (K) at a fixed  $Cu$  concentration,  $x = 0.75$  for  $Cu - Ni$ . The curve is the global fit to all compositions and temperatures, and the symbol “\*” shows the result of kMC runs.

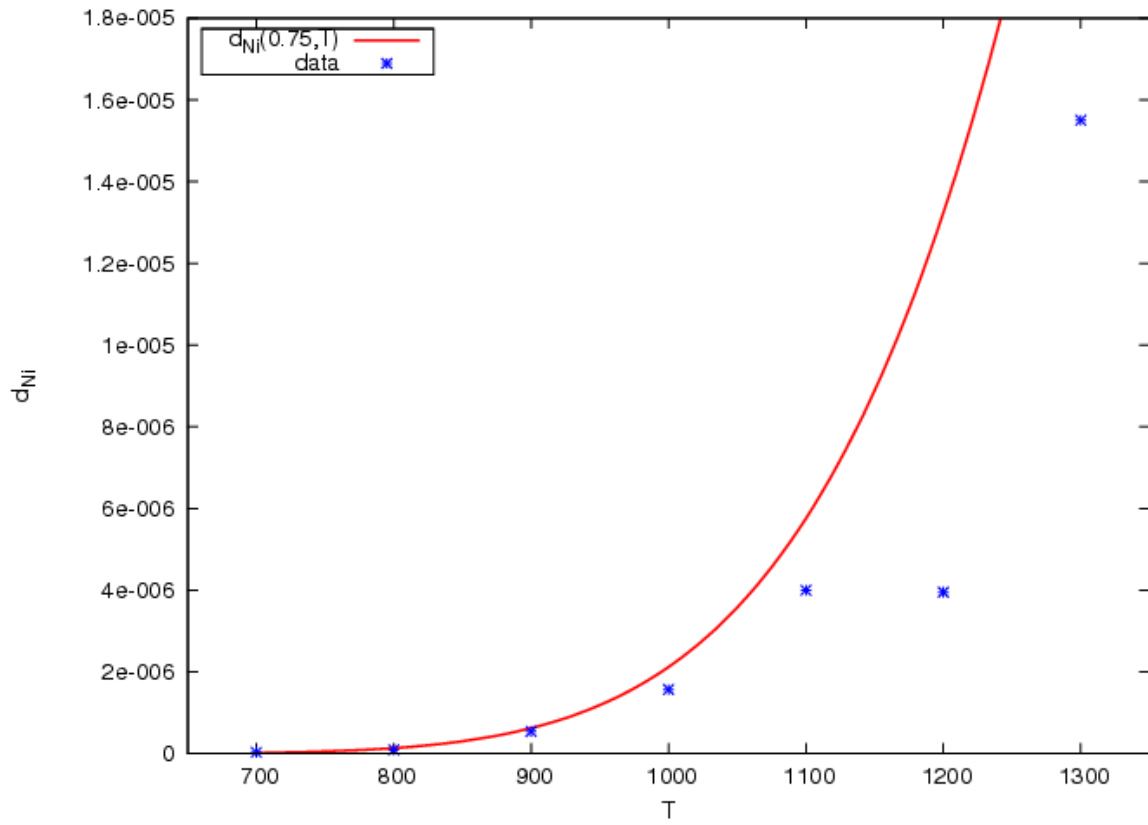


Figure 4.12:  $d_{Ni}$  vs. Temperature at a fixed  $Cu$  concentration,  $x = 0.75$  for  $Cu - Ni$ . The curve is the global fit to all compositions and temperatures, and the symbol “\*” shows the result of kMC runs.

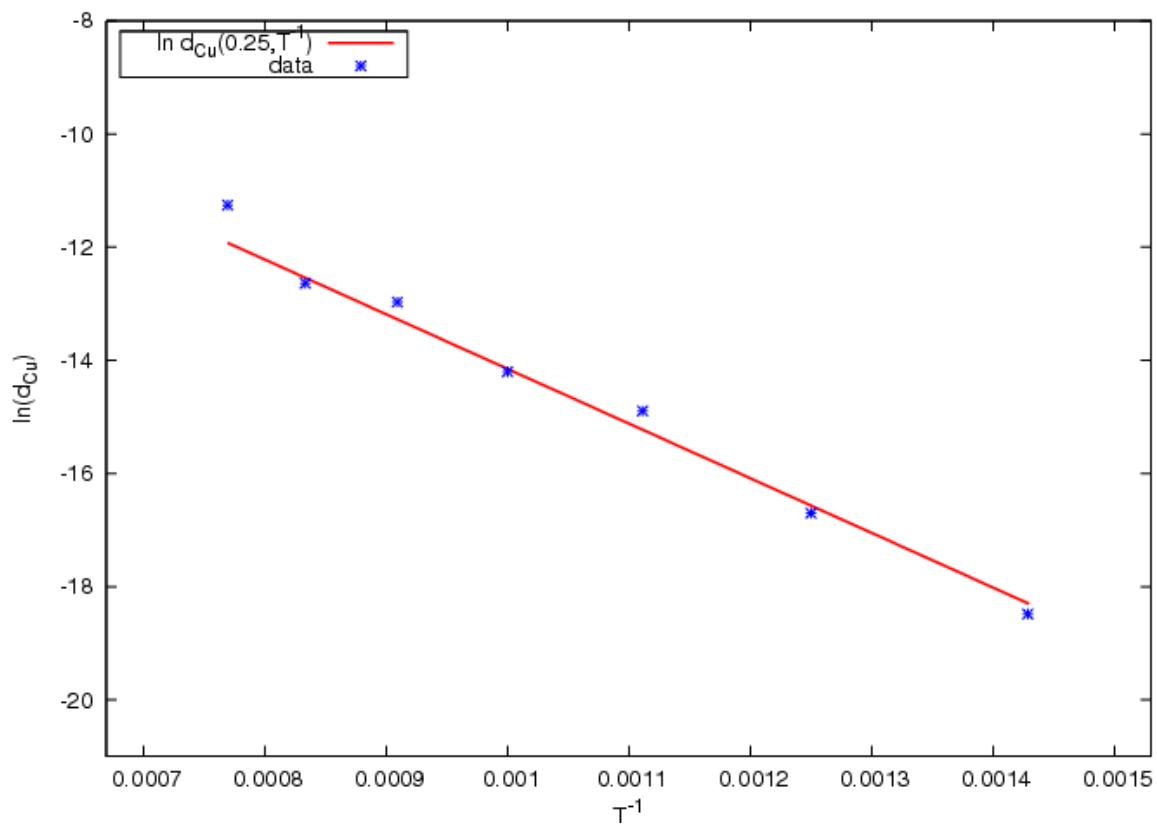


Figure 4.13: Results of kMC simulations of  $d_{Cu}$  plotted in Arrhenius form at 25%  $Cu$  concentration for the temperature range 700 – 1300 K.

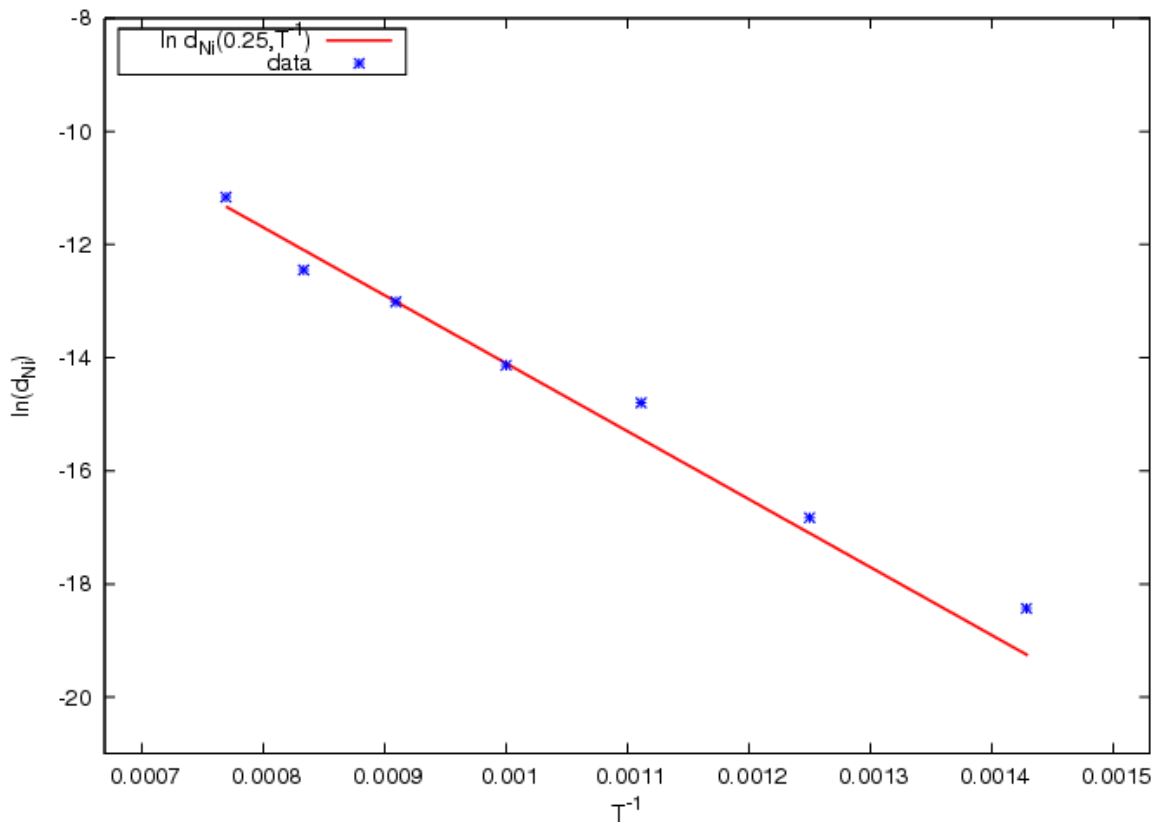


Figure 4.14: Results of kMC simulations of  $d_{Ni}$  plotted in Arrhenius form at 25% *Cu* concentration for the temperature range 700 – 1300 K.

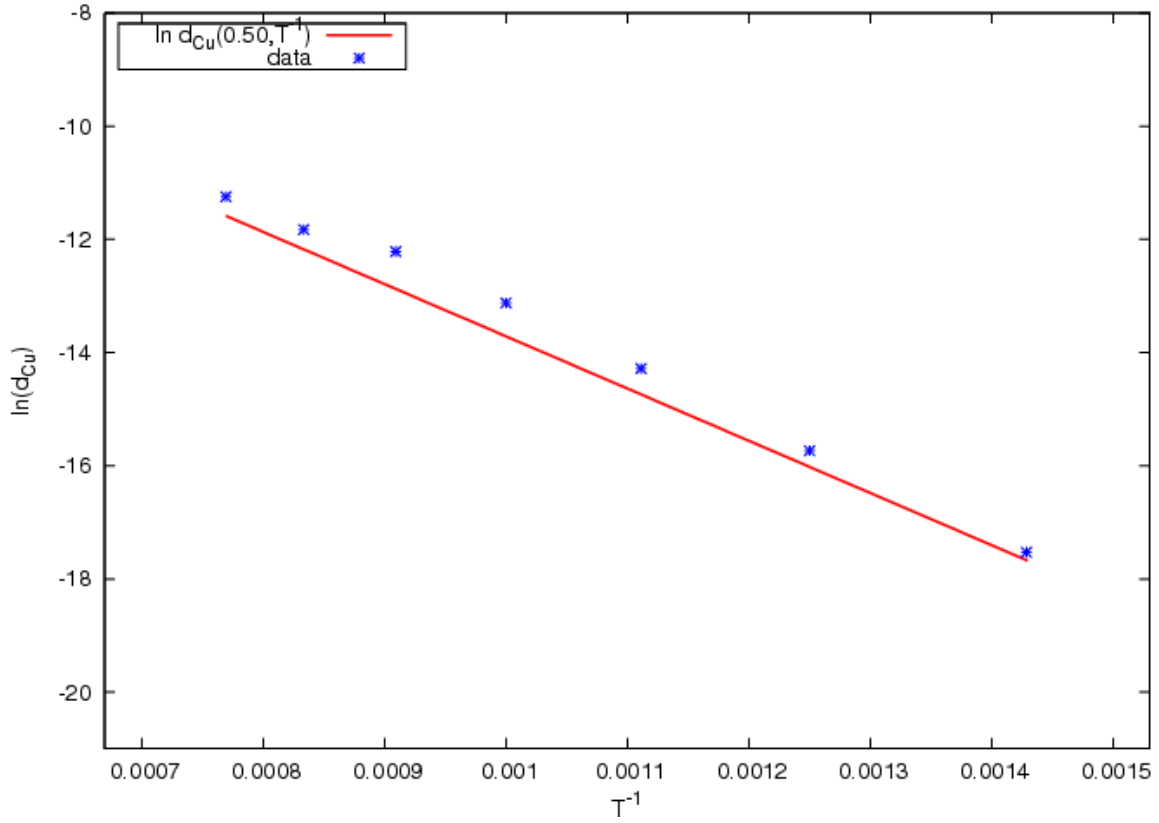


Figure 4.15: Results of kMC simulations of  $d_{Cu}$  plotted in Arrhenius form at 50%  $Cu$  concentration for the temperature range 700 – 1300 K.

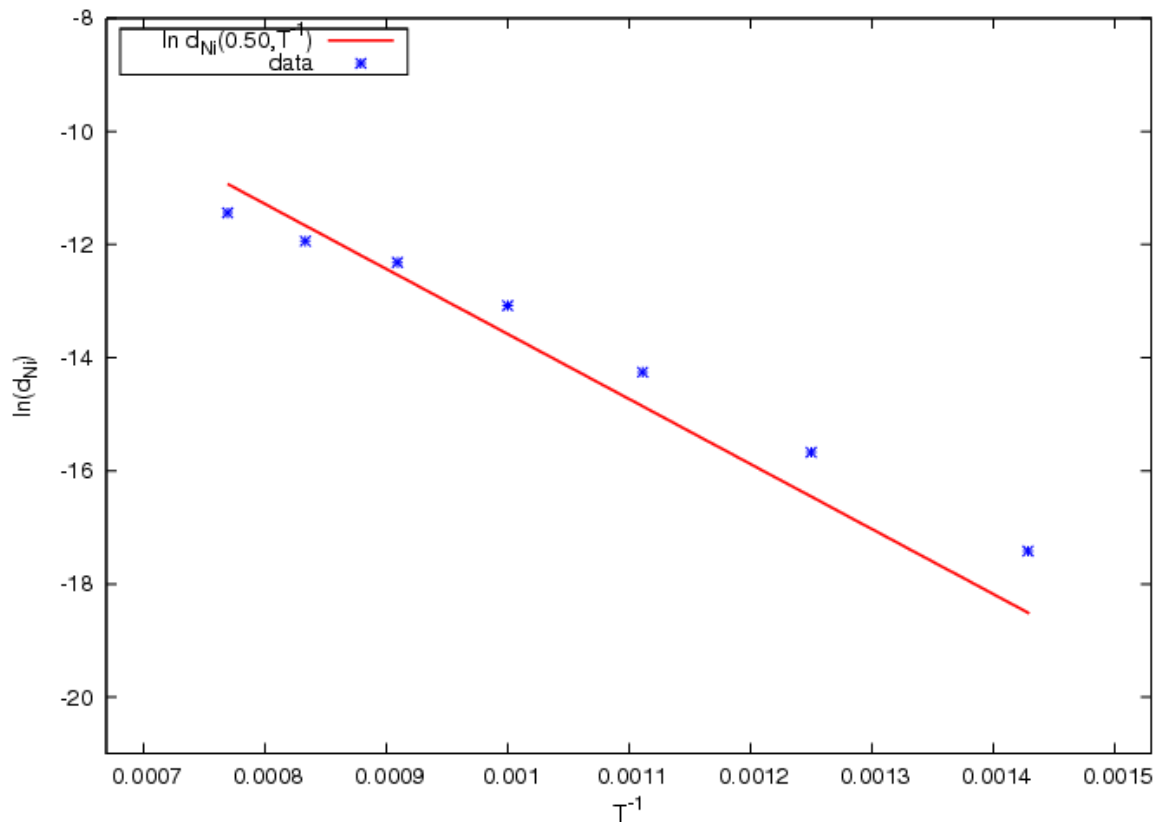


Figure 4.16: Results of kMC simulations of  $d_{Ni}$  plotted in Arrhenius form at 50% *Cu* concentration for the temperature range 700 – 1300 K.



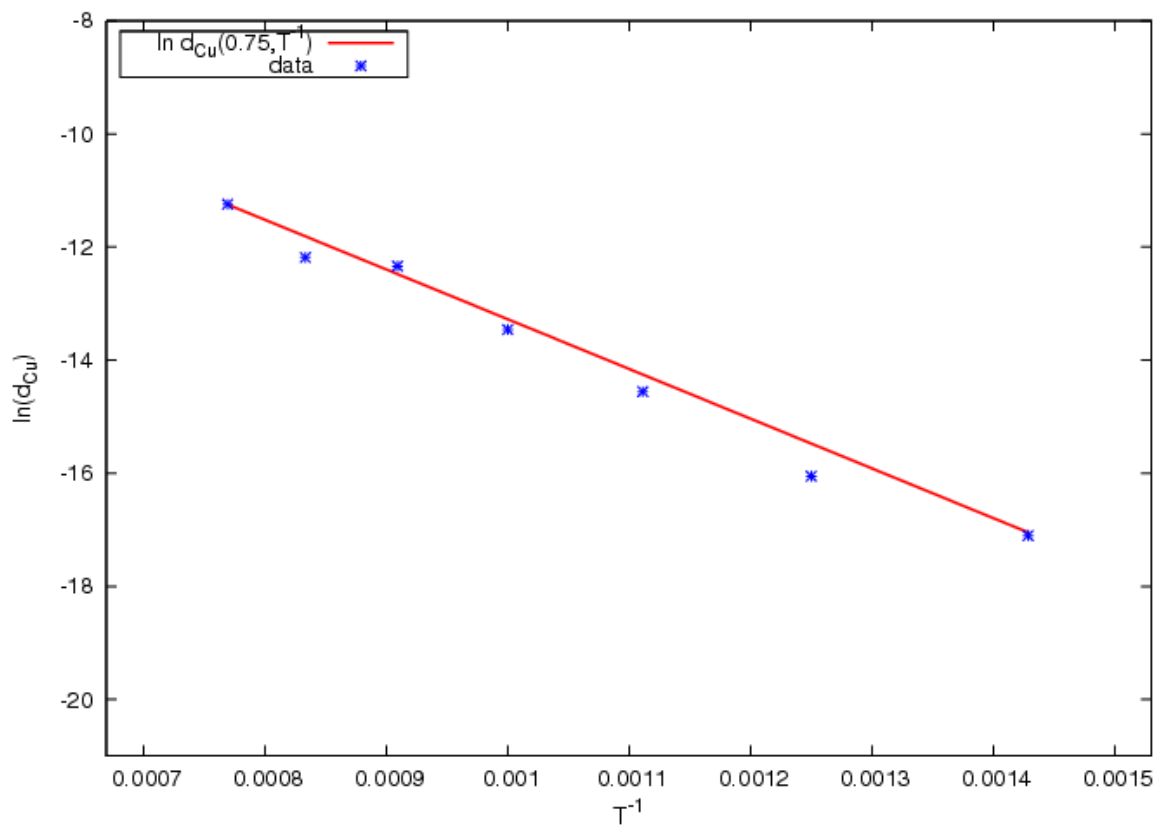


Figure 4.17: Results of kMC simulations of  $d_{Cu}$  plotted in Arrhenius form at 75%  $Cu$  concentration for the temperature range 700 – 1300 K.

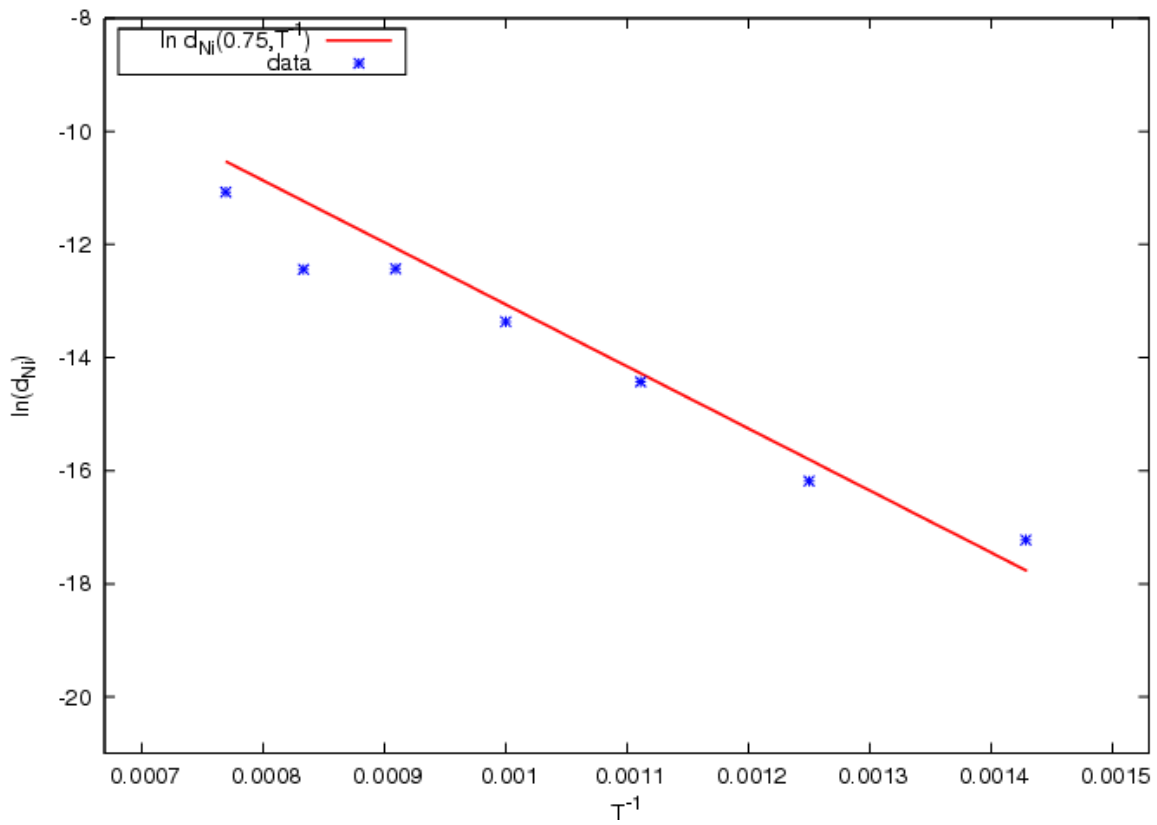


Figure 4.18: Results of kMC simulations of  $d_{Ni}$  plotted in Arrhenius form at 75%  $Cu$  concentration for the temperature range 700 – 1300 K.

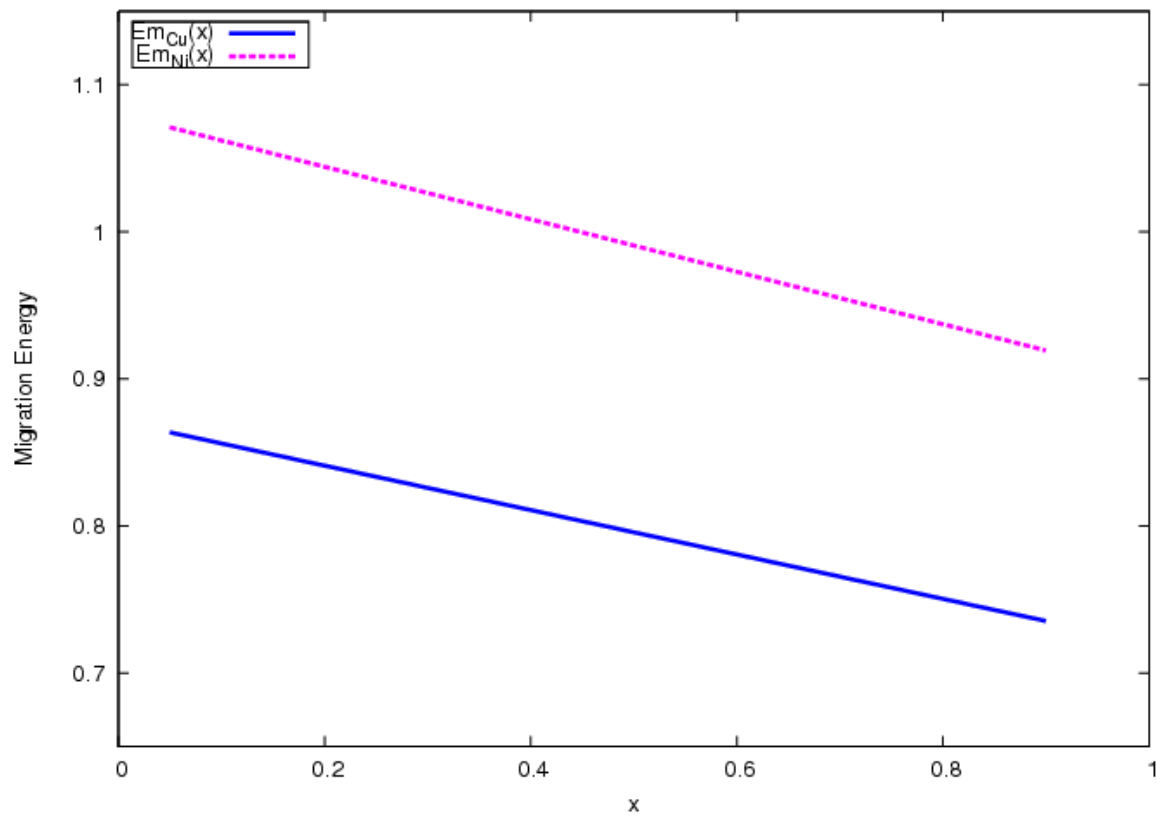


Figure 4.19: Migration energy of both  $Cu$  and  $Ni$  for  $Cu - Ni$  as a function of  $Cu$  concentration, which is obtained by the global fitting of kMC results to Eq. 3.11 for all temperatures and compositions.

## 4.2 Bulk Tracer Diffusivity for $Au - Ag$

The same approach described in the previous section is used to examine the case of a weakly ordering alloy,  $Au - Ag$ . Nine compositions are chosen from the range 10 – 90% and temperatures from the range of 800 – 1300 K. The temperatures are well above the ordering temperature (see Fig. 4.20), either the experimental or our calculated values. Equilibrium Monte Carlo calculations show negligible long-range order (LRO), and some weak short-range ordering (SRO) which depended on composition and temperature.

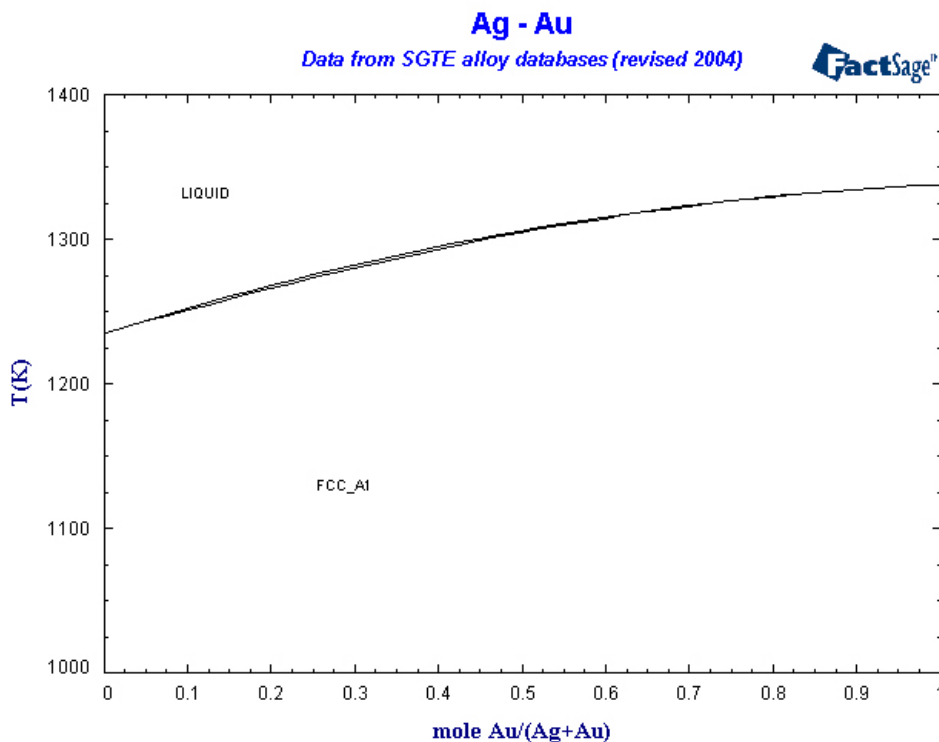


Figure 4.20:  $Ag - Au$  phase diagram (*source: www.factsage.com*)

In Fig. 4.21, SRO vs.  $Ag$  concentration is plotted for select temperatures ( $T = 600, 800$  and  $1000$  K). SRO is defined as the probability of finding  $Au$  at

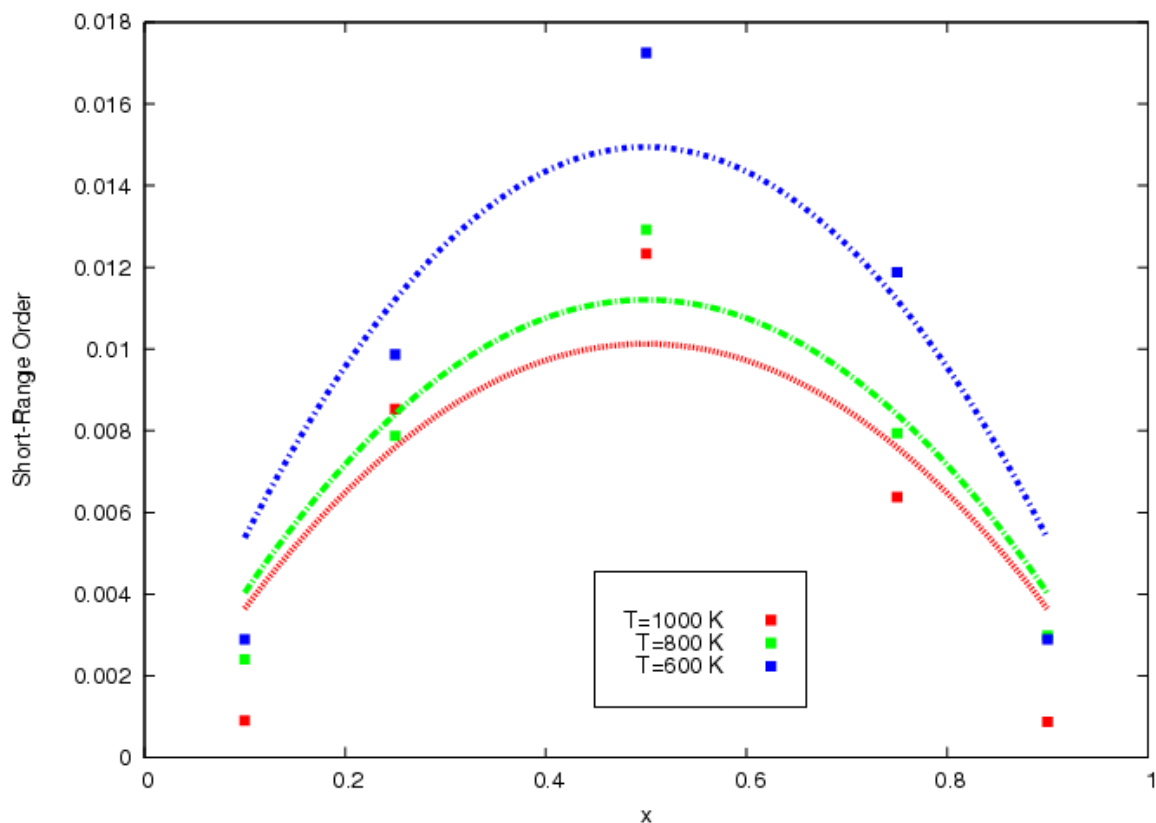


Figure 4.21: SRO vs.  $Ag$  concentration for  $T = 600, 800$  and  $1000$  K. The fitted quadratics with the boundary condition SRO vanish at 0% and 100%  $Ag$  concentrations are also shown.

the vicinity of  $Ag$  relative to the probability expected for an ideal solid solution at the same concentration. The sign of the SRO indicates a tendency to order, as is appropriate for this alloy. The degree of SRO is small but increases some with lower temperature, as expected. The fitted curves are quadratics provided that they vanish at  $Ag$  concentrations  $x = 0$  and  $x = 1$ .

The statistical variability for the following figures is typical for the kinetic Monte Carlo runs. The lines plotted in the those figures correspond to the global fit for all compositors and temperatures in  $Au - Ag$ . The complete set of calculated tracer diffusivities for  $Au$  in  $Au - Ag$  was fitted to the simple form, Eq. 3.11 where

Type	$d_0$ (arb)	$P_1$ (eV)	$P_2$ (eV)
<i>Au</i>	$3.23(\pm 0.00) \times 10^{-2}$	0.71	$0.80 \pm 0.01$
<i>Ag</i>	$4.54(\pm 0.00) \times 10^{-2}$	$0.74 \pm 0.01$	0.83

Table 4.2: Parameters obtained by a global fit to all of the presented kMC results for scaled tracer diffusivity in *Au* – *Ag*

$E_m$  is given by Eq. 4.1.

The parameter  $P_1$  is set to 0.71 eV to match the vacancy migration in pure *Au* [FBD86]. So only two parameters were used for the global fit to six temperatures and nine compositions. Similarly, the complete set of calculated tracer diffusivities for *Ag* in *Au* – *Ag* was fitted to the same form, Eq. 3.11, but this time  $P_2$  is set to 0.83 eV to match the result for pure *Ag* [FBD86]. The resulting parameters are presented in Table. 4.2.

These calculations are of the tracer diffusivity at fixed vacancy concentration. To make a direct comparison to experiment, the vacancy concentration as a function of composition and temperature must be calculated and then these results are scaled accordingly. Also there is a overall kinetic Monte Carlo time scale factor,  $\tau$ , which must be determined. However, the ratio of the two tracer diffusivities is a prediction independent of  $\tau$  and the vacancy concentration. From the fit, the predicted ratio

$$\frac{D_{Au}}{D_{Ag}} = \frac{d_{Au}}{d_{Ag}} = 0.711 \exp\left(+\frac{0.03 \text{ eV}}{k_B T}\right) \quad (4.3)$$

which means that in the range of temperatures considered here (800 – 1300 K)  $D_{Au} \approx D_{Ag}$ .

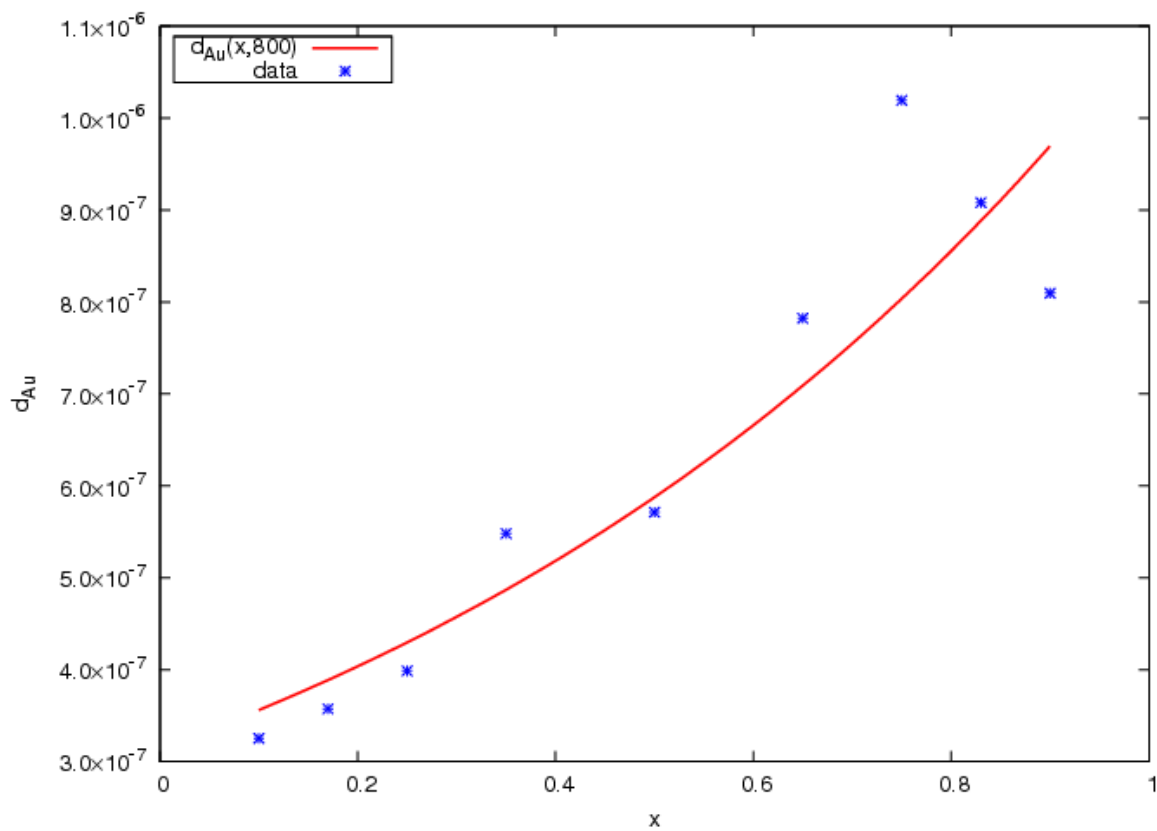


Figure 4.22:  $d_{Au}$  vs.  $Ag$  concentration at 800 K for  $Au - Ag$ . The curve is the global fit to all compositions and temperatures, and the symbol “\*” shows the result of kMC runs.

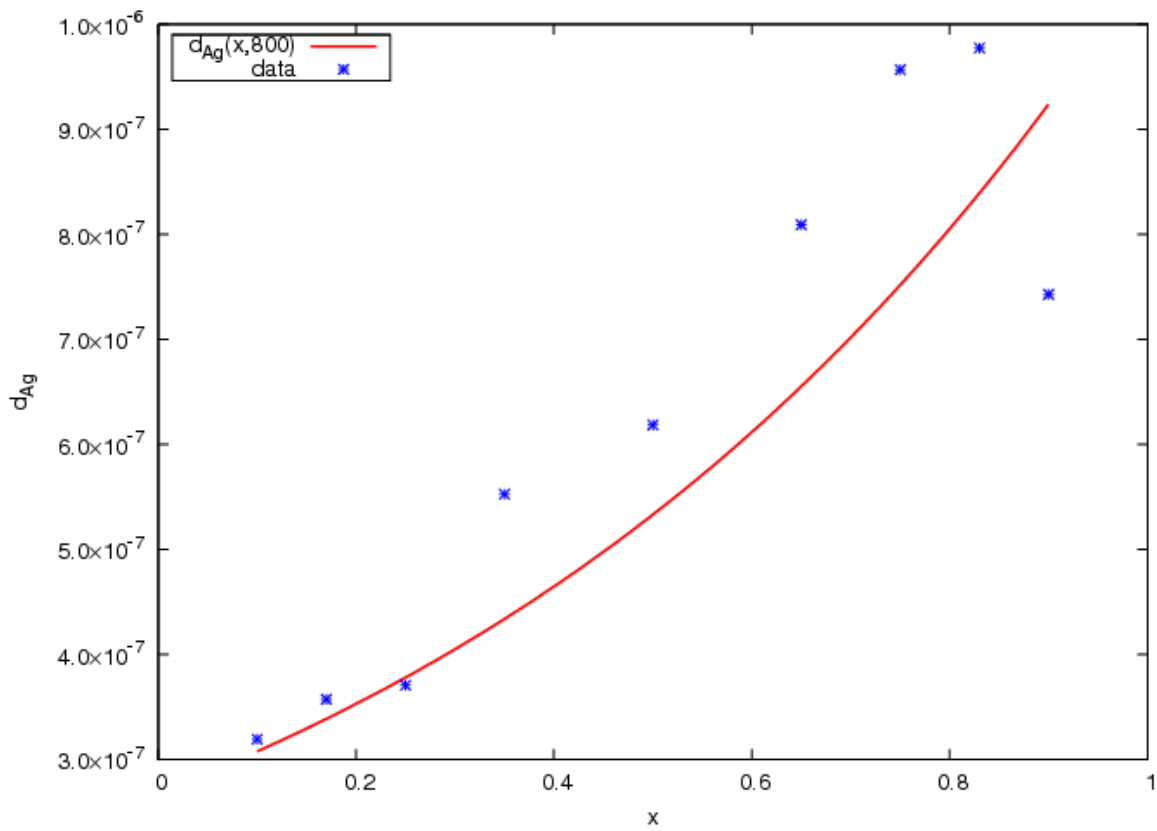


Figure 4.23:  $d_{Ag}$  vs.  $Ag$  concentration at 800 K for  $Au - Ag$ . The curve is the global fit to all compositions and temperatures, and the symbol “\*” shows the result of kMC runs.



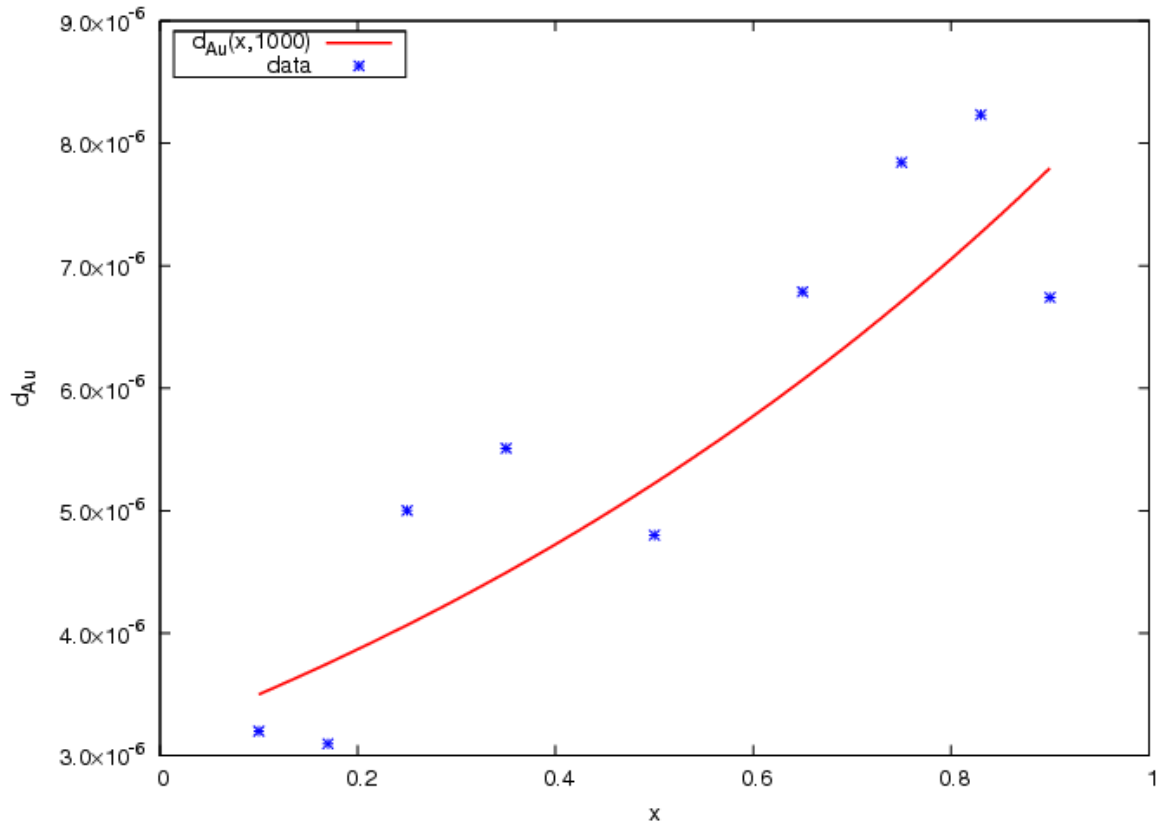


Figure 4.24:  $d_{Au}$  vs.  $Ag$  concentration at 1000 K for  $Au - Ag$ . The curve is the global fit to all compositions and temperatures, and the symbol “\*” shows the result of kMC runs.

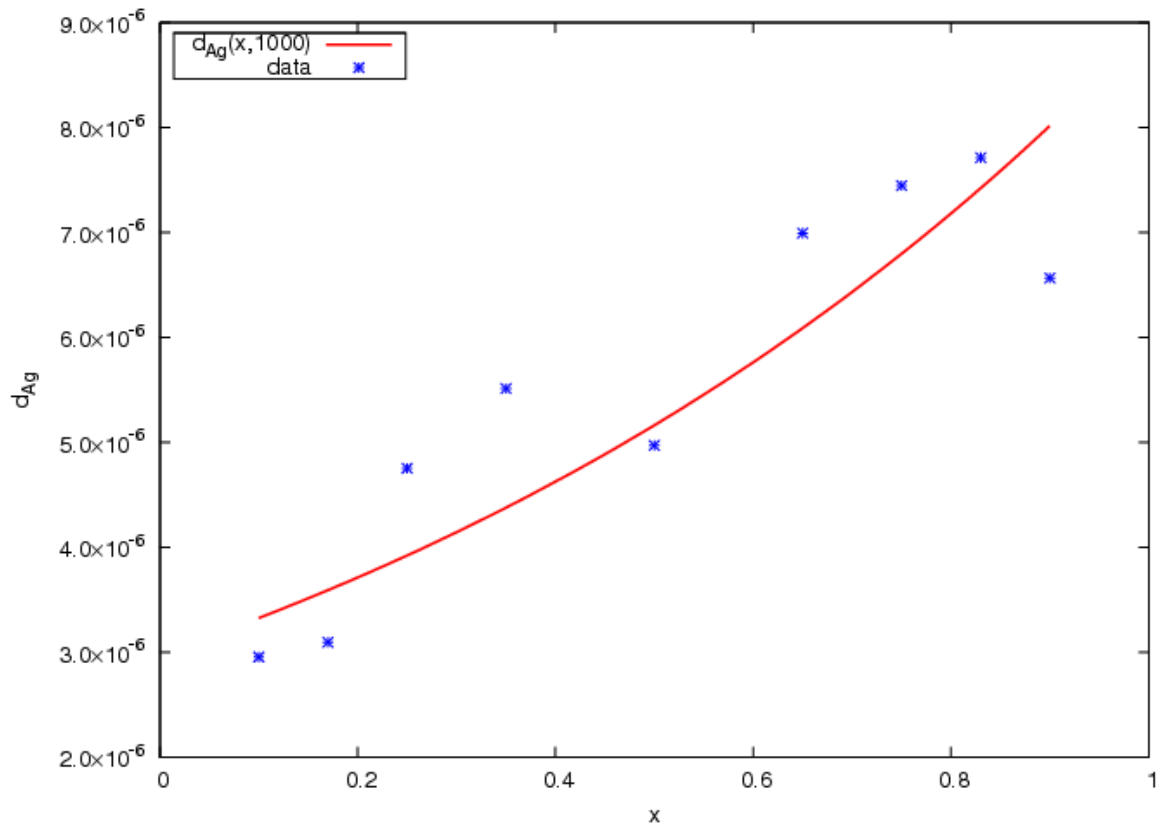


Figure 4.25:  $d_{Ag}$  vs.  $Ag$  concentration at 1000 K for  $Au - Ag$ . The curve is the global fit to all compositions and temperatures, and the symbol “\*” shows the result of kMC runs.

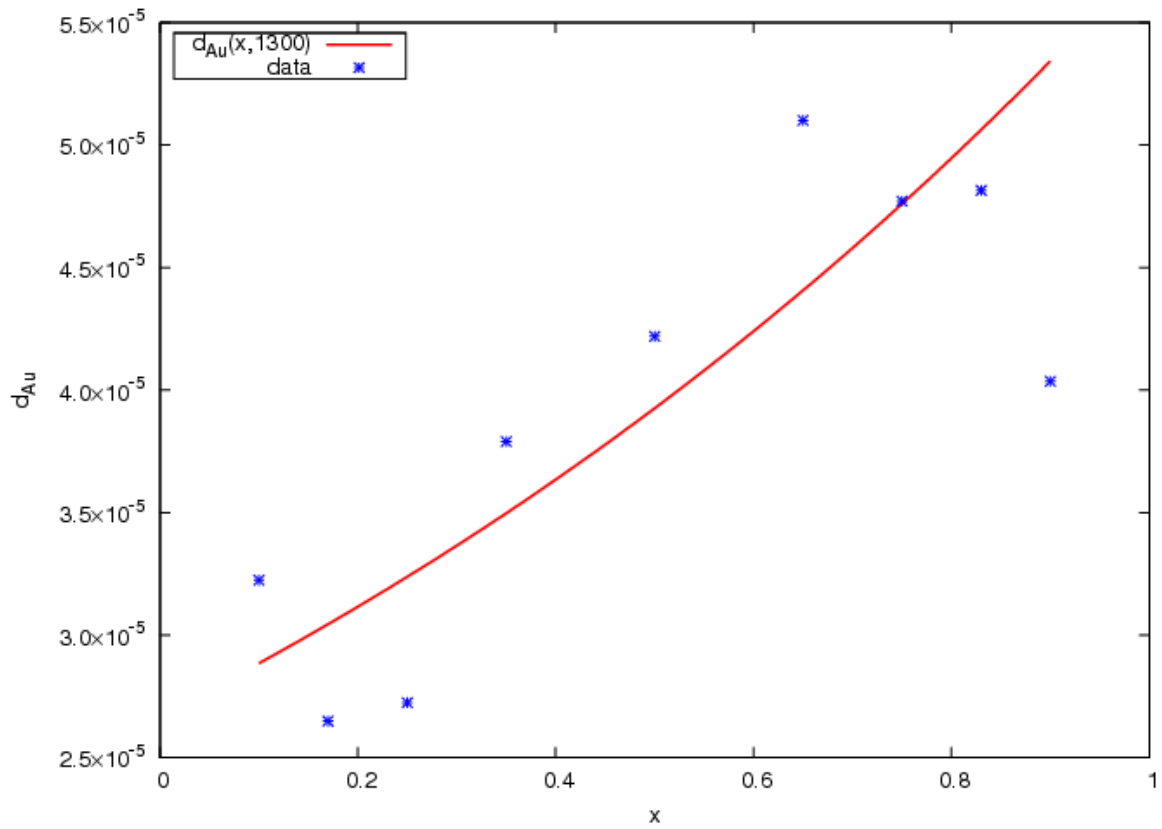


Figure 4.26:  $d_{Au}$  vs.  $Ag$  concentration at 1300 K for  $Au - Ag$ . The curve is the global fit to all compositions and temperatures, and the symbol “\*” shows the result of kMC runs.

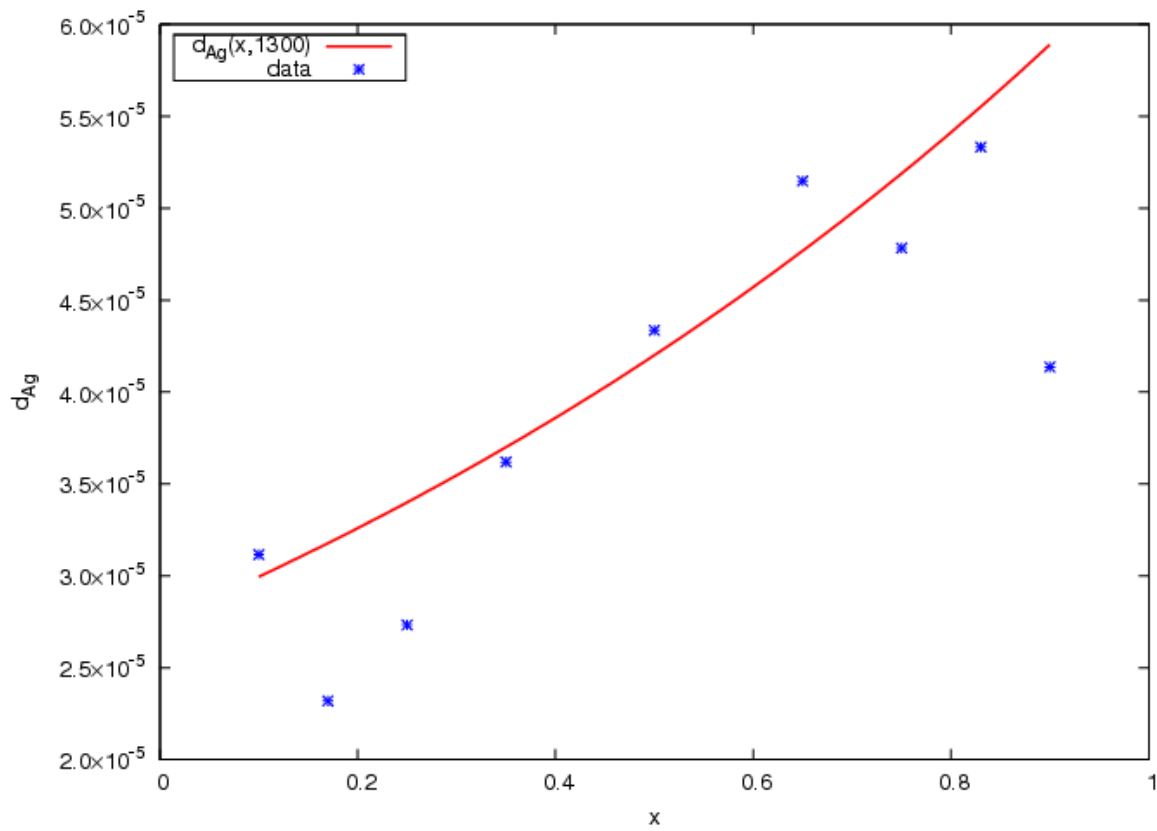


Figure 4.27:  $d_{Ag}$  vs.  $Ag$  concentration at 1300 K for  $Au - Ag$ . The curve is the global fit to all compositions and temperatures, and the symbol “\*” shows the result of kMC runs.

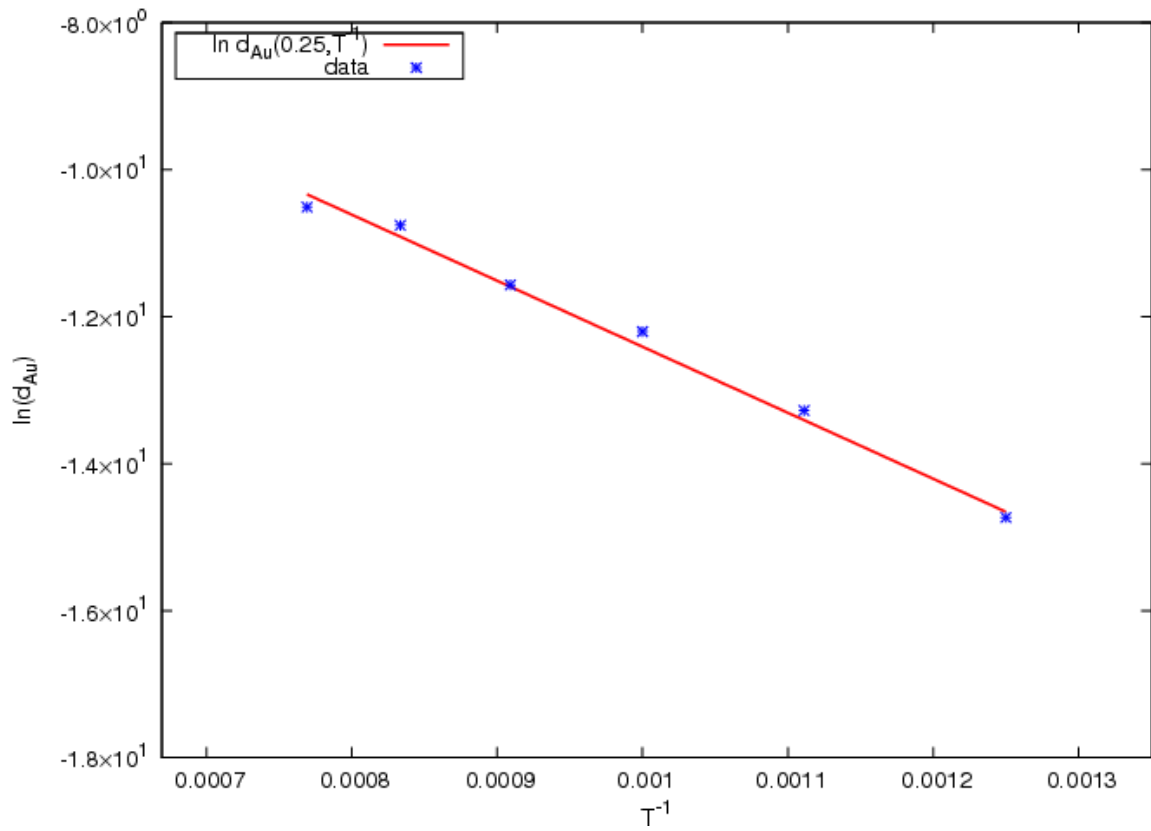


Figure 4.28: Results of kMC simulations of  $d_{Au}$  plotted in Arrhenius form at 25%  $Ag$  concentration for the temperature range 800 – 1300 K.

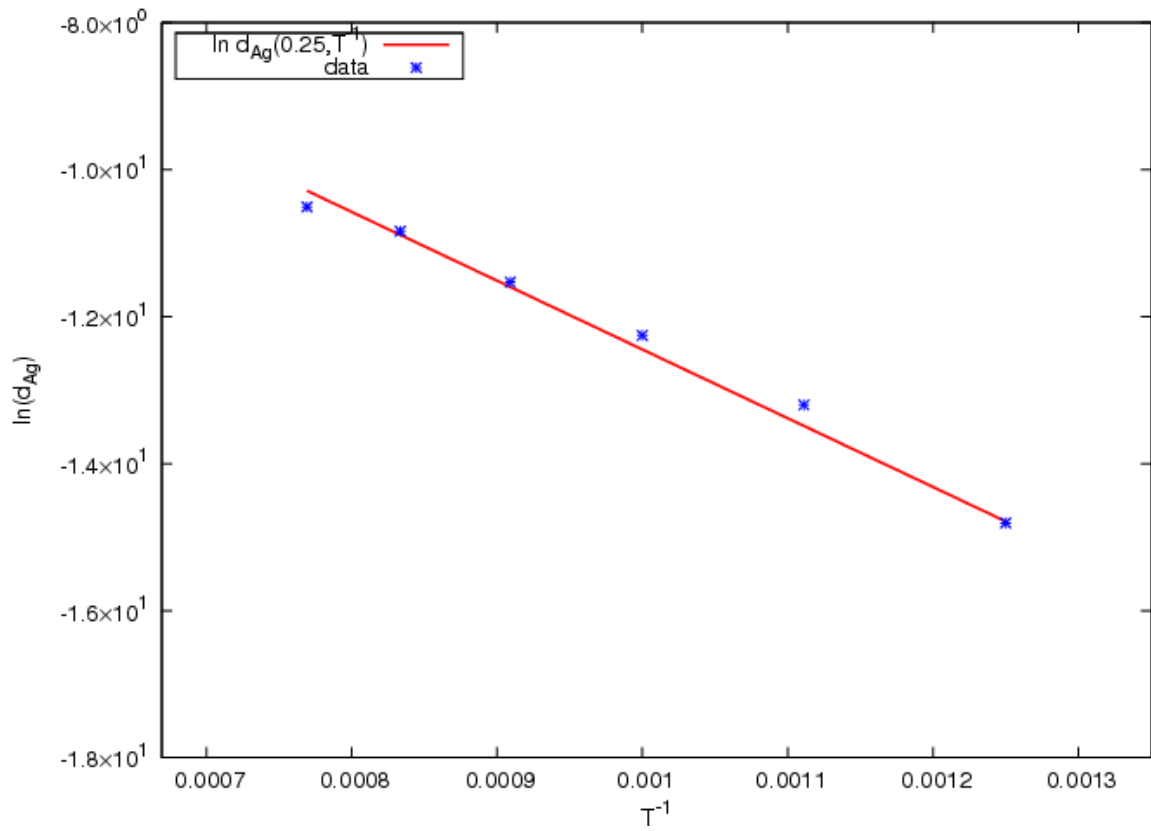


Figure 4.29: Results of kMC simulations of  $d_{Ag}$  plotted in Arrhenius form at 25%  $Ag$  concentration for the temperature range 800 – 1300 K.

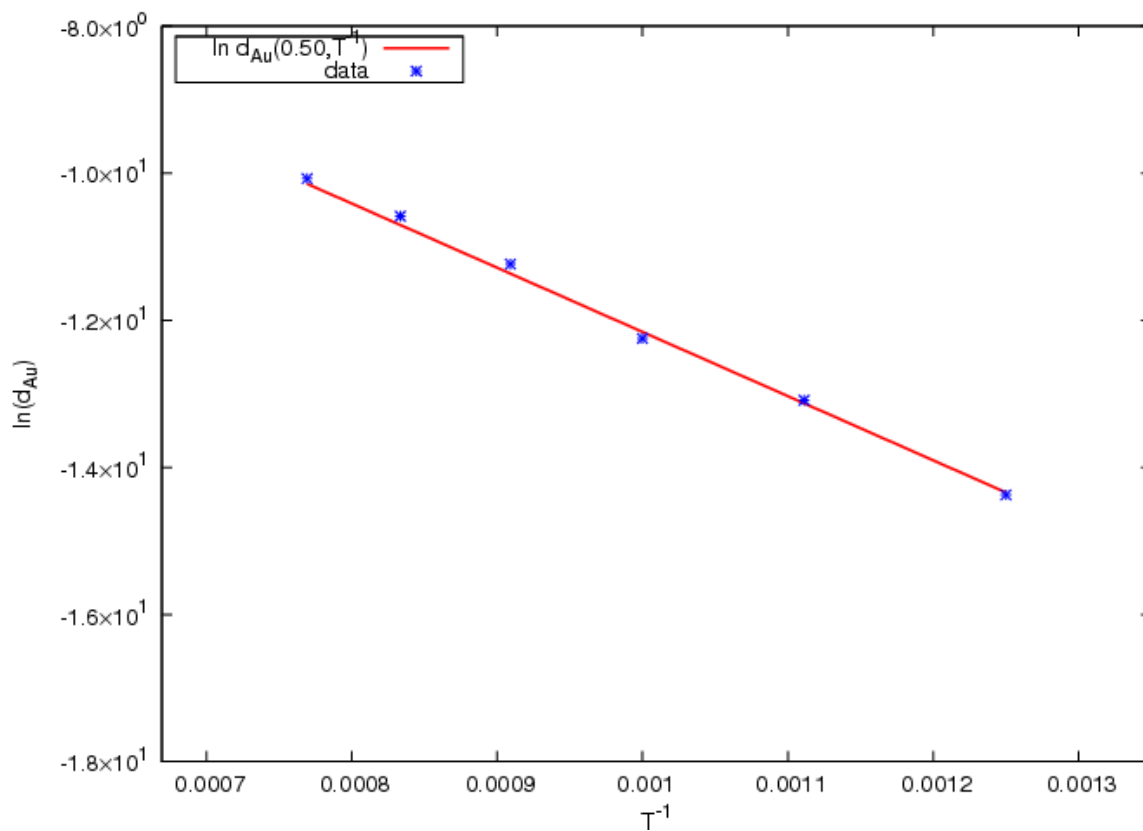


Figure 4.30: Results of kMC simulations of  $d_{Au}$  plotted in Arrhenius form at 50% *Ag* concentration for the temperature range 800 – 1300 K.

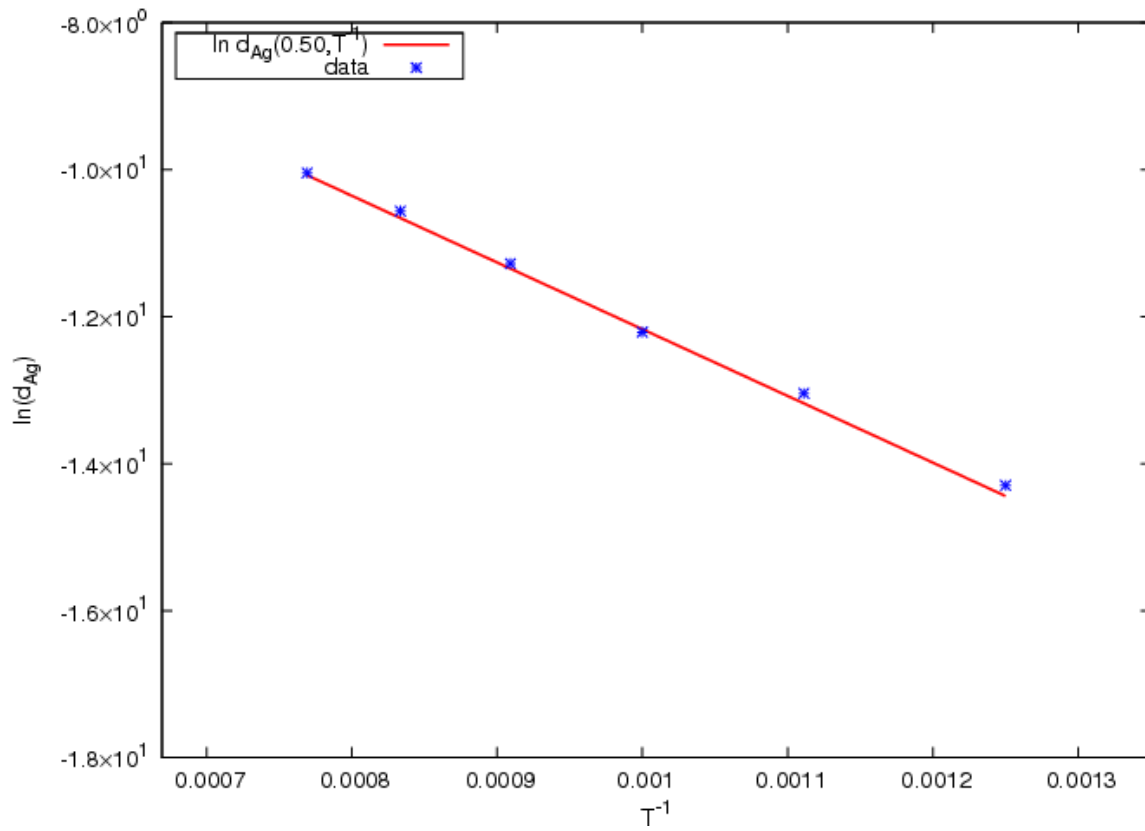


Figure 4.31: Results of kMC simulations of  $d_{Ag}$  plotted in Arrhenius form at 50%  $Ag$  concentration for the temperature range 800 – 1300 K.



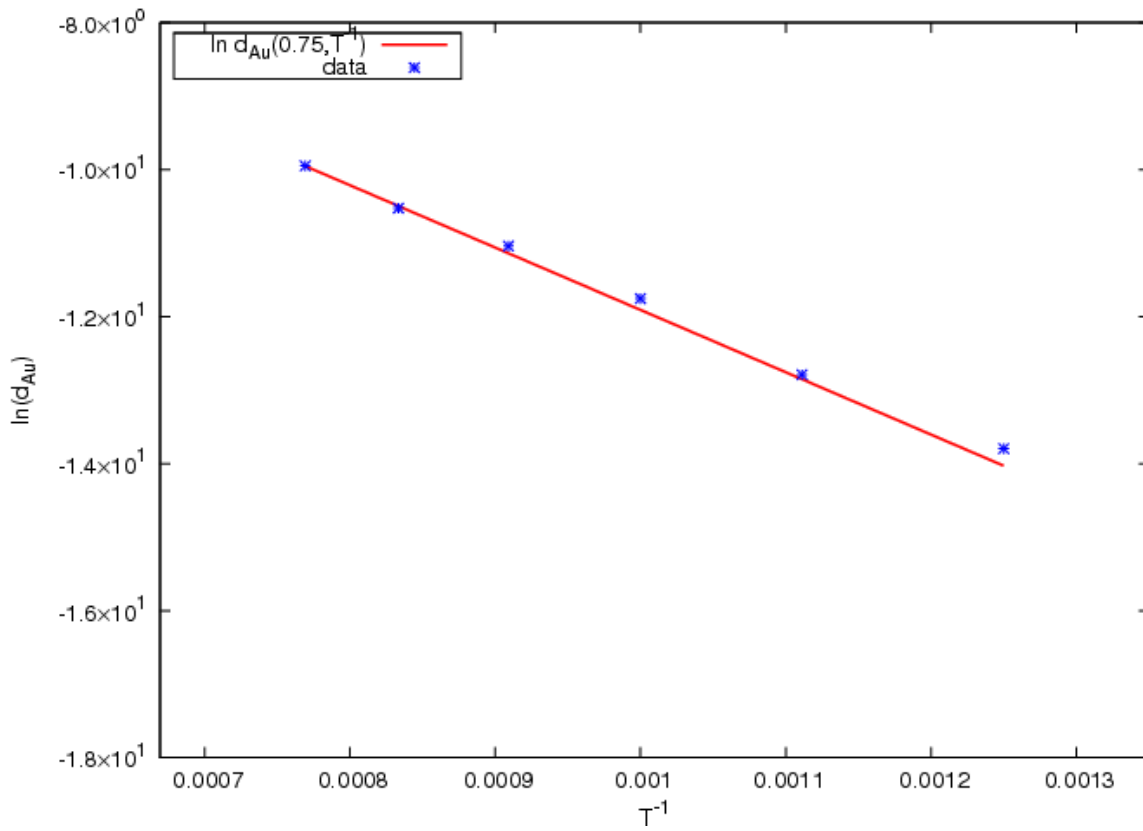


Figure 4.32: Results of kMC simulations of  $d_{Au}$  plotted in Arrhenius form at 75%  $Ag$  concentration for the temperature range 800 – 1300 K.

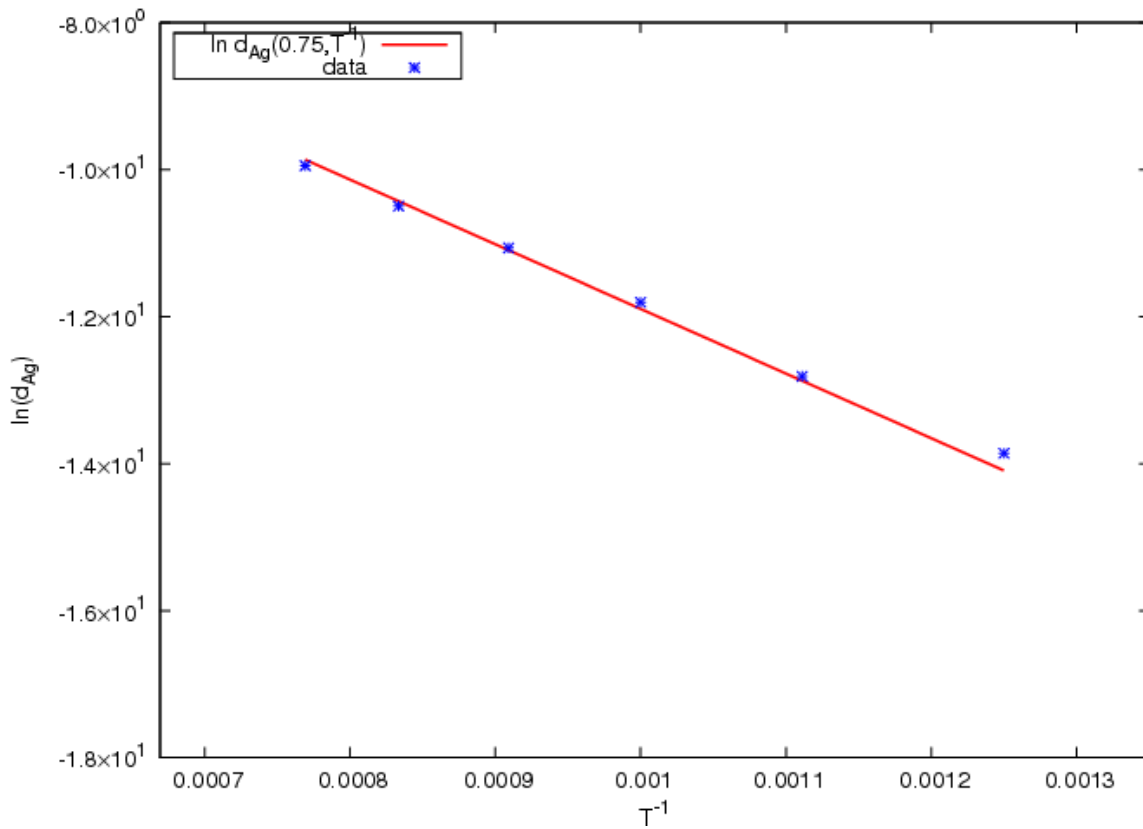


Figure 4.33: Results of kMC simulations of  $d_{Ag}$  plotted in Arrhenius form at 75%  $Ag$  concentration for the temperature range 800 – 1300 K.

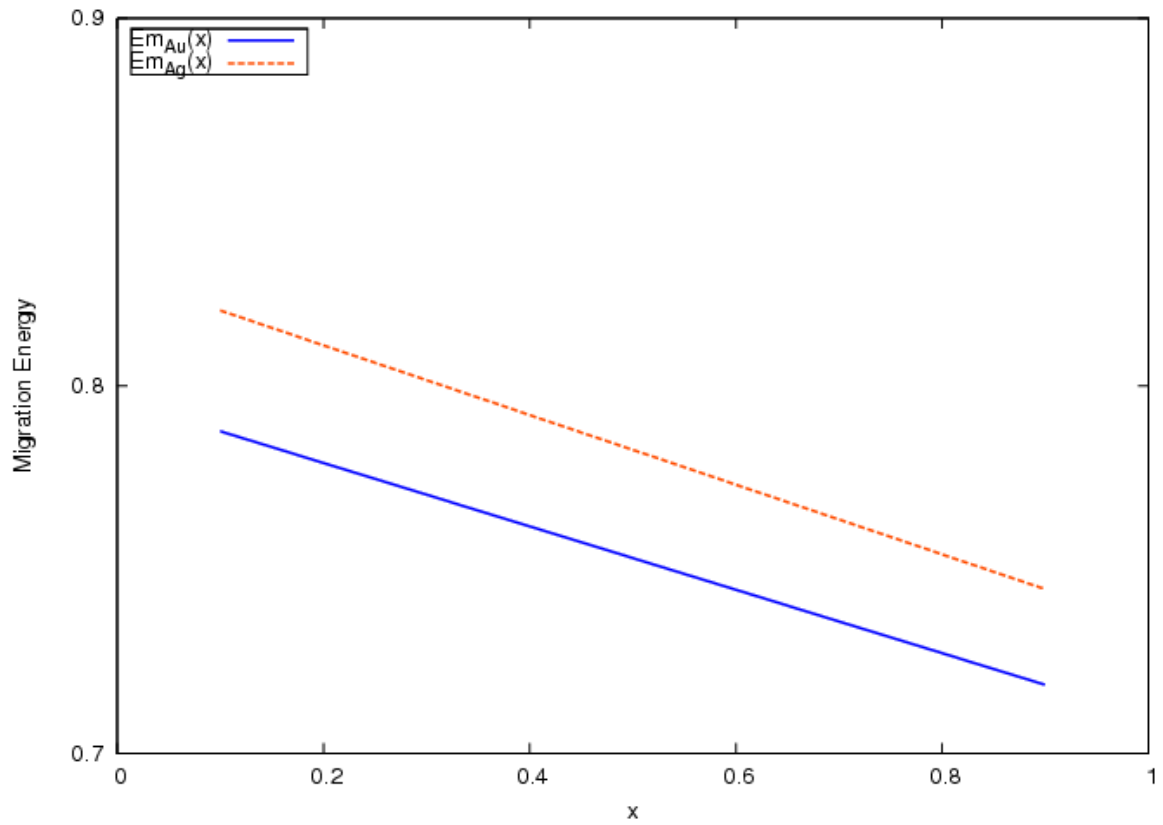


Figure 4.34: Migration energy of both *Au* and *Ag* for *Au – Ag* as a function of *Ag* concentration, which is obtained by the global fitting of kMC results to Eq. 3.11 for all temperatures and compositions.

### 4.3 Mobility of Anti-Phase Boundary in $Ni_3Al$

Crystalline solids have a very regular arrangement of atoms. The local arrangement of atoms or molecules within the crystal repeats itself periodically throughout the structure. However, in real life, this periodicity is not perfect and there are defects in the structure such as point defects, line defects, planar defects, and bulk defects. The Anti-Phase Boundary (APB) can be given as an example of a planar defect. While maintaining the crystallographic direction, the phase on each side of the boundary changes, i.e., ABABBABA. In Fig. (4.36), an APB in (100) direction for  $Ni_3Al$  is shown. Little more than a decade ago, Rong *et al.* identified an unusual process: They observed the translation of the APB in  $Ni_3Al$  [RJS94]. Classic dislocation climb has known to be one of the most important process controlling the deformation in intermetallics [GYKL94].

In this section, the vacancy-assisted microscopic mechanism which allows the translation of an APB perpendicular to its slip plane, and its dependence on temperature are investigated using the same technique, on-the-fly kinetic Monte Carlo, as described in Chapter 3: *Simulation* for two different cases. In the first case, the motion and the “width”<sup>1</sup> of the APB is examined under no driving force for various temperatures ( $T = 1000, 1200$  and  $1500$  K), and in the second case, the motion of the APB is examined under bias for  $T = 1000$  K. This part of the research was carried out on earlier versions of Pflame, thus the Dimer Method is used to find the necessary saddlepoint energies (see, Sec. 3.2).

Possible binding of a vacancy to the APB was examined by Harris *et al.* [HTDM06]. They placed the vacancy at various sites near three ideal APBs and then they calculated the binding energy (relative to bulk). They found that  $V_{Ni}$  was weakly bound

---

<sup>1</sup>The “width” of the APB for an ideal stoichiometry can be thought as a measure of distribution of concentration of anti-site defects at the vicinity of the APB.

(less than 0.1 eV), however they found that the binding of  $V_{Al}$  to be 0.35 and 0.30 eV for the (110) and (111) directions, respectively. So, it is reasonable to think that the vacancy may bind to the APB, and as it wanders, it reshuffles the atoms thus causing one phase to turn into another. In this work and in the Harris *et al.* work, it is found that the binding sites are limited, which means that the vacancy needs to wander off and come back to accomplish a translation of the APB as opposing to the “zipper” effect (see Fig. 4.35) as one would expect.

In the absence of a driving force, the vacancy may wander off either side of the APB, thus making the conversion of one phase into another reversible. This motion has the characteristic of a random walk. However, in the presence of a driving force, APB will drift in the direction of the driving force with a velocity proportional this force.

In this work, a periodic  $Ni_3Al$  slab of 1280 sites with an abrupt APB is set up with ideal stoichiometry (see, Fig 4.36). Only one vacancy is introduced on the APB and its concentration is fixed throughout the calculations. Every atom on each site is free to move except the first 256, and the last 256 atoms (see, Fig. 4.37). This means that the atoms in these regions are not allowed to exchange places with the vacancy. This puts boundaries on the motion of the APB perpendicular to its slip plane. An external driving force is not present, however, when the APB approaches the non-movable region, the degree of the freedom of the vacancy at the vicinity of the non-movable region is decreased, thus biasing the motion to move towards the middle.

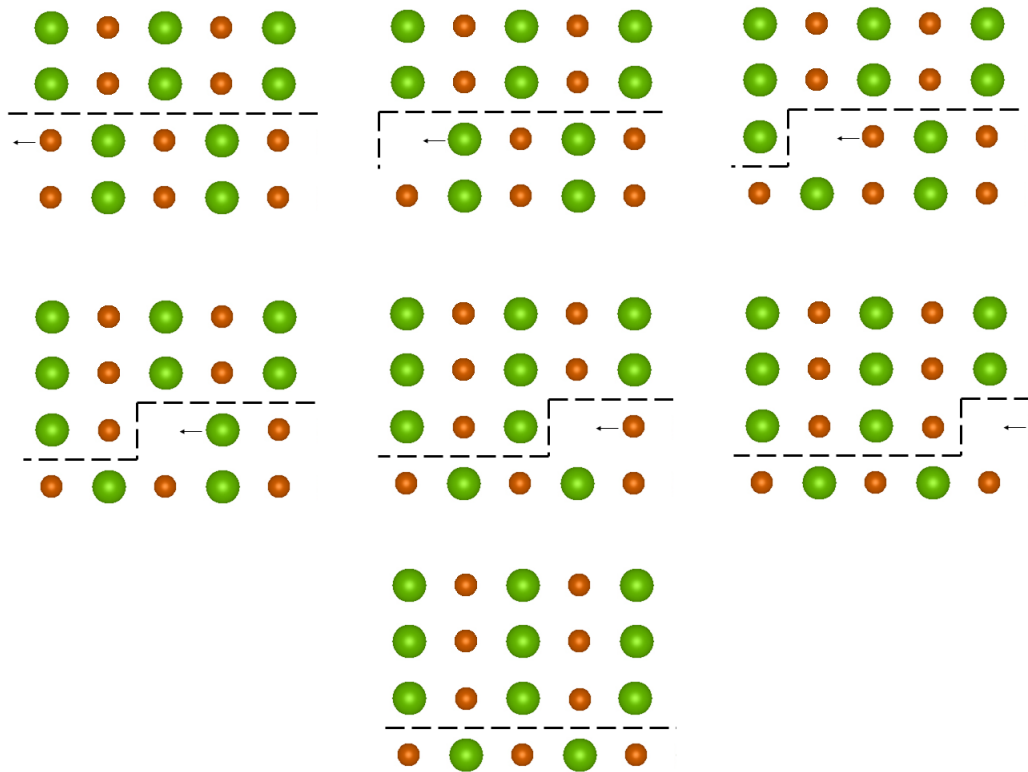


Figure 4.35: Zipper effect: If the vacancy is bound to a region near the APB, this shows the easiest way to translate the APB.

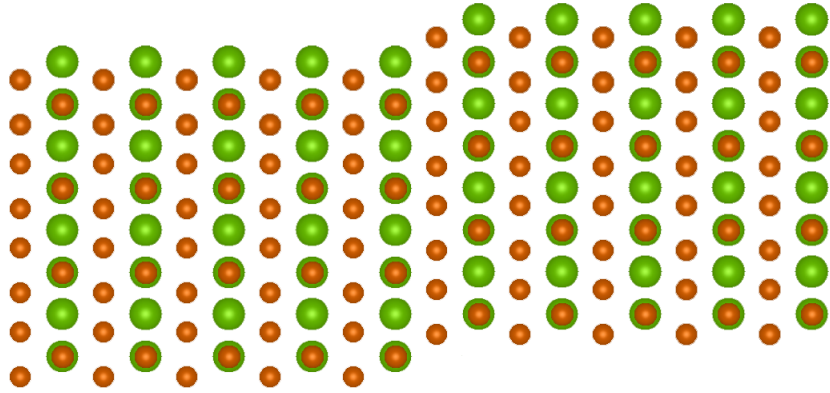


Figure 4.36: (100) APB in  $Ni_3Al$ .

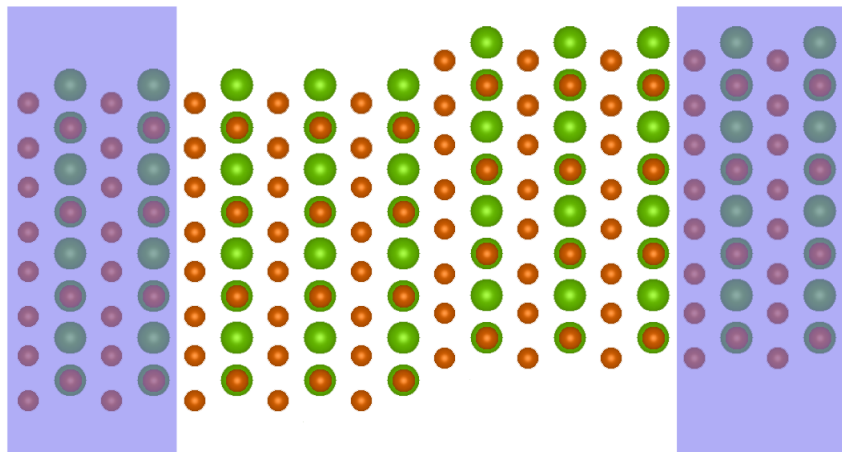


Figure 4.37: (100) APB in  $Ni_3Al$  with two non-movable region (blue shaded) on each side putting boundaries on the APB's motion perpendicular to its slip plane.

The nature of the motion, the mobility and the width of the APB, is examined for  $T = 1000, 1200$  and  $1500$  K. We intended to examine larger range of temperatures (i.e.  $T = 1000 - 2000$  K), however, the simulation takes a long time to be able to observe any significant motion of the APB. One of the main reason is that after a vacancy translates a certain region of the APB, it leaves the APB and starts wandering around, when it comes back, it translates another portion of the APB. The overall

effect is the translation of the whole APB perpendicular to its slip plane. In this work, we initially ran the sample six to ten times with 5000 Monte Carlo steps each, feeding the previous run’s final configuration to the next run as an initial configuration.

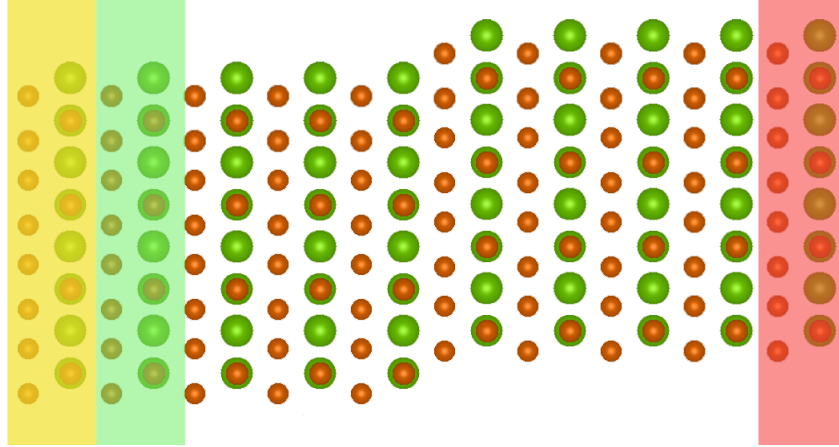


Figure 4.38: Visual definition of *layer* for the (100) APB  $Ni_3Al$  sample. The first two planes (yellow shaded) are designated as *layer* number 1, the following two planes (green shaded) are designated as *layer* number 2, etc. The last two planes (red shaded) are designated as *layer* number 10. There are a total of ten *layers*.

To examine the configurations, we defined “layers” (see, Fig. 4.38). Starting from the left end, each two planes of sites perpendicular to (100) is designated as “one” layer. In the sample, we have ten layers. For each layer we did a histogram of which lattice site  $Al$  atoms occupy. In an FCC alloy, there are four different sites that atoms can occupy. These sites are shown in Fig. 4.39.

In the first case, the APB is positioned in the middle (between the fifth and the sixth layer), far enough from both ends not to be biased due to the non-movable region. The histogram of the initial configuration is given in *Table* 4.3. For the first five layers, all  $Al$  atoms reside on site one. Due to phase shift (APB) after the fifth layer,  $Al$  atoms now reside on site three. There are total 32  $Al$  atoms per layer. As the vacancy wanders around the APB, it will introduce anti-site defects. One expects



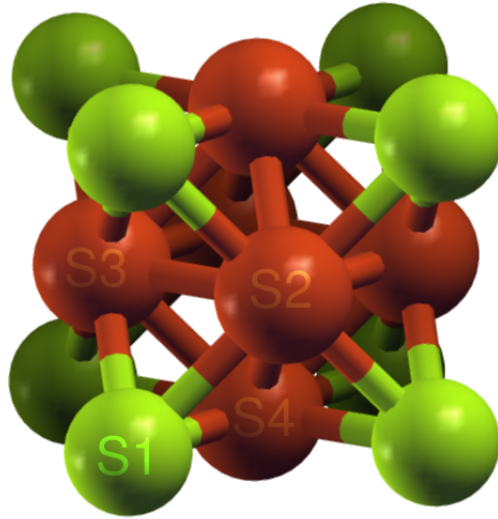


Figure 4.39: Four sites of an FCC ( $L1_2$ ): Site 1 (S1), Site 2 (S2), Site 3 (S3) and Site 4 (S4).

the concentration of these anti-site defects to depend on the temperature. To reduce the statistical variations, we averaged the histogram over intermediate configurations of each run (each run has ten intermediate configurations). The averaged histogram after the third run at  $T = 1000$  K is given in *Table 4.4*. Readers should notice that even after the third run (total 15000 MC steps), the concentration of anti-site defects drop down fast as one goes away from the initial position of the APB (between the fifth and the sixth layer). This indicates some degree of vacancy-APB bonding and it also shows how slow the process actually is. The distribution of the concentration of anti-site defects about the middle suggests that the vacancy didn't have a preferred direction to move, as one expects.

The histograms of the final configurations for the runs at  $T = 1000, 1200$  and  $1500$  K are given in *Table 4.5*, *Table 4.6* and *Table 4.7*, respectively.

Layer	S1	S2	S3	S4
1	32	0	0	0
2	32	0	0	0
3	32	0	0	0
4	32	0	0	0
5	32	0	0	0
6	0	0	32	0
7	0	0	32	0
8	0	0	32	0
9	0	0	32	0
10	0	0	32	0

Table 4.3: Histogram of sites  $Al$  atoms occupy per layer for the initial configuration. There are total 32  $Al$  atoms per layer. Due to phase shift (remember, APB) after the fifth layer,  $Al$  atoms now reside on site three.

The increasing and the spreading out distribution of the concentration of the anti-site defects clearly shows a temperature dependence. As the temperature increases, the width increases.

Layer	S1	S2	S3	S4
1	32	0	0	0
2	32	0	0	0
3	32	0.4	0	0.2
4	31	0	1	0.5
5	28.5	0.2	2	0.3
6	4.6	0.8	25.2	0.3
7	0.1	0.8	32	0.1
8	0.4	0	31.6	0
9	0	0	32	0
10	0	0	32	0

Table 4.4: The averaged histogram of sites  $Al$  atoms occupy per layer over intermediate configurations after the third run at  $T = 1000$  K. Initially the APB was positioned in the middle (between the fifth and the sixth layer). The histogram for the first two and the last two layers are not allowed to change due to the non-movable region.

*Table 4.10* shows a snapshot of a run at  $T=1000$ K under no driving force. After the vacancy shuffling of some portions of the APB, it wanders off to the 3rd layer. Another snapshot taken at a later time (see *Table 4.11*) shows that the vacancy comes back again and continues to shuffle the atoms at the vicinity of the APB. This observation is consistent with Harris *et al.*'s work. The binding to the APB, as one would expect, doesn't cause the *zipper* effect.

In the second case, the APB is initially positioned closer to the non-movable region (between the seventh and the eighth layer, see Fig. 4.40). The histogram of the initial configuration is given in Table. 4.8. For the first seven layers, all  $Al$  atoms reside on site one. Due to phase shift (APB) after the seventh layer,  $Al$  atoms now reside on site three. The averaged histogram after the third run at  $T = 1000$  K is given in *Table 4.9* as an example.

Layer	S1	S2	S3	S4
1	32	0	0	0
2	32	0	0	0
3	31.9	0.9	0.3	0.2
4	31.7	0	0.1	0.4
5	27.3	0.1	3	0.6
6	9.6	0.4	19.8	1.2
7	0.1	0.5	31.9	0
8	0	0	32	0
9	0	0	32	0
10	0	0	32	0

Table 4.5: The averaged histogram of sites  $Al$  atoms occupy per layer over intermediate configurations for the final configuration at  $T = 1000$  K. Initially the APB was positioned in the middle (between the fifth and the sixth layer). The histogram for the first two and the last two layers are not allowed to change due to the non-movable region.

Layer	S1	S2	S3	S4
1	32	0	0	0
2	32	0	0	0
3	28	0.1	3.6	0
4	30.7	0.9	0.1	0.3
5	23.3	0.9	2.8	1.3
6	6.8	3.8	17.7	2.5
7	2.1	4.6	28.2	0.6
8	1.1	1.8	29.2	1.6
9	0	0	32	0
10	0	0	32	0

Table 4.6: The averaged histogram of sites  $Al$  atoms occupy per layer over intermediate configurations for the final configuration at  $T = 1200$  K. Initially the APB was positioned in the middle (between the fifth and the sixth layer). The histogram for the first two and the last two layers are not allowed to change due to the non-movable region.

Layer	S1	S2	S3	S4
1	32	0	0	0
2	32	0	0	0
3	25.4	1.6	1.8	1.8
4	17.2	4.8	5.5	2.1
5	8	5.7	11.7	4.3
6	7.2	5	15.1	3.8
7	5.8	10.8	10	4.7
8	6.6	6.9	19.4	6.8
9	0	0	32	0
10	0	0	32	0

Table 4.7: The averaged histogram of sites  $Al$  atoms occupy per layer over intermediate configurations for the final configuration at  $T = 1500$  K. Initially the APB was positioned in the middle (between the fifth and the sixth layer). The histogram for the first two and the last two layers are not allowed to change due to the non-movable region.

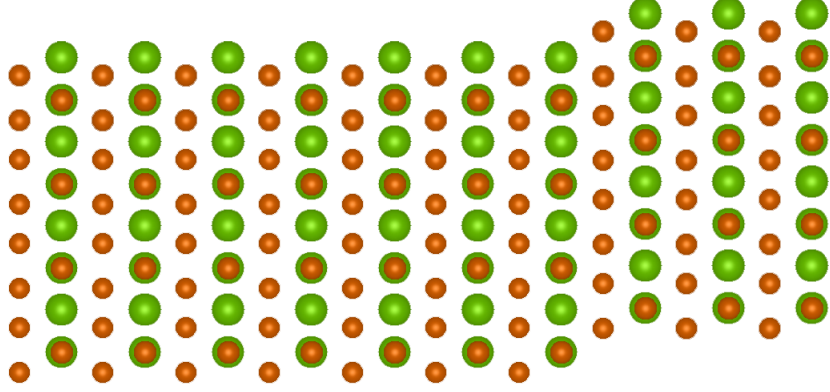


Figure 4.40: (100) APB positioned closer the right “wall”.

Readers should notice the effect of the non-movable region on the immediate position of the APB. The vacancy preferred to move towards the middle creating more anti-site defects than staying closer to the “wall”. However, even the motion towards the wall is not favored, due to the random walk nature of the vacancy, some anti-site defects are still observed on layer eight.

The favored motion of the vacancy towards the middle (due to the wall) acts like a “driving force” on the APB. As the vacancy translates the APB, the abrupt shape of the APB starts to disappear. The higher the temperature, the less abrupt the APB becomes. The “width” of the APB for an ideal stoichiometry can be thought as a measure of distribution of concentration of anti-site defects at the vicinity of the APB. One can try to fit  $\tanh$  to the average histogram for both site one and site three in the form

$$a \tanh (b x + c) + d \quad (4.4)$$

where  $a, b, c$  and  $d$  are the fitting parameters and  $x$  is the layer number. The parameter  $b$  is responsible for the width of  $\tanh$ , and the parameter  $c$  for positioning the center. A relationship between these parameters and the dispersion of the APB can

Layer	S1	S2	S3	S4
1	32	0	0	0
2	32	0	0	0
3	32	0	0	0
4	32	0	0	0
5	32	0	0	0
6	32	0	0	0
7	32	0	0	0
8	0	0	32	0
9	0	0	32	0
10	0	0	32	0

Table 4.8: Histogram of sites  $Al$  atoms occupy per layer for the initial configuration. There are total 32  $Al$  atoms per layer. Due to phase shift (remember– APB) after the seventh layer,  $Al$  atoms now reside on site three.

be formulated.



Layer	S1	S2	S3	S4
1	32	0	0	0
2	32	0	0	0
3	32	0	0	0
4	32	0	0	0
5	31.7	0.1	0.5	0.4
6	29.2	0.1	1.1	0.8
7	17.6	0.9	10.6	1.6
8	0	0.8	32	0
9	0	0	32	0
10	0	0	32	0

Table 4.9: The averaged histogram of sites  $Al$  atoms occupy per layer over intermediate configurations for the third run at  $T = 1000$  K. The histogram for the first two and the last two layers are not allowed to change due to the non-movable region.

Layer	S1	S2	S3	S4
1	32	0	0	0
2	32	0	0	0
3	31	0	0	1
4	32	0	0	0
5	32	0	0	0
6	0	0	32	0
7	0	0	31	0
8	0	0	32	1
9	0	0	32	0
10	0	0	32	0

Table 4.10: An early snapshot of the configuration of the simulation running at  $T=1000$ K under no driving force.

Layer	S1	S2	S3	S4
1	32	0	0	0
2	32	0	0	0
3	30	0	1	1
4	32	0	0	0
5	30	0	1	0
6	4	0	26	1
7	1	1	32	0
8	0	0	32	0
9	0	0	32	0
10	0	0	32	0

Table 4.11: A later snapshot of the configuration of the simulation running at  $T=1000\text{K}$  under no driving force.

The following figures show the width and the mobility of the APB and are the snapshots of the simulation run at  $T = 1000 \text{ K}$  (the second case: APB positioned closer to the “wall”), fitted *tanh* to the averaged histogram of site one and site three.

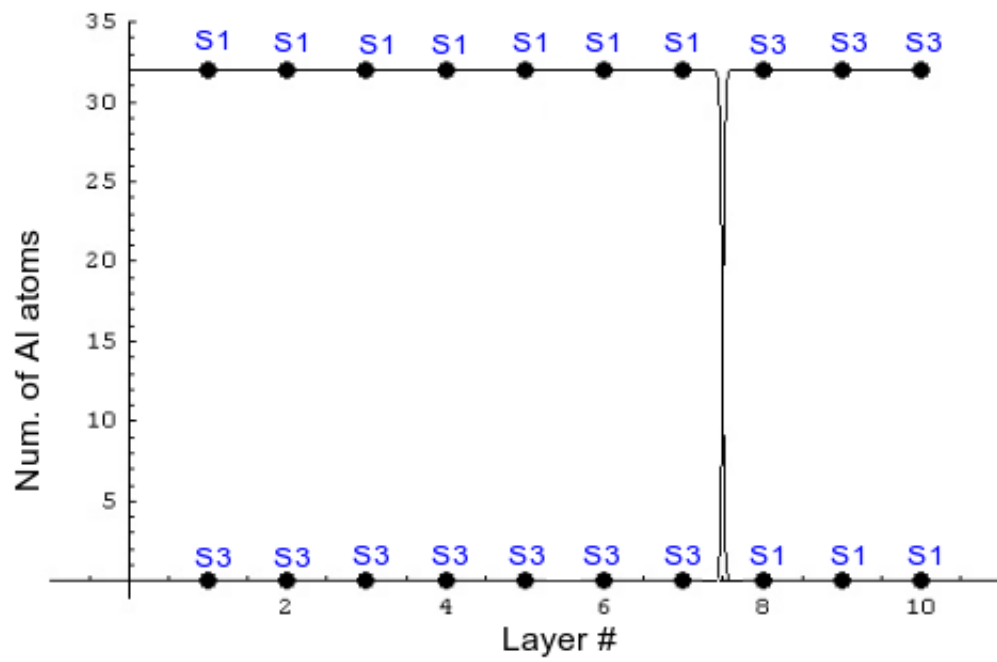


Figure 4.41: The position and the width of (100) APB for the initial configuration.

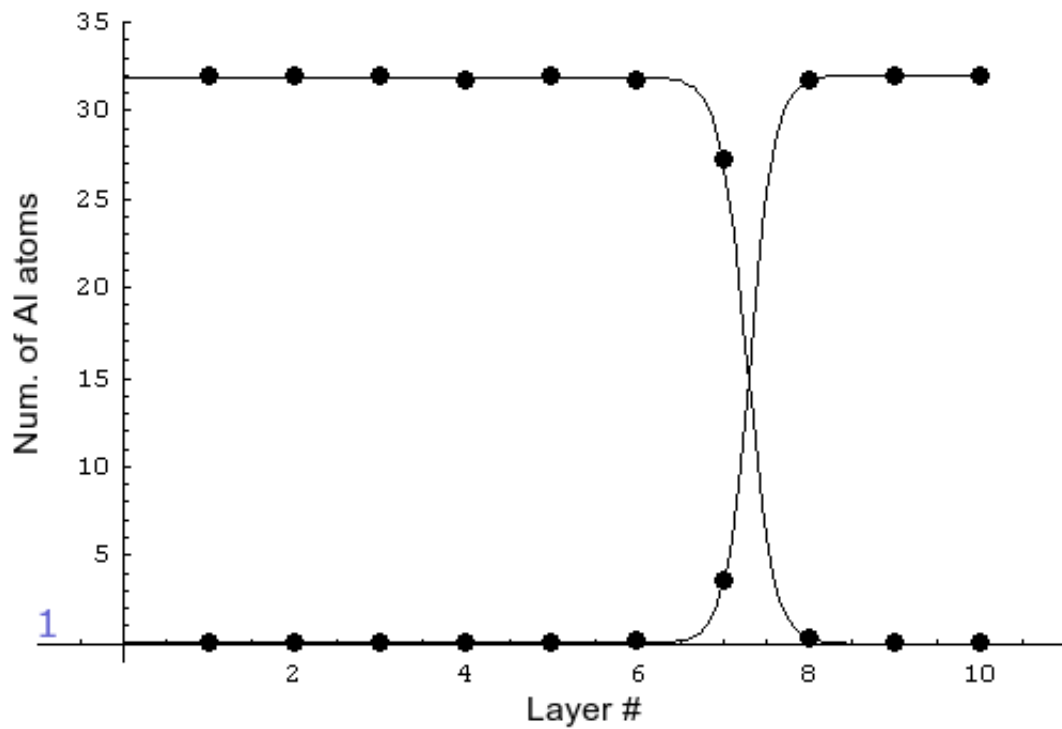


Figure 4.42: The first snapshot of the simulation running at  $T = 1000$  K showing the position and the width of (100) APB. Number of *Al* atoms vs. layer number is plotted, the fitted *tanh* to site one and site three are also shown.

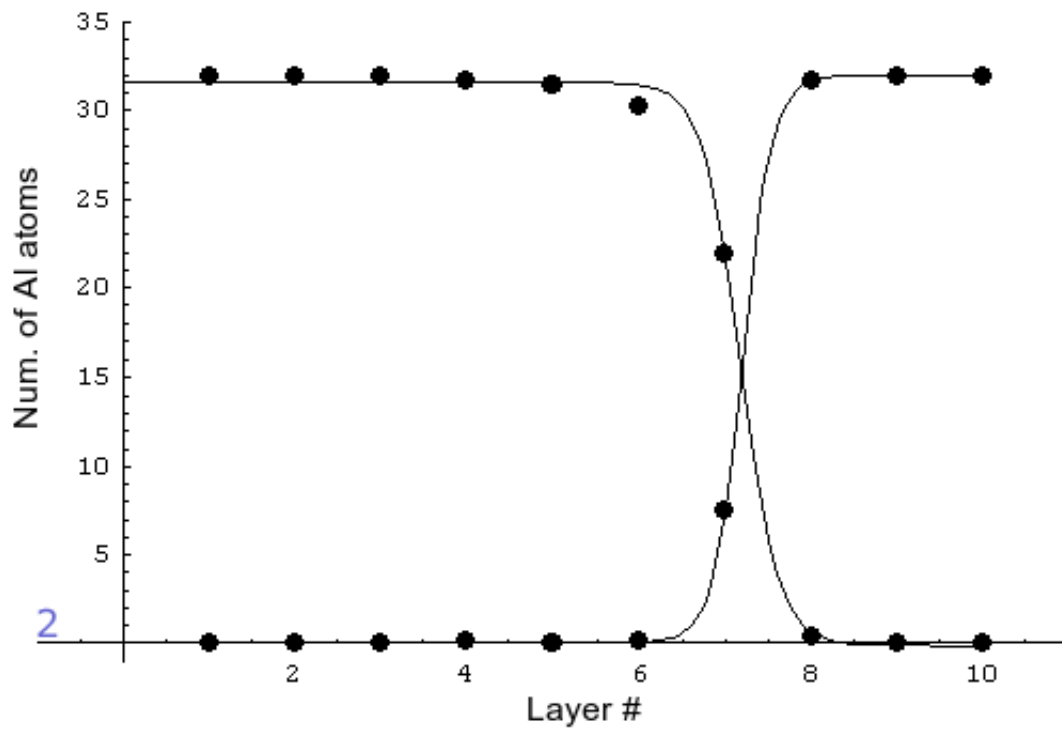


Figure 4.43: The second snapshot of the simulation running at  $T = 1000$  K showing the position and the width of (100) APB. Number of *Al* atoms vs. layer number is plotted, the fitted *tanh* to site one and site three are also shown.

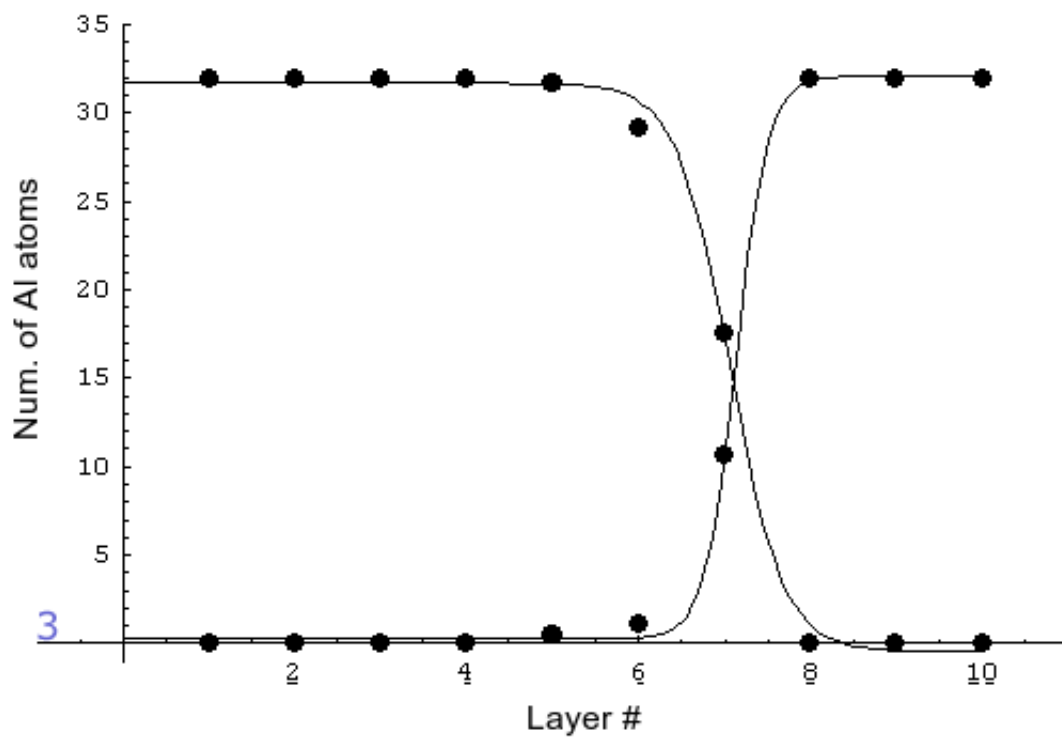


Figure 4.44: The third snapshot of the simulation running at  $T = 1000$  K showing the position and the width of (100) APB. Number of *Al* atoms vs. layer number is plotted, the fitted *tanh* to site one and site three are also shown.

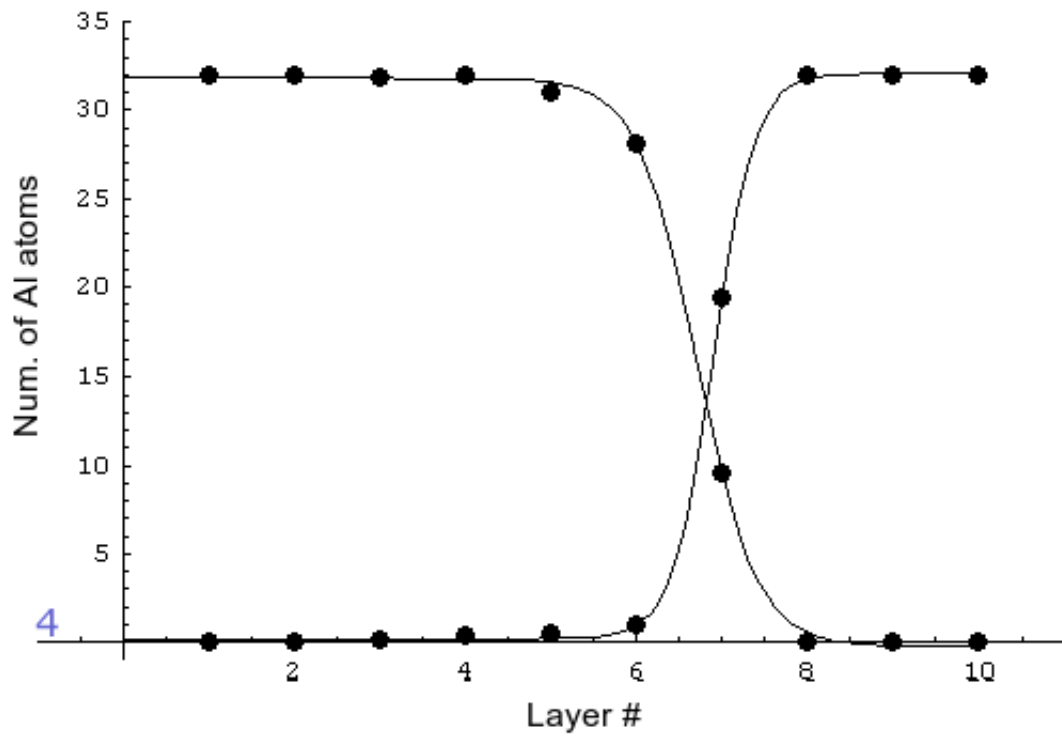


Figure 4.45: The fourth snapshot of the simulation running at  $T = 1000$  K showing the position and the width of (100) APB. Number of *Al* atoms vs. layer number is plotted, the fitted *tanh* to site one and site three are also shown.

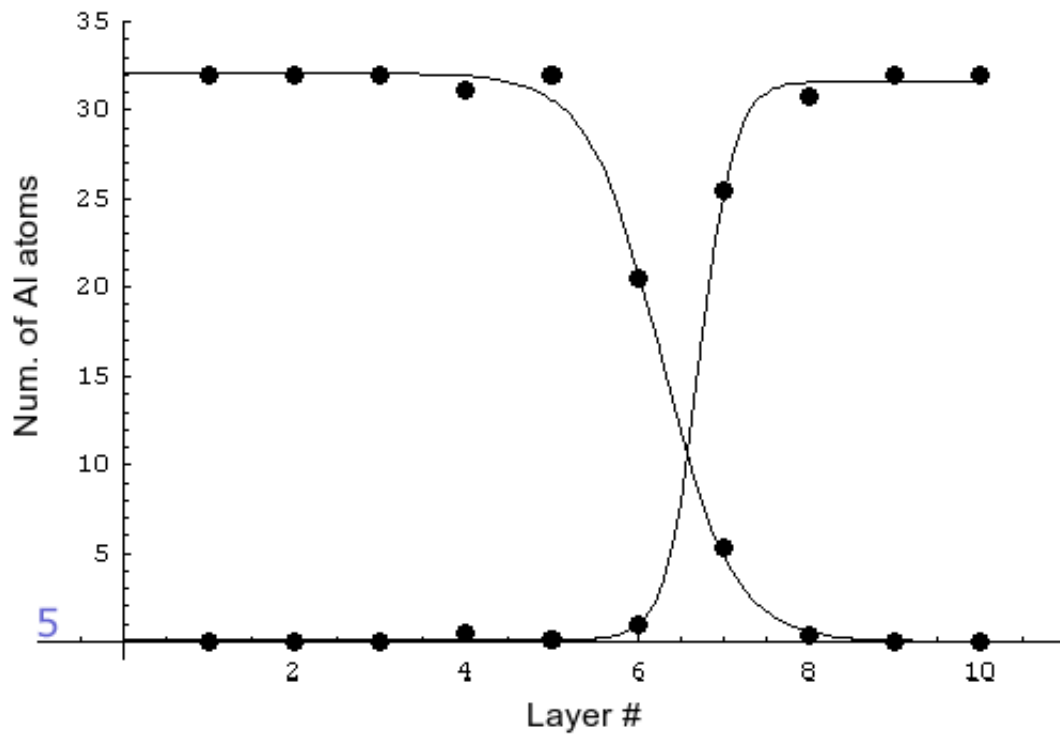


Figure 4.46: The fifth snapshot of the simulation running at  $T = 1000$  K showing the position and the width of (100) APB. Number of *Al* atoms vs. layer number is plotted, the fitted *tanh* to site one and site three are also shown.



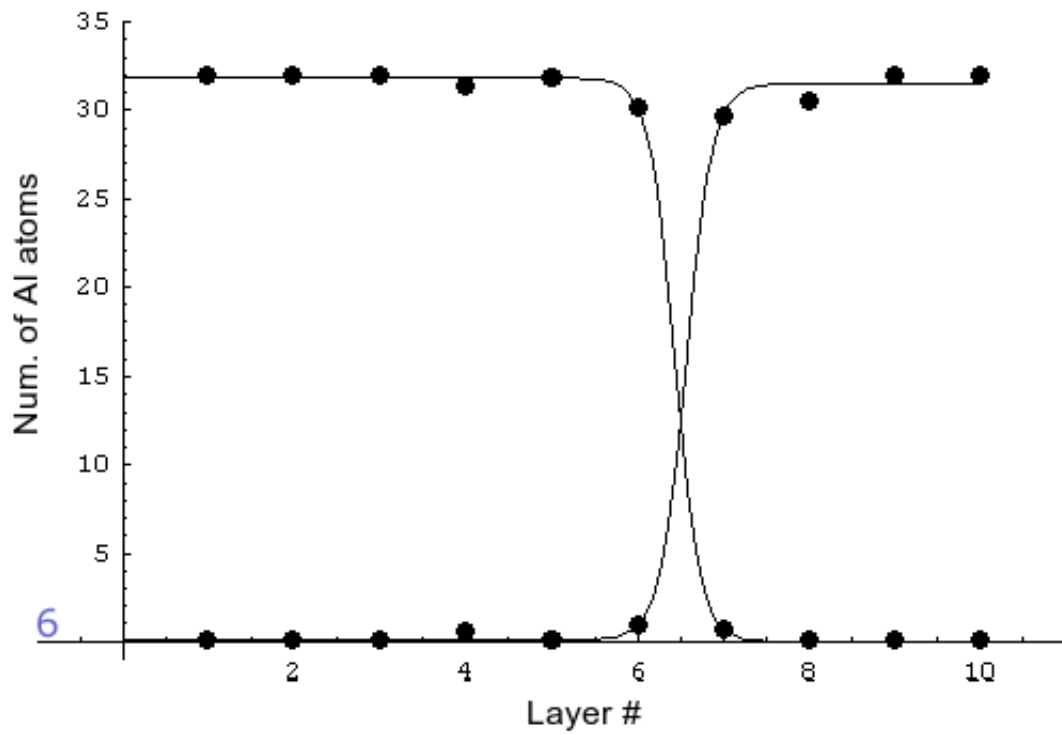


Figure 4.47: The sixth snapshot of the simulation running at  $T = 1000$  K showing the position and the width of (100) APB. Number of *Al* atoms vs. layer number is plotted, the fitted *tanh* to site one and site three are also shown.

## Chapter 5

# Sandtrap Limitation and How to Overcome it

During the simulations at low temperatures, we sometimes come across configurations in ordered phase where the vacancy spends a large number of steps moving locally without accomplishing significant displacements or accumulating much simulated time.

In such configurations, we find that the vacancy is trapped between two valleys where the saddlepoint energy between these two valleys is much smaller than the saddlepoint energies necessary to escape from one of the other 11 exits, thus causing the vacancy to hop back and forth. Even though there is a very small chance of an escape, the vacancy spends most of its time in this “sandtrap”, making the simulation very inefficient. A 1-D representation of the energy valleys of this *sandtrap* is shown in *Fig. 5.1*. To tackle this problem, we calculate the escape probabilities and the elapsed time for an escape jump to take place for 1-D by averaging over all possible jumps within this trap, i.e., starting in valley  $a$ , an escape can take place from exit  $A$  with the first jump, or it can jump to valley  $b$  and escape from exit  $B$ . Or instead

of exiting from exit  $B$ , it may come back to valley  $a$  and exit from exit  $A$ , etc.

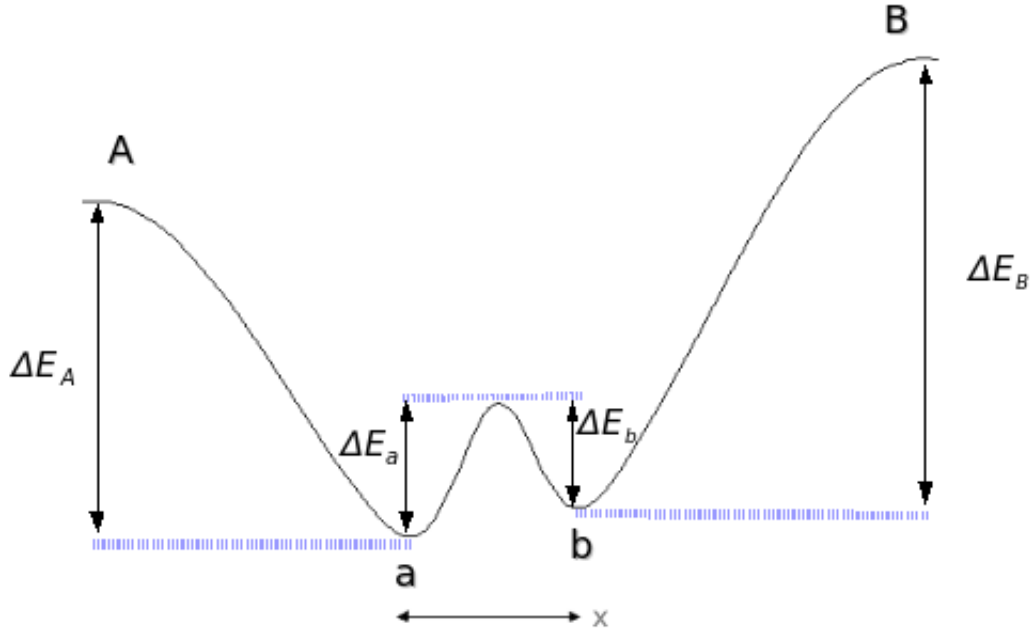


Figure 5.1: 1-D representation of the “sandtrap” for two energy valleys ( $\Delta E$ 's are not necessarily equal) as a function of displacement.

The probability of a jump from valley  $a$  to valley  $b$  can be written as (see Fig. 5.1)

$$P_a = C_{aA} e^{-\Delta E_a/kT}. \quad (5.1)$$

Similarly, the probability from valley  $a$  to *exit*  $A$ ,

$$P_A = C_{aA} e^{-\Delta E_A/kT}, \quad (5.2)$$

from valley  $b$  to valley  $a$ ,

$$P_b = C_{bB} e^{-\Delta E_b/kT}, \quad (5.3)$$

and from valley  $b$  to *exit*  $B$ ,

$$P_B = C_{bB} e^{-\Delta E_B/kT} \quad (5.4)$$

where  $k$  is the Boltzmann constant,  $T$  is the temperature, the  $\Delta E$ 's are the energy barriers to be crossed (saddlepoint energies), and the  $C$ 's are the normalization coefficients. We can also write

$$\begin{aligned} P_A + P_a &= 1 \\ P_B + P_b &= 1 \end{aligned} \quad (5.5)$$

then the coefficients are

$$\begin{aligned} C_{aA} &= \frac{1}{e^{-\Delta E_a/kT} + e^{-\Delta E_A/kT}} \\ C_{bB} &= \frac{1}{e^{-\Delta E_b/kT} + e^{-\Delta E_B/kT}} \end{aligned} \quad (5.6)$$

and time steps associated with each jump can be written as

$$\begin{aligned} t_a &= \tau_{aA} e^{\Delta E_a/kT} \\ t_A &= \tau_{aA} e^{\Delta E_A/kT} \\ t_b &= \tau_{bB} e^{\Delta E_b/kT} \\ t_B &= \tau_{bB} e^{\Delta E_B/kT} \end{aligned} \quad (5.7)$$

respectively, where  $\tau$ 's are constants.

First, let's assume that we start in valley  $a$ , then we can write

$$\langle t_{a \rightarrow A} \rangle = \frac{\sum_{n=0}^{\infty} P_A P_a^n P_b^n (nt_a + nt_b + t_A)}{\sum_{n=0}^{\infty} P_A P_a^n P_b^n} = t_A \left( \frac{2t_a t_B + t_a t_b + t_B t_b + t_A t_b}{t_a t_B + t_a t_b + t_A t_b} \right) \quad (5.8)$$

and

$$\begin{aligned} \langle t_{a \rightarrow B} \rangle &= \frac{\sum_{n=0}^{\infty} P_B P_a^{(n+1)} P_b^n ((n+1)t_a + nt_b + t_B)}{\sum_{n=0}^{\infty} P_B P_a^{(n+1)} P_b^n} \\ &= \frac{t_a^2 t_B + t_a t_B^2 + t_a t_B t_A + t_a^2 t_b + t_a t_B t_b + t_a t_A t_b + 2t_B t_A t_b}{t_a t_B + t_a t_b + t_A t_b} \end{aligned} \quad (5.9)$$

Eq 5.8 and Eq. 5.9 give the average time for an escape jump to take place from exit  $A$  and exit  $B$ , respectively.

Similarly, if we start from valley  $b$ , then we can write

$$\begin{aligned}
\langle t_{b \rightarrow A} \rangle &= \frac{\sum_{n=0}^{\infty} P_A P_b^{(n+1)} P_a^n ((n+1)t_b + nt_a + t_A)}{\sum_{n=0}^{\infty} P_A P_b^{(n+1)} P_a^n} \\
&= \frac{2t_a t_B t_A + t_a t_B t_b + t_a t_A t_b + t_B t_A t_b + t_A^2 t_b + t_a t_b^2 + t_A t_b^2}{t_a t_B + t_a t_b + t_A t_b}
\end{aligned} \tag{5.10}$$

and

$$\langle t_{b \rightarrow B} \rangle = \frac{\sum_{n=0}^{\infty} P_B P_b^n P_a^n (nt_b + nt_a + t_B)}{\sum_{n=0}^{\infty} P_B P_b^n P_a^n} = t_B \left( \frac{t_a t_B + t_a t_A + t_a t_b + 2t_A t_b}{t_a t_B + t_a t_b + t_A t_b} \right) \tag{5.11}$$

Eq 5.10 and Eq 5.11 give the averaged time for an escape jump to take place from exit  $A$  and exit  $B$ , respectively.

If we generalize this idea to 11 exits, we can write the exit probabilities from valley  $a$  to exit  $A$ 's as

$$\begin{aligned}
P_{A1} &= C_{aA} e^{-\Delta E_{A1}/kT} \\
P_{A2} &= C_{aA} e^{-\Delta E_{A2}/kT} \\
&\vdots \\
P_{A11} &= C_{aA} e^{-\Delta E_{A11}/kT}
\end{aligned} \tag{5.12}$$

and the probability to jump from valley  $a$  to valley  $b$  as

$$P_a = C_{aA} e^{-\Delta E_a/kT} \tag{5.13}$$

where  $\Delta E_A$ 's (and  $\Delta E_a$ ) are the energy barriers to be crossed,  $k$  is the Boltzmann constant,  $T$  is the temperature, and the coefficient  $C_{aA}$  is determined from the normalization,

$$P_{A1} + P_{A2} + \dots + P_{A11} + P_a = 1 \tag{5.14}$$

thus  $C_{aA}$  is

$$C_{aA} = \frac{1}{e^{-\Delta E_{A1}/kT} + e^{-\Delta E_{A2}/kT} + \dots + e^{-\Delta E_{A11}/kT} + e^{-\Delta E_a/kT}} \quad (5.15)$$

and the time steps associated with each jump can be written as

$$\begin{aligned} t_{A1} &= \tau_{aA} e^{\Delta E_{A1}/kT} \\ t_{A2} &= \tau_{aA} e^{\Delta E_{A2}/kT} \\ &\vdots \\ t_{A11} &= \tau_{aA} e^{\Delta E_{A11}/kT} \\ t_a &= \tau_{aA} e^{\Delta E_a/kT} \end{aligned} \quad (5.16)$$

respectively, where  $\tau$ 's are constants.

Similarly, the escape probabilities from valley  $b$  to exit  $B$  are

$$\begin{aligned} P_{B1} &= C_{bB} e^{-\Delta E_{B1}/kT} \\ P_{B2} &= C_{bB} e^{-\Delta E_{B2}/kT} \\ &\vdots \\ P_{B11} &= C_{bB} e^{-\Delta E_{B11}/kT} \end{aligned} \quad (5.17)$$

and the probability to jump from valley  $b$  to valley  $a$  is

$$P_b = C_{bB} e^{-\Delta E_b/kT} \quad (5.18)$$

where  $\Delta E_B$ 's (and  $\Delta E_b$ ) are the energy barriers to be crossed, and the coefficient  $C_{bB}$  is the normalization constant which is determined from

$$P_{B1} + P_{B2} + \dots + P_{B11} + P_b = 1 \quad (5.19)$$

giving

$$C_{bB} = \frac{1}{e^{-\Delta E_{B1}/kT} + e^{-\Delta E_{B2}/kT} + \dots + e^{-\Delta E_{B11}/kT}} + e^{-\Delta E_b/kT} \quad (5.20)$$

and the time steps associated with each jump are

$$\begin{aligned} t_{B1} &= \tau_{bB} e^{\Delta E_{B1}/kT} \\ t_{B2} &= \tau_{bB} e^{\Delta E_{B2}/kT} \\ &\vdots \\ t_{B11} &= \tau_{bB} e^{\Delta E_{B11}/kT} \\ t_b &= \tau_{bB} e^{\Delta E_b/kT} \end{aligned} \quad (5.21)$$

respectively, where  $\tau$ 's are constants.

Hence the average escape times, starting from valley  $a$  and exiting from exit  $A_i$ , are

$$\langle t_{a \rightarrow A_i} \rangle = \frac{\sum_{n=0}^{\infty} P_{A_i} P_a^n P_b^n (nt_a + nt_b + t_{A_i})}{\sum_{n=0}^{\infty} P_{A_i} P_a^n P_b^n}, \quad (5.22)$$

starting from valley  $a$  and exiting from exit  $B_i$ ,

$$\langle t_{a \rightarrow B_i} \rangle = \frac{\sum_{n=0}^{\infty} P_{B_i} P_a^{(n+1)} P_b^n ((n+1)t_a + nt_b + t_{B_i})}{\sum_{n=0}^{\infty} P_{B_i} P_a^{(n+1)} P_b^n}, \quad (5.23)$$

starting from valley  $b$  and exiting from exit  $A_i$ ,

$$\langle t_{b \rightarrow A_i} \rangle = \frac{\sum_{n=0}^{\infty} P_{A_i} P_b^{(n+1)} P_a^n ((n+1)t_b + nt_a + t_{A_i})}{\sum_{n=0}^{\infty} P_{A_i} P_b^{(n+1)} P_a^n}, \quad (5.24)$$

and finally, starting from valley  $b$  and exiting from exit  $B_i$ ,

$$\langle t_{b \rightarrow B_i} \rangle = \frac{\sum_{n=0}^{\infty} P_{B_i} P_b^n P_a^n (nt_b + nt_a + t_{B_i})}{\sum_{n=0}^{\infty} P_{B_i} P_b^n, P_a^n} \quad (5.25)$$

where  $i = 1, 2, 3 \dots 11$ , the exit indexes.

During the simulation, at each step, we can check which atom exchanges places with the vacancy. If the same atom is exchanging places over and over, then this means that we have fallen into a sandtrap. Sometimes, the vacancy is trapped there until the end of the simulation, and sometimes after jumping back and forth several times, it gets out of the trap. When we detect a sandtrap, we take the vacancy out of that trap, increase the total simulation time by the average escape time and then resume the simulation at the next simulation step.

However, care must be taken because a sandtrap can consist of more than two valleys. In this case, the average escape times need to be calculated for multi valleys with the same approach described above. During our simulations, we didn't sample sandtraps with more than two valleys. However, to overcome sandtraps in the recent calculations, instead of running one sample and using the average escape times, we prepared ten identical samples with the vacancy located at randomly selected position. After running the simulation for these ten samples under the same conditions, we averaged the diffusivity coefficients over these ten runs. Even if some samples fall into the sandtraps, the averaged diffusivity coefficient is not effected significantly.

Reader should note that the lower the temperature, the more sandtraps will be observed. Thus averaging over identical samples won't produce good results since the majority of the samples will be falling into sandtraps. In this case, the average escape time calculations are inevitable.



# Chapter 6

## Conclusions and Discussion

### 6.1 Diffusion in Binary Alloys

The results of this work demonstrate that the on-the-fly kinetic Monte Carlo method is sufficiently robust to provide reasonable results for the tracer diffusivities in binary intermetallic alloys showing significant deviations from ideal solid solution. This work becomes more valuable to calculate the tracer diffusion coefficients for the cases where there are no available isotopes to carry out the tracer diffusion experiments. However, the limitation of this local method is clearly present near critical transitions, where large fluctuations in the local environment become statistically overwhelming. During the simulations at low temperatures, we sometimes came across configurations in ordered phase in which the vacancy can spend a large number of steps moving locally without accomplishing significant displacements or accumulating much simulated time (see chapter 5: *Sandtrap Limitation and How to Overcome it*). For these reasons, a more strategic method would be required to treat the entire range of temperatures and compositions, but this method does provide useful results.

## 6.2 Translation of an APB

In the presented work of Anti-Phase Boundary in a strongly ordered alloy,  $Ni_3Al$ , we observed that in the absence of a driving force, the vacancy doesn't have any preferred direction, thus creating anti-site defects on both side of the APB equally as it wanders around. The nature of its "randomness" and its effect on the translation of the APB requires further investigation. However, we have seen that the binding of the vacancy to the APB doesn't cause the *zipper* effect, as one would expect. When the vacancy wanders by the APB, it translates a portion of the APB and then wanders off. When it comes back again, it translates another portion. In this way, the AMD simulations are more revealing than simple static calculations of the binding energy. We have also seen a dependence of the distribution of the concentration of anti-site defects on temperature, as expected. The statistical fluctuations were overwhelming thus preventing us making further analysis, but we have clearly observed the translation of the APB in a certain direction when under bias. Much longer simulation time is required if one wants to investigate the nature of the motion, but for now, we can conclude that the vacancy-assistance is very plausible and on-the-fly kinetic Monte Carlo works reasonably well.

# Chapter 7

## Future Work

- Developing a more efficient way to avoid sandtraps (see Chapter 5: *Sandtrap Limitation and How to Overcome it*) to improve the statistics.
- Calculating tracer diffusivities at the high and the low end concentrations.
- Calculation of tracer diffusivities for di-vacancies as a function of temperature and concentration.
- Analyzing the effects of vacancy concentration on tracer diffusivities.
- Including pressure effects on tracer diffusivity.
- Improving the statistics on Anti-Phase Boundary calculations by running more samples.
- Redefining the “width” to improve analysis of the translation of the Anti-Phase Boundary.

# References

- [All82] A.R. Allnatt. *J. Phys. C*, 15:5605, 1982.
- [Ant75] T.R. Anthony. *Diffusion in Solids, Recent Developments*, edited by A.S. Nowick and J.J. Burton, p353. New York: Academic Press, 1975.
- [Bol94] L. Boltzmann. *Ann. Phys.*, 53:960, 1894.
- [Car90] A.E. Carlsson. *Solid State Physics*, edited by H. Ehenreich, D. Thrnbull, pp.1-91. Boston: Harcourt Brace Jovanovich, 1990.
- [Cha78] D. Chandler. *J. Chem. Phys.*, 68:2959, 1978.
- [Dar48] L.S. Darken. *Trans. Amer. Inst. Min. (Metall.) Engrs.*, 175:184, 1948.
- [Daw89] M.S. Daw. *Phys. Rev. B.*, 39:7441–7452, 1989.
- [DB83] M.S. Daw and M.I. Baskes. *Phys. Rev. Lett.*, 50:1285, 1983.
- [DB84] M.S. Daw and M.I. Baskes. *Phys. Rev. B.*, 29:6443–6453, 1984.
- [DFB93] M.S. Daw, S.M Foiles, and M.I. Baskes. *Mater. Sci. Rep.*, 9:251, 1993.
- [FBD86] S.M. Foiles, M.I. Baskes, and M.S. Daw. *Phys. Rev. B.*, 33:7983, 1986.
- [Fic55] A. Fick. *Philos. Mag.*, 10:30, 1855.
- [Fre75] W.J Fredericks. *Diffusion in Solids, Recent Developments*, edited by A.S. Nowick and J.J. Burton, p381. New York: Academic Press, 1975.
- [FW91] K.A. Fichthorn and W.H. Weinberg. *J. Chem. Phys.*, 95:1090, 1991.
- [GYKL94] E.P. George, M. Yamaguchi, K.S. Kumar, and C.T. Liu. *Annu. Rev. Mater. Sci.*, 24:409–451, 1994.
- [Har06] C.C. Harris. *Vacancy-Mediated Diffusion in Ni<sub>3</sub>Al Using Kinetic Monte Carlo*. Clemson University Masters Thesis, 2006.
- [HJ99] G. Henkelman and H. Jónsson. *J. Chem. Phys.*, 111:7010, 1999.

- [HJ00] G. Henkelman and H. Jónsson. *J. Chem. Phys.*, 113:9978, 2000.
- [HJ01] G. Henkelman and H. Jónsson. *J. Chem. Phys.*, 115:9657, 2001.
- [HL64] R.E. Howard and A.B. Lidiard. *Rep. Prog. Phys.*, 27:161, 1964.
- [HTDM06] C.C. Harris, R. Tedstrom, M.S. Daw, and M.J. Mills. *Comput. Mater. Sci.*, 37:462, 2006.
- [Jam76] A.M. James. *A Dictionary of Thermodynamics*. ISBN:0470150351, 1976.
- [Mat33] C. Matano. *Jpn. Phys.*, 8:109, 1933.
- [MCB79] J.A. Montgomery, D. Chandler, and B.J. Berne. *J. Chem. Phys.*, 70:4056, 1979.
- [MRR<sup>+</sup>53] N. Metropolis, A.W. Rosenbluth, M.N. Rosenbluth, A.H. Teller, and E. Teller. *Chem. Phys.*, 21:1087, 1953.
- [RJS94] T.S. Rong, I.P. Jones, and R.E. Smallman. *Scripta Metall. Mater.*, 30:19, 1994.
- [SE47] A.D. Smigelskas and E.O. Kirkendall. *Trans. AIME*, 171:130, 1947.
- [VMG02] A.F. Voter, F. Montalenti, and T.C. Germann. *Ann. Rev. Mater. Res.*, 32:321, 2002.